Archives of Computational Methods in Engineering
https://doi.org/10.1007/s11831-025-10245-4

REVIEW

Recent Progress of Digital Reconstruction in Polycrystalline Materials

Bingbing Chen[1] · Dongfeng Li[2] · Peter Davies[3] · Richard Johnston[3] · Xiangyun Ge[1] · Chenfeng Li[1]

Received: 19 November 2024 / Accepted: 9 February 2025

Abstract

This study comprehensively reviews recent advances in the digital reconstruction of polycrystalline materials. Digital reconstruction serves as both a representative volume element for multiscale modelling and a source of quantitative data for microstructure characterisation. Three main types of digital reconstruction in polycrystalline materials exist: (i) experimental reconstruction, which links processing-structure-properties-performance by reconstructing actual polycrystalline microstructures using destructive or non-destructive methods; (ii) physics-based models, which replicate evolutionary processes to establish processing-structure linkages, including cellular automata, Monte Carlo, vertex/front tracking, level set, machine learning, and phase field methods; and (iii) geometry-based models, which create ensembles of statistically equivalent polycrystalline microstructures for structure-properties-performance linkages, using simplistic morphology, Voronoi tessellation, ellipsoid packing, texture synthesis, high-order, reduced-order, and machine learning methods. This work reviews the key features, procedures, advantages, and limitations of these methods, with a particular focus on their application in constructing processing-structure-properties-performance linkages. Finally, it summarises the conclusions, challenges, and future directions for digital reconstruction in polycrystalline materials within the framework of computational materials engineering.

Nomenclature

μCT	micro-Computed Tomography
2D	Two-Dimensional
3D	Three-Dimensional
AM	Additively Manufacturing
ART	Algebraic Reconstruction Technique
ASR	Algebraic Strain Refinement
AVM	Alkemper and Voorhees Micromiller
BIB	Broad Ion Beam
CA	Cellular Automata
CDBN	Convolutional Deep Belief Network
CFD	Computational Fluid Dynamics
CPFEM	Crystal Plasticity Finite Element Method
DAXM	Differential-Aperture X-ray Microscopy
DBFIB	Dual Beam Focused Ion Beam
DCT	Diffraction Contrast Tomography
DED	Direct Energy Deposition
DFXM	Dark Field X-ray Microscopy
DIC	Digital Image Correlation
DL	Deep Learning
DLD	Direct Laser Deposition
DNN	Dendritic Needle Network
DR	Digital Reconstruction
DRX	Dynamic recrystallisation
EBSD	Electron Backscattering Diffraction
EBSM	Electron Beam Selective Melting
EP	Ellipsoid packing
FCA	Frontal Cellular Automata
FDM	Finite Difference Method
FEM	Finite Element Method
FF-HEDM	Far-Field High Energy Diffraction Microscopy
FIB	Focused Ion Beam
FSAM	Friction Stir Additive Manufacturing
FSW	Friction Stir Welding
FVM	Finite Volume Method
GFIB	Gallium Focused Ion Beam
GP	Gaussian Process
HD-DRC	High Resolution Digital Image Correlation
HDMR	Hybrid Deposition and Micro-Rolling

✉ Chenfeng Li
c.f.li@swansea.ac.uk

[1] Zienkiewicz Institute for Modelling, Data and AI, Faculty of Science and Engineering, Swansea University, Swansea SA1 8EN, United Kingdom

[2] School of Science, Harbin Institute of Technology, Shenzhen 518055, China

[3] Advanced Imaging of Materials (AIM) Facility, Faculty of Science and Engineering, Swansea University, Swansea SA1 8EN, United Kingdom

Published online: 01 March 2025

ICME	Integrated Computational Materials Engineering
LabDCT	Laboratory X-ray Diffraction Contrast Tomography
LAD	Laser Additive Manufacturing
LBM	Lattice Boltzmann Method
LP	Laguerre Polyhedron
LPBF	Laser Powder Bed Fusion
LS	Level Set
LV	Laguerre Voronoi
MC	Monte Carlo
MCA	Multilevel Cellular Automaton
MCS	Manual Collection System
ML	Machine Learning
MPS	Multiple-Point Simulation
MRF	Markov Rrandom Field
Nano-CT	Nano Computed Tomography
NF-HEDM	Near-Field High Energy Diffraction Microscopy
NXRD-CT	Nano X-ray Diffraction Computed Tomography
OIM	Orientation Imaging Microscopy
OM	Optical Microscopy
OMiTEM	Orientation Mapping in the Transmission Electron Microscope
PB-LBM	Powder Bed Laser Beam Melting
PBF	Powder Bed Fusion
PC-CA	Parallel Computing-Cellular Automata
PCR	Polycrystal Refinement
PF	Phase Field
PFIB	Plasma Focused Ion Beam
PS	Processing-Structure
PSPP	Processing-Sructure-Properties-Performance
PV	Poisson Voronoi
RGR	Recursive Grain Remapping
RM	Robo-Met.3D
ROI	Region of Interest
RVE	Representative Volume Element
S-μCT	Synchrotron Micro-computed Tomography
S3DXRD	Scanning Three-Dimensional X-ray Diffraction Microscopy
SBFIB	Single Beam Focused Ion Beam
SEM	Scanning Electron Microscopy
SERVEs	Statistically Equivalent Representative Volume Elements
SLM	Selective Laser Melting
SM	Spectral Method
SM	Synthetic Microstructure
SPED	Scanning Precession Electron Diffraction
SPFM	Sharp Phase Field Method
SPP	Structure-Properties-Performance
SRX	Static recrystallisation
TB	Tribeam
TS	Texture synthesis
TT	Topotomography
VAE	Variational Autoencoder
VOF	Volume-of-fluid
VP	Voronoi Polyhedron
VSCA	Virtual Submesh Cellular Automata
VT	Voronoi tessellation

1 Introduction

Polycrystalline materials such as metals [1–3], rocks [4] and ceramics [5] are commonly encountered in nature and industry. Their formation involves nucleation and growth through solidification, recrystallisation, grain growth, and solid-state phase transformation. These evolutionary processes form the polycrystalline microstructure with random morphological and crystallographic characteristics, consisting of grain aggregates with varying lattice orientations and sizes separated by grain boundaries. The random characteristics of polycrystalline microstructures affects fundamentally the macroscopic properties and performance of polycrystalline materials [1–5].

Advancements in microscopic imaging, particularly Orientation Imaging Microscopy techniques (OIM) such as X-ray diffraction and electron backscattering diffraction, have made quantitative microstructure characterisation/representation of polycrystalline materials essential for understanding how processing history shapes microstructure and influences material properties. The characteristics of polycrystalline microstructure is typically represented by a range of statistical descriptors, including phase volume fraction, two-point correlation, chord length [6–8], grain orientation [9], grain misorientation [9], axial grain size [10], and N-point probability functions [11–13], among others.

Microstructure reconstruction generates digital polycrystalline microstructures that can be used to support further quantitative analysis. Such digital microstructures are often referred to as Representative Volume Elements (RVEs) in the literature, defined as the minimum volume of a microstructure whose properties and statistical descriptors exactly match those of a macroscopic solid [14]. RVE generation techniques for polycrystalline materials are divided into experimental and synthetic models [15]. Experimental models focus on reconstruction through experimental characterisation of actual polycrystalline microstructures. However, relying solely on imaging techniques to study the polycrystaline microstructures has limitations. First, obtaining high-quality microstructure images can be time-consuming and costly. Second, capturing all the random characteristics formed during processing is challenging, either due to the lack of statistical homogeneity in experimental

reconstructions or because the parameter space is too vast to sample effectively within a reasonable time frame [16].

Synthetic models offer an efficient alternative to experimental reconstruction. These models can be generally classified into two types: physics-based and geometry-based [15, 16]. Physics-based models replicate the microstructure formation processes, leveraging the fundamental principles of Processing-Structure (PS) linkages in polycrystalline materials. Various methods are employed in physics-based reconstructions, including cellular automata, Monte Carlo methods, vertex/front tracking, level set methods, and phase field methods. On the other hand, geometry-based models create ensembles of statistically equivalent polycrystalline microstructures, commonly referred to as Statistically Equivalent Representative Volume Elements (SERVEs) [14, 17–19]. The effective properties and statistical characterisations derived from averaging multiple geometric reconstructions are equivalent to those obtained from an RVE reconstruction [14, 20]. Techniques such as simplistic morphology, Voronoi tessellation, ellipsoid packing, texture synthesis, high-order methods, reduced-order methods, and machine learning are all used in the geometry-based reconstructions of polycrystalline microstructures.

After digitally reconstructing polycrystalline materials, the digital microstructure must be discretised to support computational modelling. Accurate identification of the grain morphology plays a crucial role in this process. Generally, microstructure discretisation can be achieved through two approaches: (a) grid discretisation and (b) vertex-edge-face discretisation. The grid discretisation method employs regular grid units to partition the entire domain systematically. This approach is independent of grain shapes, making it straightforward to implement and widely utilized in data collection for experimental reconstruction, as well as in cellular automata and Monte Carlo methods within physics-based reconstructions. However, the grain morphology characterised through grain discretisation is often limited to basic geometric forms and can be significantly affected by grid anisotropy. In contrast, the vertex-edge-face discretisation method begins by discretizing vertices to establish coordinate points, which are then used to generate grain edges. These edges serve as the foundation for constructing grain faces, ultimately forming grain volumes within the space. This approach is highly dependent on the specific shapes of the grains, allowing for flexible and accurate characterisation of diverse grain morphologies. Consequently, it is extensively employed to capture complex interfaces in polycrystalline materials.

The remainder of the paper is structured into four sections. section 2 discusses the methods for experimental reconstruction of actual polycrystalline microstructures. section 3 focuses on physics-based techniques for reconstruction of microstructure evolution under specific processing constraints. section 4 explores geometry-based reconstruction methods aimed at generating statistical characterisations in polycrystalline materials. Finally, concluding remarks, challenges, and future perspectives are presented in section 5.

2 Experimental Reconstruction

There are many imaging techniques capable of obtaining microstructure information for polycrystalline materials. Generally speaking, these techniques can be classfied into three categories [21]:

- Plane-section microscopy techniques: Optical Microscopy (OM) [22], and Scanning Electron Microscopy (SEM) [23].
- X-ray microtomography techniques: micro-Computed Tomography (μCT) [24], Synchrotron micro-Computed Tomography (S-μCT) [24], and Nano Computed Tomography (NanoCT) [24].
- Orientation Imaging Microscopy (OIM) techniques: X-ray diffraction [25], three dimensional Orientation Mapping in the Transmission Electron Microscope (3DOMiTEM) [26], Scanning Precession Electron Diffraction (SPED) [27], and Electron Backscattering Diffraction (EBSD) [28].

Among the aforementioned techniques, plane-section microscopy and X-ray imaging are used to detect variations in microstructural scale, composition and chemistry within polycrystalline materials. Orientation imaging microscopy techniques, on the other hand, measure lattice orientation through Bragg diffraction. These microscopic imaging techniques can be broadly divided into two categories: destructive and non-destructive approaches [15]. Destructive reconstruction involves acquiring data by sequentially removing sections of the material (Fig 2), while non-destructive reconstruction gathers data through a series of transmission images taken from different projection angles (Fig 9). Although destructive reconstruction techniques are more commonly used in experimental reconstruction due to their accessibility and higher resolving capability, they consume the material specimen and can be time-consuming. Additionally, the quality of reconstruction is heavily influenced by the sample preparation. In contrast, non-destructive reconstruction preserves the integrity of the sample but requires the use of high-intensity radiation sources. Figure 1 illustrates the classification of imaging techniques, whilst the following two subsections provide detailed information on destructive and non-destructive reconstruction methods, including their workflows, advantages, and disadvantages.

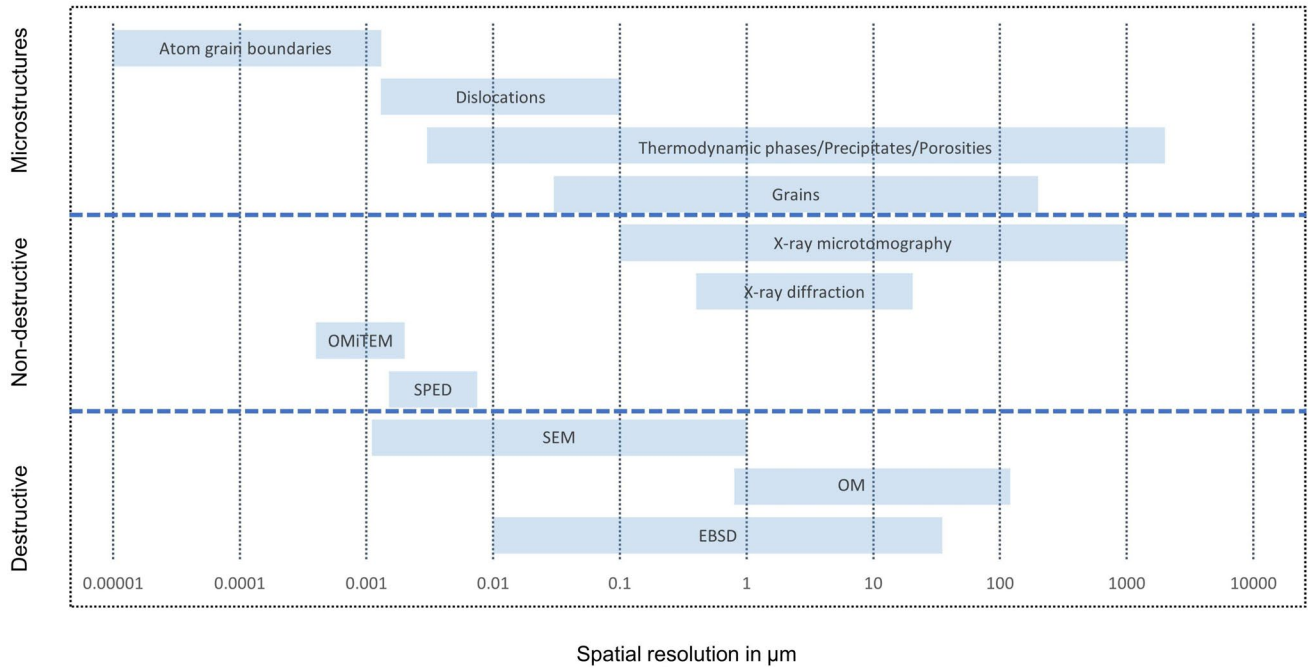

Fig. 1 Imaging techniques for polycrystalline materials: destructive and non-destructive reconstruction, and the spatial resolution

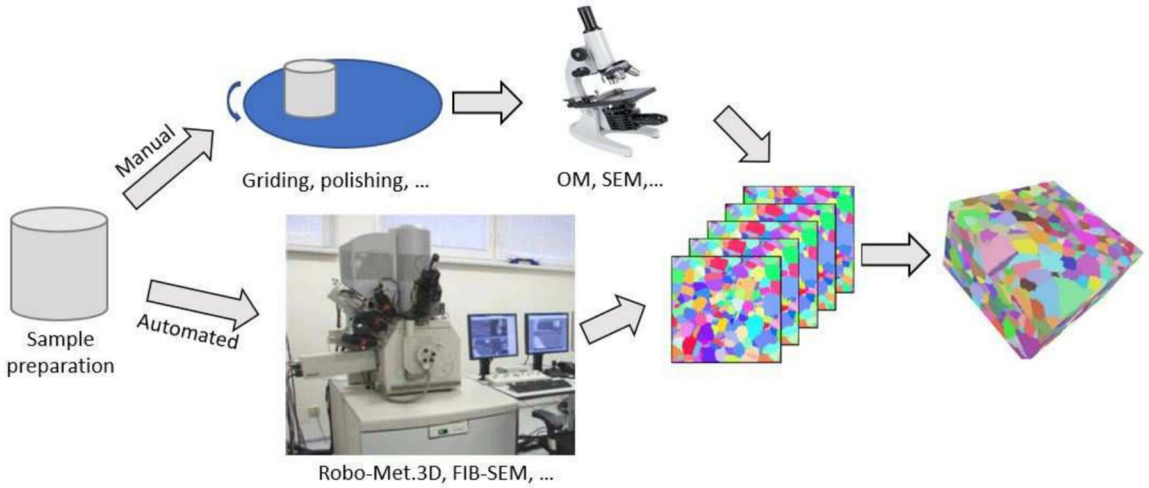

Fig. 2 The workflow of destructive reconstruction. Adapted from [40], Copyright (2008), with permission from Elsevier

2.1 Destructive Reconstruction

Early efforts to reconstruct 2D polycrystalline microstructures using destructive reconstruction methods were successful. However, crucial morphological information such as grain size, shape and boundary features is influenced by spatial connectivity in 3D space and cannot be fully quantified from 2D microstructures alone. In recent years, the serial sectioning methodology has been developed to address this limitation by collecting and assembling 2D microstructure data into a 3D reconstruction of polycrystalline materials. The serial sectioning reconstruction process involves three steps: data collection, data processing, and space discretisation.

- Data collection: In this step, 2D microstructure data is sequentially collected for later assembly into a 3D model, as illustrated in Fig 2. Data collection can be performed manually or automatically, with manual methods tracing back to the 1960s. The process begins by preparing

repetitive, consistent-thickness, and flat sections through techniques such as sputtering, ablating, polishing, etching, and cutting. This continues until the the desired sample volume is achieved. OM [22] and SEM [23] are commonly used to visualize grain boundaries [22, 23], microcracks [29], pores [30] and precipitates [23], while Electron Backscatter Diffraction (EBSD) [31] is employed to characterise crystallographic information. The repetitive nature of this data collection process lends itself well to automation, which enhances efficiency and reduces variability [32]. Several automated devices are commonly used for serial sectioning reconstruction [33], including the Alkemper and Voorhees Micromiller (AVM) [34], Robo-Met.3D (RM) [30], Broad Ion Beam (BIB) [35] and Focused Ion Beam (FIB) systems, such as Gallium FIB (GFIB) [36, 37]), multiple beam FIB systems and Plasma FIB (PFIB) [38]. In practice, these automation devices are often integrated with imaging systems. For instance, the OM is paired with AVM [34] and RM [39], while SEM is used with RM [30], BIB [35] and FIB [36]. AVM, RM and BIB can achieve micron-level precision, making them suitable for imaging micron-scale features such as grains, thermodynamic phases, and pores (Fig 1). FIB systems can achieve high accuracy on both micron and submicron scales, suitable for imaging grains, grain boundaries, and precipitates (Fig 1). Additionally, FIB systems can produce highly refined serial sections with thickness approximately 10-15nm through closed-loop control. Beyond OM and SEM, EBSD can be integrated into RM [30], BIB [35], and FIB [40] systems to provide comprehensive microstructure reconstructions, incorporating detailed crystallographic information.

- Data processing: This step combines the collected 2D data sets into a 3D data stack through a series of operations, including thresholding, alignment, clean-up and segmentation [31]. Depending on the imaging techniques used during data collection, three primary microstructure segmentation strategies are employed: the watershed algorithm for identifying grain boundaries in OM (Fig 3a), brightness contrast for identifying precipitates in SEM (Fig 3b), and orientation data mapping for identifying grains and twins in EBSD (Fig 3c). For more detailed information on these segmentation strategies, readers are directed to the references [41].
- Space discretisation: This step identifies individual grains within the digital microstructure using either grid or vertex-edge-face-volume discretisation. The grid discretisation method is primarily employed during data collection and processing, and it sometimes serves as an input for the vertex-edge-face discretisation scheme. Two main techniques used in the vertex-edge-face-volume method are the marching cubes algorithm [22] and the CAD-based surface fitting technique [40]. The marching cubes algorithm captures grain topological information, such as quadruple points, triple lines, and grain surfaces (Fig 4). This process begins by replacing boundary grids with marching cubes, followed by identifying the intersection of the isosurface, and concluding with smoothing and mesh decimation. On the other hand, the CAD-based surface fitting technique offers a smooth characterisation of grain surfaces. It starts by identifying the set of boundary grids, then matching polynomial surfaces, and concludes with an algorithm to clean up overlaps and gaps.

Recent research on the serial sectioning methodologies has focused on large-scale datasets, high efficiency, and high-resolution reconstruction to better characterise complex, fine microstructures. Although the FIB system offers improved sectioning fidelity and efficient automated serial sectioning and image acquisition [42], it has limitations regarding the volumes, portions, resolution, and milling times of the collected data [38]. To address these shortcomings, researchers have developed OM-based 3D reconstruction techniques to view and analyze large grain datasets [43]. Additionally, the Xenon plasma-focused ion beam (PFIB) has been introduced, offering faster milling times, improved resolution, and the ability to handle larger volumes compared to conventional FIB systems [38]. The PFIB has been successfully employed to reconstruct the α lath and 3-variant clusters in additively manufactured Ti-6Al-4V [31] (Fig 5).

Furthermore, the Tribeam (TB) system has been developed by integrating a femtosecond laser into a FIB setup [44]. The main advantage of the TB (laser-FIB) system is its significantly faster milling time, up to 2,000 times quicker than traditional FIB and 100 times faster than PFIB without causing substantial damage to the material [45]. More recently, a TB system has been implemented on the PFIB platform (femtosecond laser-PFIB) [29], enabling laser sectioning at rates 4–5 orders of magnitude faster than GFIB [33] and subsequent surface cleanup at speeds 10–20 times faster than GFIB. Moreover, advanced imaging processing techniques have been introduced to enhance data processing and ensure accurate microstructure reconstruction. Examples include machine learning approaches for precipitate segmentation and classification [23], the k-means clustering algorithm for determining initial growth orientations in grains with complex morphologies [44], the variant graph approach [46] (Fig 6), and the graph clustering algorithm for parent grain reconstruction [47].

Destructive reconstruction has become a widely used technique for building PSPP linkages in polycrystalline materials [29]. It has been applied in various processes, including solidification, recrystallisation, grain growth, and solid-state phase transformation, in both traditional and additive manufacturing (Table 1). For example, [48] built the TB

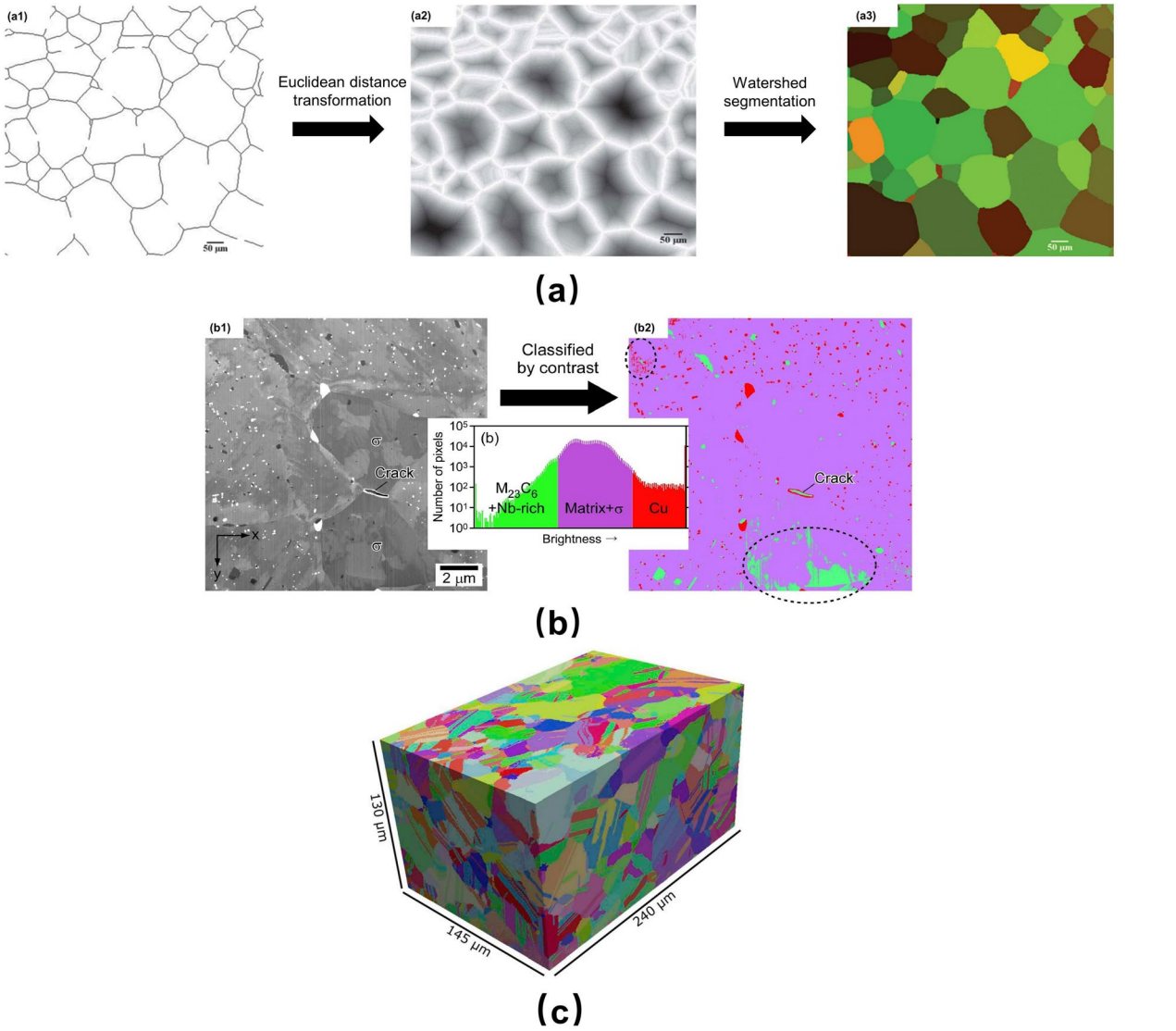

Fig. 3 Microstructure segmentation strategies in destructive reconstruction: **a** the watershed algorithm for identifying grain boundaries in OM, adapted from [22], Copyright (2014), with permission from Elsevier; **b** brightness contrast for identifying precipitates in SEM, reprinted from [23], Copyright (2021), with permission from Elsevier; **c** orientation data mapping for identifying grains and twins in EBSD, reprinted from [41], Copyright (2020), with permission from Elsevier

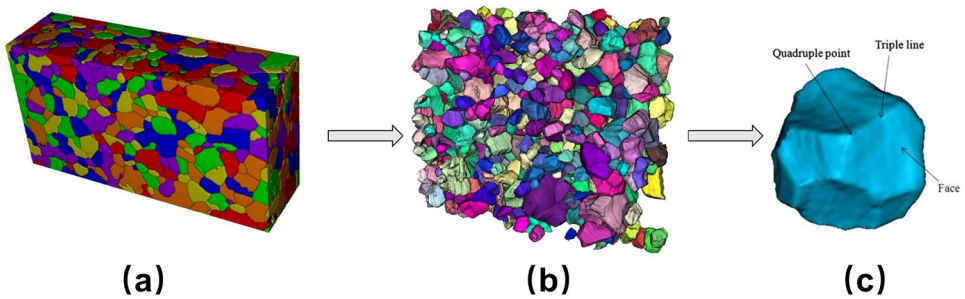

Fig. 4 Large-dataset reconstruction of polycrystalline microstructures: **a** visualization of a part of the large-dataset reconstruction, **b** visualization of the internal structure, **c** visualization of a single grain exhibiting different topological characteristics. Adapted from [22], Copyright (2014), with permission from Elsevier

system of EBM-printed bulk IN718 to reveal the sensitivity of microstructure solidification under steady-state growth conditions (Fig 7). The SEM was utilized [49] to study the surface and subsurface recrystallisation reconstruction of

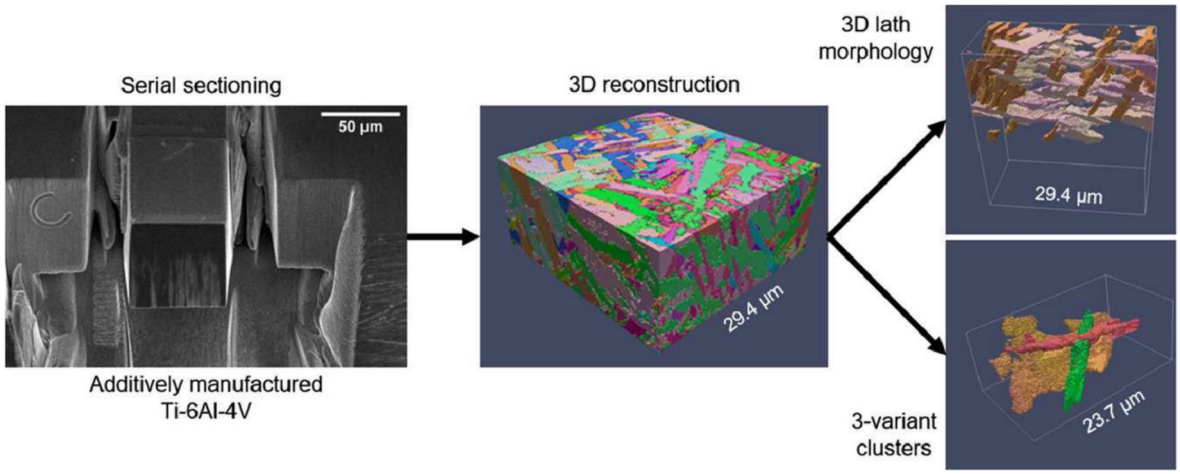

Fig. 5 The α lath and 3-variant clusters in additively manufactured Ti-6Al-4V reconstructed by PFIB-SEM. Reprinted from [31], Copyright (2020), with permission from Elsevier

polycrystalline platinum during the annealing stage in the oxygen atmosphere. The EBSD was employed by [50] to reconstruct the transformation from the as-solidified β-Ti phase to α-Ti phase in melted Ti-6Al-4V. In addition to PS linkages, Digital Image Correlation (DIC) techniques have been used to establish SPP connections [51]. DIC tracks surface characteristics of a sample through a series of digital reconstructions to generate a displacement field, which can then be used to measure the strain fields on the specimen's surface [52]. This technique has been combined with spatial and crystallographic orientation data from EBSD to detect microstructural strain localization [53] and has also been adapted for high-resolution DIC (HR-DIC) within SEM [54]. Moreover, femtosecond laser-PFIB techniques have been employed on AA7050 and AA7085 alloys to investigate the interaction of 3D cracks with the surrounding microstructure [29] (Fig 8). Several open-source software packages are availalbe for destructive reconstruction in polycrystalline materials, including ImageJ [55], MTEX [56], and DREAM.3D [57].

2.2 Non-Destructive Reconstruction

Non-destructive reconstruction generates a 3D reconstruction of polycrystalline materials by combining 2D projection images, thereby avoiding the need for material section removal (Fig 9). The main workflow of non-destructive reconstruction is similar to those of the serial sectioning method, but the algorithms employed differ significantly.

- Data collection: In this step, 2D projection data is sequentially acquired using X-ray microtomography and X-ray diffraction techniques. X-ray microtomography is generally classified into absorption and phase contrast types [24]. In absorption-contrast X-ray microtomography systems like μCT, S-μCT, and Nano-CT, mathematical projection algorithms can interpret measured intensity variations as an attenuation coefficient distribution, which reveals porosity, crack morphology, grain boundaries, precipitates, thermodynamic phases, and other microstructural features within polycrystalline materials (Table 2). Phase-contrast X-ray microtomography systems exhibit significantly greater sensitivity to small density differences and varying phase shift than absorption-contrast X-ray microtomography due to coherent Fresnel diffraction techniques [64, 65] and are additionally employed for detecting brittle fractures and fatigue cracks (Table 2). X-ray diffraction systems including Differential-Aperture X-ray Microscopy (DAXM) [66], Three-Dimensional X-ray Diffraction Microscopy [67] (3DXRD, also known as High-Energy X-ray Diffraction Microscopy (HEDM) [68]), and Diffraction Contrast Tomography (DCT) [69], utilize Bragg diffraction to measure crystallographic orientation [64]. DAXM combines the polychromatic synchrotron X-ray microbeam and a charge-coupled device detector to measure intra- and intergranular orientations and grain sizes [70]. The HEDM was established at Denmark's Risϕ National Laboratory to reconstruct 3D grain orientations and boundary maps [67]. HEDM can be further categorized as Near-Field High Energy Diffraction Microscopy (NF-HEDM) and Far-Field High Energy Diffraction Microscopy (FF-HEDM) [64, 71]. NF-HEDM uses high-resolution near-field detectors to reveal grain orientations, shapes, and edges, whereas FF-HEDM employs far-field detectors with lower resolution to determine each grain's centroid position, average orientation and average lattice strain tensor [72]. Recent advancements have inte-

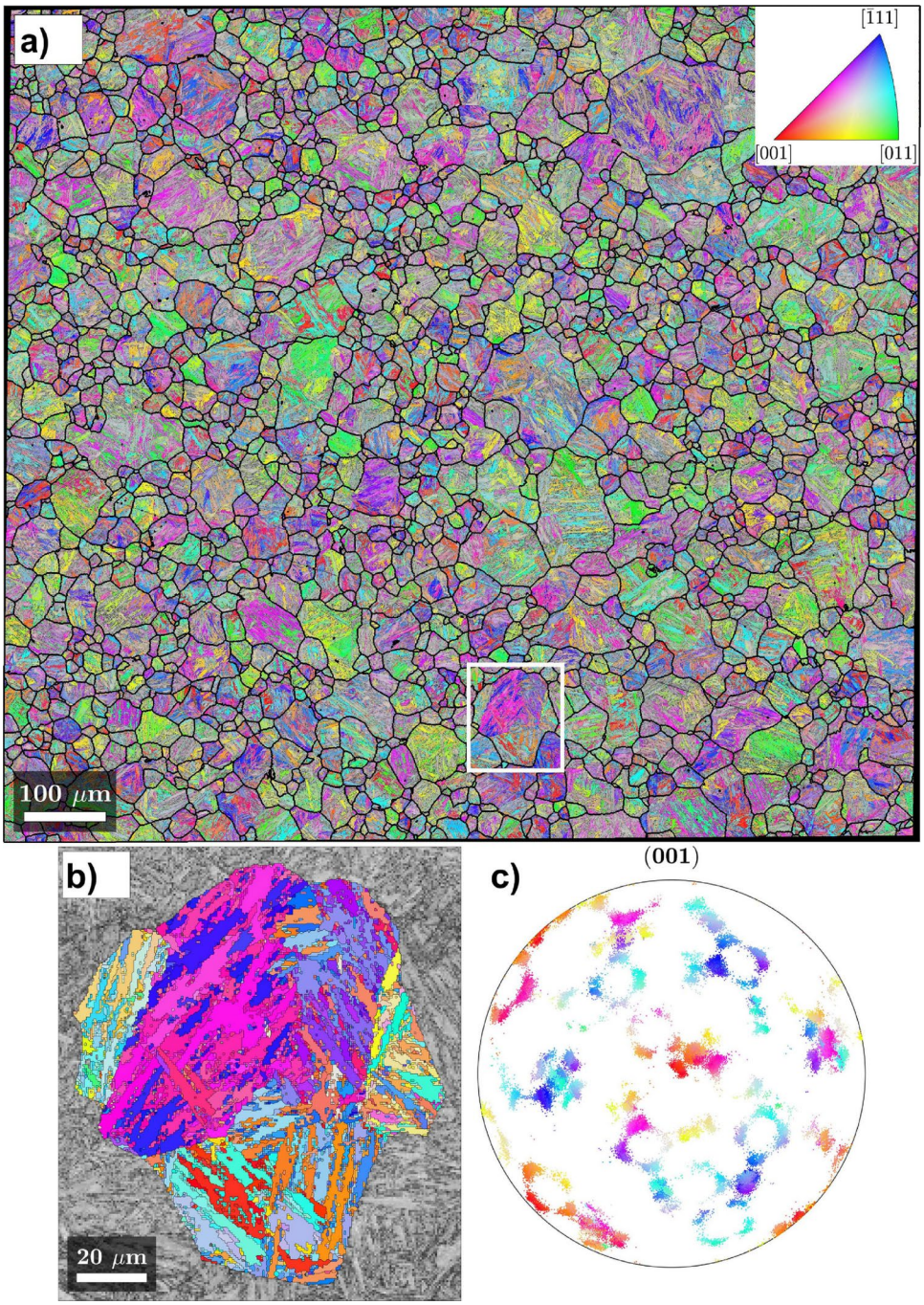

Fig. 6 Parent grain reconstruction using the variant graph approach: **a** the reconstructed parent austenite grains are shown in black boundaries, **b** a single, heavily twinned parent austenite grain extracted from **a**, **c** pole figure showing the martensite orientations in **b**. Reprinted from [46], Copyright (2022), with permission from Elsevier

grated NF-HEDM and FF-HEDM techniques to reconstruct spatial intragranular lattice orientation fields [71]. Furthermore, NF-HEDM and X-ray microtomography techniques have been employed together to establish the SPP connections in polycrystalline materials (Fig 10). The DCT, developed by [73] and inheriting projection reconstruction principles from 3DXRD, utilizes a monochromatic wide beam and a single near-field detector to reconstruct grain and orientation maps with full 360° scans. This technique reduces scanning and analysis times while facilitating integration with X-ray microtomography [69, 72]).

- Data processing: This step integrates 2D projection data from X-ray microtomography and X-ray diffraction into a 3D data set through advanced image processing algorithms. For example, the filtered back projection algorithm [78] and image segmentation techniques [90] for X-ray microtomography data (Fig 11a). Readers are directed to [77] for more detailed information. In X-ray diffraction data processing, examples include the thresh-

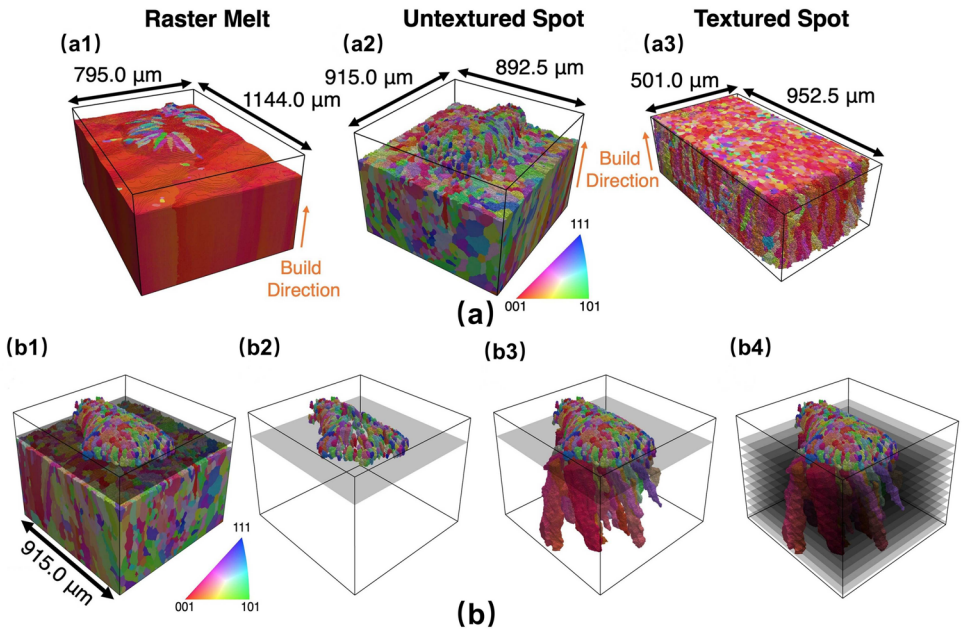

Fig. 7 Solidification reconstruction of bulk IN718 under steady-state growth conditions: **a** fully-reconstructed 3D volumes of **a1** the Raster Melt sample, **a2** the Untextured Spot sample, and **a3** the Textured Spot sample; **b** isolated solidification event in Untextured Spot sample **b1** the Untextured Spot build, **b2** nucleated grains lying fully above the planar cutoff, **b3** the full-extent of grains touching the isolated melt pool, **b4** gray planes spaced 50 μm along the build direction. Reprinted from [48], Copyright (2022), with permission from Elsevier

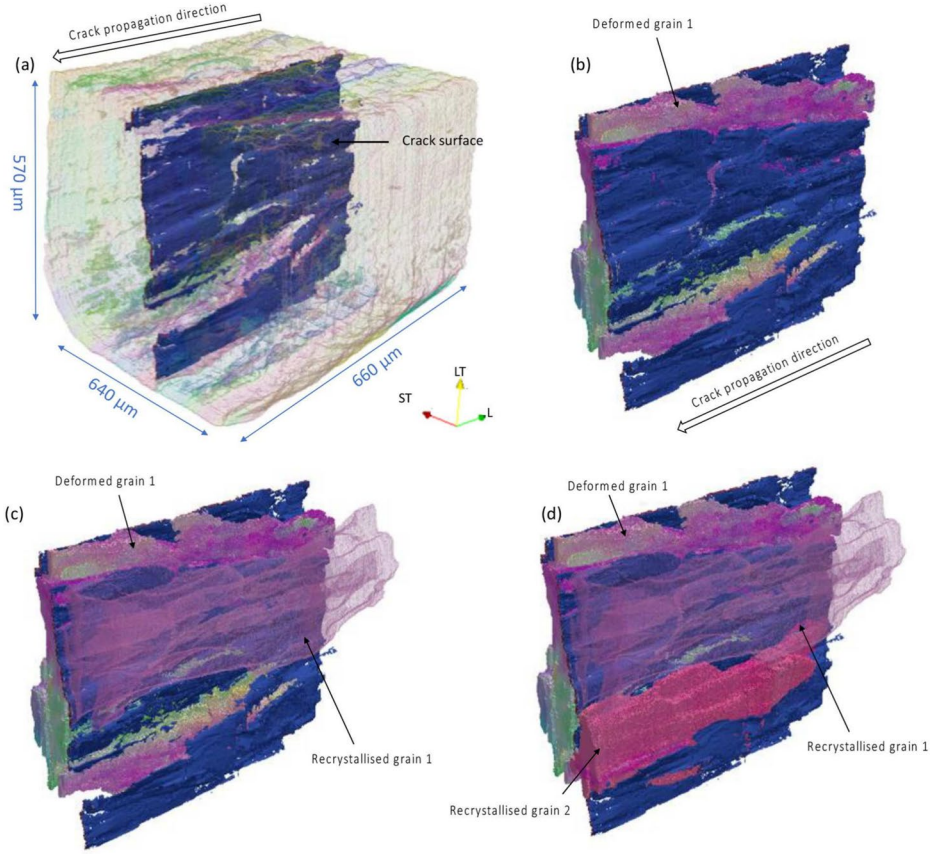

Fig. 8 3D reconstruction of the crack path (shown in dark blue) and interactions with the surrounding microstructure: **a** Entire segmented crack within the analyzed 3D volume, **b** cracking adjacent to large plate-like deformed grain 1, **c** cracking between deformed grain 1 and recrystallized grain 1, and **d** deviation of the crack around recrystallized grain 2. Reprinted from [29], Copyright (2022), with permission from Elsevier

olding techniques for diffraction spot segmentation [67], the ray tracing and Friedel pairs schemes for determining diffracted X-rays' direction [67], the GRAINDEX [91] and GrainSpotter [92] algorithms for grain indexing, and the Algebraic Reconstruction Technique (ART) [93], GrainSweeper [94], and forward-projection algorithms [95] for grain reconstruction (Fig 11b). For more detailed information, readers are directed to references

Table 1 A summary of imaging techniques used in destructive reconstruction during the processing and manufacturing of polycrystalline materials

Evolutionary processes	Imaging techniques	Microstructural features
Recrystallisation and grain growth	SEM [58]; EBSD [59]; OM [60].	Grain boundaries identification [60]; grain coarsening [59, 60]; grain refinement [59, 60].
Solidification	SEM [59]; EBSD [61]; OM [62].	Dendrite structure [62]; solidified grain structure [62].
Solid-state phase transformation	EBSD [31, 50].	Parent phase [47, 50]; phase boundaries [50, 63]; phase morphologies [31, 50].

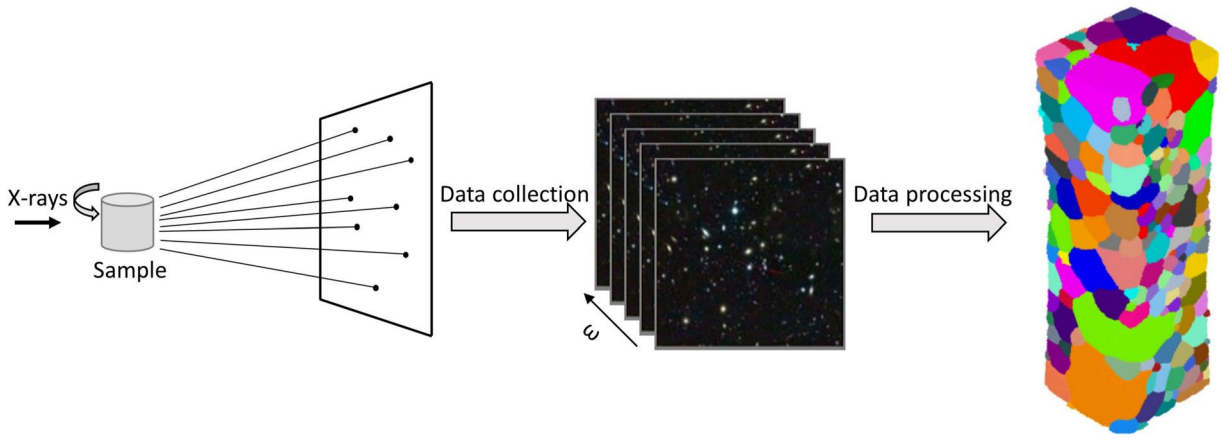

Fig. 9 The workflow of Non-destructive reconstruction

[25]. Recently, deep learning has advanced X-ray Bragg peak analysis in diffraction data processing [96]. Several software packages are available for X-ray data processing, including X-ray microtomography software Avizo [97], 3DXRD software IceNine [98], HEDM software [71] and DCT software [89].

- Space discretisation: This step identifies individual features within the digital microstructur using either grid or vertex-edge-face discretisation. Grain-based discretisation methods are commonly employed in the reconstruction of grain orientations [89, 99, 100], grain boundary migration [66], and strain fields [85, 101]. Similar to destructive reconstruction, two main techniques employed in the vertex-edge-face method are the marching cubes algorithm [24] and the CAD-based surfing fitting [100]. Several software packages are available for vertex-edge-face based discretisation in non-destructive reconstruction, including OOF2 [102] and Amira [103] (Fig 12).

Recent research in non-destructive reconstruction emphasizes enhancing experimental facilities to achieve accurate, efficient, and high-resolution reconstructions of polycrystalline microstructures. To address the resolution limitations of X-ray diffraction techniques, researchers have developed Nano X-ray Diffraction Computed Tomography (NXRD-CT) [74] and Dark Field X-ray Microscopy (DFXM) [104, 105] systems. Both methods achieve sub-micrometre spatial resolution but sacrifice temporal resolution due to their multi-dimensional scanning operations [64]. The scanning 3DXRD (S3DXRD) technique, achieved by narrowing the X-ray beam cross-section to sub-grain dimensions, enables the investigation of intragranular changes and the analysis of samples with multiple grains [84, 85, 101]. Topotomography (TT) enhances spatial and temporal resolution through a modified DCT acquisition geometry, allowing for imaging of individual grains with detector resolution tailored to the grain size [75, 106]. The technique has been integrated with DCT to achieve high-spatial-resolution grain orientation mapping [64] and bulk plasticity observation [89] (Fig 13). Laboratory X-ray Diffraction Contrast Tomography (Lab-DCT) is an emerging reconstruction technique that extends the applicability of DCT to home laboratories [68, 99]. This technique has proven valuable for investigating 3D grain structures and 4D (space and time) structural evolutions [78, 99]. Recent advancements in LabDCT include enhanced grain orientation mapping through DL-based data processing [107] and improved geometric measurement accuracy [99].

In addition to X-ray based reconstruction, TEM-based techniques such as Three-Dimensional Orientation Mapping in Transmission Electron Microscopy (3D-OMiTEM) [26,

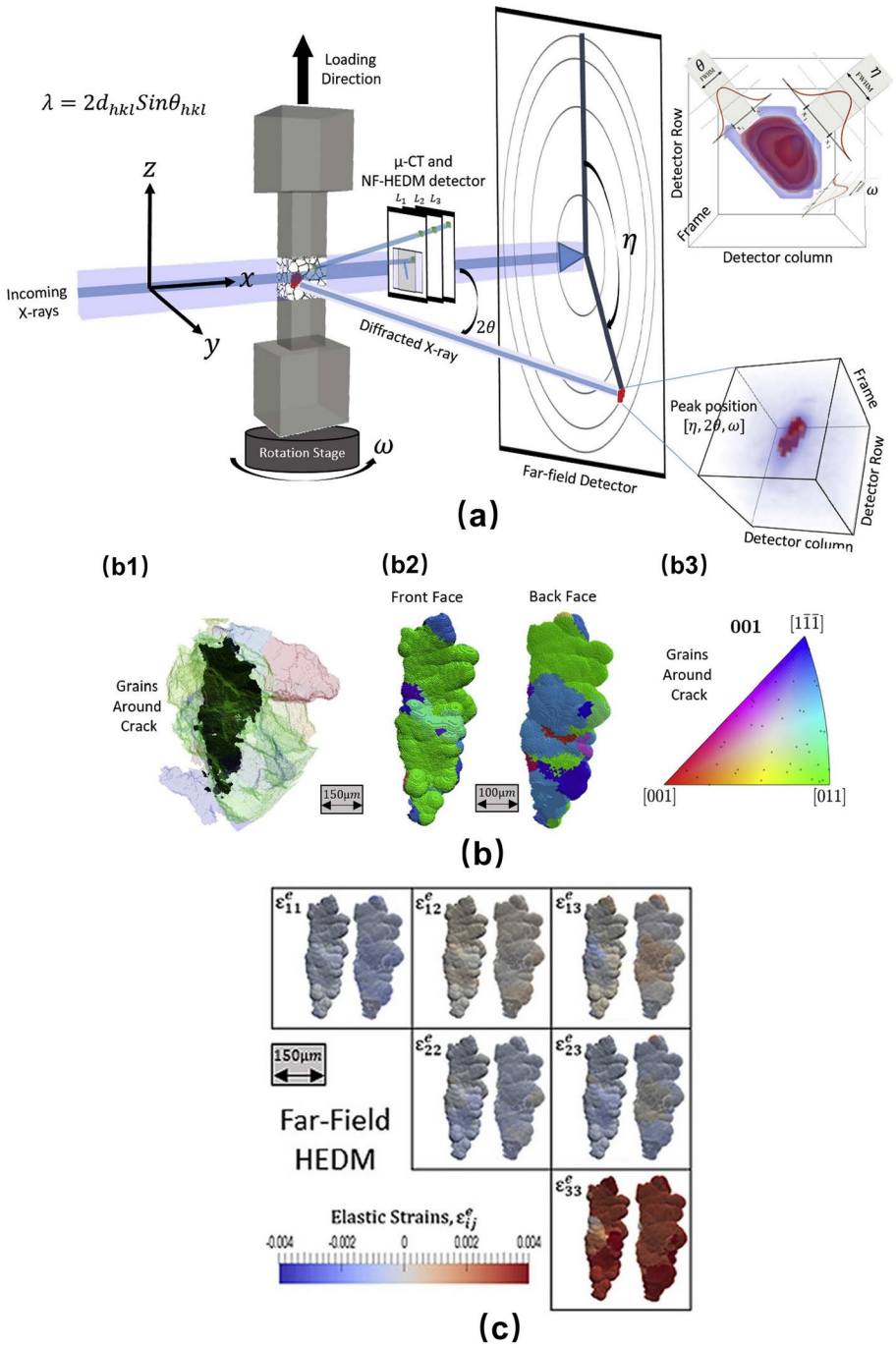

Fig. 10 Fatigue crack propagation and lattice strain characterisations using HEDM in a Ni-based superalloy: **a** schematic of the HEDM experimental setup, which includes μCT, NF-HEDM, FF-HEDM, and reciprocal space mapping, **b1** grains of interest surrounding the crack path, **b2** grains adjacent to the crack on the front and the back face, **b3** the orientation distribution of the grains adjacent to the crack, **c** grain average elastic strain tensor for each grain adjacent to the crack on the front and the back face. Adapted from [72], Copyright (2019), with permission from Elsevier

108] and Scanning Precession Electron Diffraction (SPED) [27] have been developed for non-destructive analysis of polycrystalline materials at the nanometer scale. Recently, the 3D-OMiTEM and SPED-based TEM techniques have been extensively employed to reconstruct polycrystalline microstructures and characterise features such as grains orientations [109, 110], precipitates [110], grain boundaries [26], and thermodynamic phases [27]. Detailed information on data collection, data processing, and software packages used in TEM-based reconstruction is available in the references [26, 27].

As illustrated in Table 2, non-destructive reconstruction has become a widely used technique to establish PSPP linkages in polycrystalline materials. In PS linkages for both traditional [78] and additive manufacturing [77], recent years have witnessed significant breakthroughs for understanding grain coarsening [78] (Fig 14a), and grain boundary migration [78] (Fig 14b) during recrystallisation and grain growth, dendrite growth [77] (Fig 15) during

Table 2 A summary of X-ray based imaging techniques for non-destructive reconstruction in polycrystalline materials

Imaging techniques	Collection types	Microstructural features	Properties and performance
Micro-computed tomography (μCT)	Absorption contrast	Minerals [24]; porosities [24].	–
Micro-computed tomography (μCT)	Phase contrast	Minerals [24]; porosities [24].	–
Synchrotron micro-computed tomography (S-μCT)	Absorption contrast	Precipitates [74]; grain boundaries [75]; thermodynamic phases [75]; porosities [69, 72, 75, 76]; dendrite growth [77].	Brittle fracture [75]; fatigue failure [72]; ductile failure [76].
Synchrotron micro-computed tomography (S-μCT)	Phase contrast	Grain boundaries [75]; thermodynamic phases [75]; grain structure [78]; porosities [75].	Brittle fracture [75]; fatigue failure [79].
Nano computed tomography (Nano-CT)	Phase contrast	Precipitates [74].	–
Nano X-ray fluorescence (Nano-XRF) microscopy	Absorption contrast	Grain boundaries [80].	–
Differential-aperture X-ray microscopy (DAXM)	Orientation data mapping	Grains orientations [81]; grain boundary migration [66]; phase boundaries and morphologies [82].	Elastic strain [83].
Scanning three-dimensional X-ray diffraction microscopy (S3DXRD)	Orientation data mapping	Grains orientations [84].	Intragranular strain [85] and stress [86] fields.
High-energy X-ray diffraction microscopy (HEDM)	Orientation data mapping	Grains orientations [87].	Lattice strain [72]; stress-strain evolution [51]; intragranular strain [88].
Diffraction contrast tomography (DCT)	Orientation data mapping	Grains orientations [64].	Intergranular stress corrosion cracking [73].
Topotomography (TT)	Orientation data mapping	Grain boundary migration [67]; grain coarsening [75].	Bulk plasticity [89].
Laboratory diffraction contrast tomography (LabDCT)	Orientation data mapping	Grains orientations [78], grain coarsening [78], grain boundary migration [78].	–

solidification, and thermodynamic phase boundaries and morphologies [82] during solid-state phase transformation. Integrating non-destructive reconstruction with DIC analysis [76] enables precise assessment of microstructural effects on micromechanical responses. For instance, HEDM combined with X-ray microtomography has been employed to study stress-strain evolution [51], ductile failure void coalescence [76] (Fig 16), and small fatigue crack propagation [72, 79] (Fig 10b). Additionally, advancements in non-destructive techniques have enhanced the investigation of intragranular strain, stress fields (Fig 17), and bulk plasticity (Fig 13). For more detailed information on SPP linkages through non-destructive reconstruction, readers are directed to the references listed in Table 2.

3 Physics-Based Models

Several techniques, including cellular automata, Monte Carlo methods, level set methods, and phase field methods, have been developed to reconstruct evolutionary processes in polycrystalline materials. Cellular automata and Monte Carlo methods discretise the domain with grids and update state variables at each grid through discrete time steps [111]. In contrast, level set and phase field methods track continuously the evolving position of time- and space-dependent interfaces through continuous motion functions [111]. The following subsections outline the workflows of these methods alongside their advantages and limitations.

3.1 Cellular Automata

Cellular Automata (CA) [111–113] models are based on three basic rules: (a) grid discretisation that divides the domain into discrete cells with different state features, (b) neighbourhood identification that finds each cell's closest neighbours, and (c) transformation rules that updates the state features of all cells. These rules guide the prediction of the spatial and temporal evolution of microstructures in polycrystalline materials, and execution procedure is summarized below.

- State generation: The analytical domain is discretised into cells, typically regular but also capable of accommodating random [114] and irregular configurations [115]. State variables, such as dislocation density and

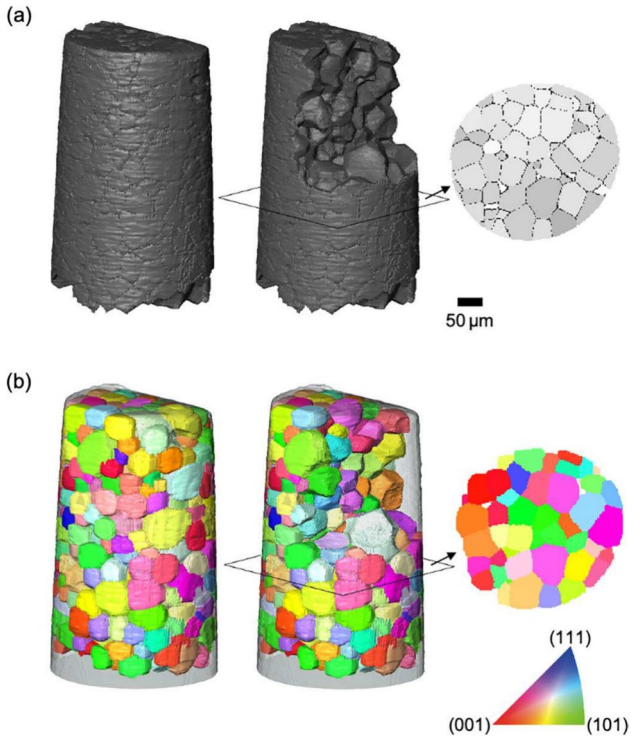

Fig. 11 **a** Internal grain structure reconstruction of the Ti-β21S sample using X-ray phase contrast microtomography; **b** Grains and orientation mapping using X-ray diffraction; Grains are coloured by crystallographic orientation according to the inverse pole figure. Reprinted from [78], Copyright (2021), with permission from Elsevier

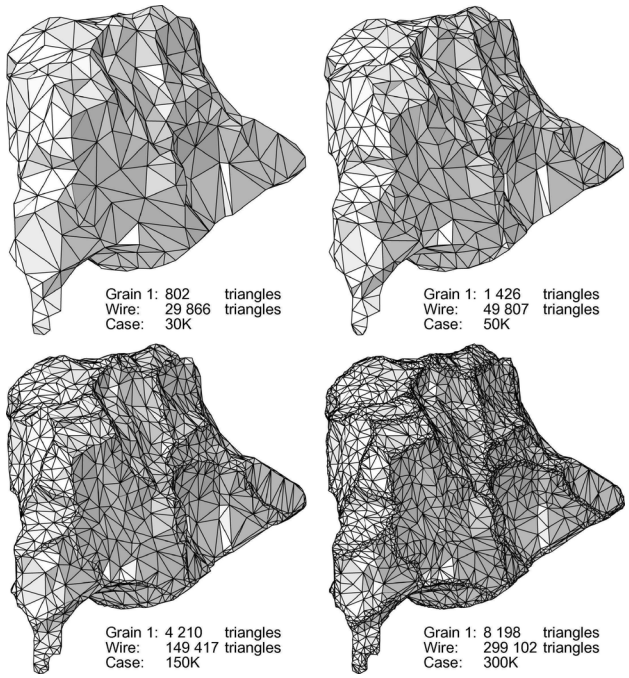

Fig. 12 Different levels of the vertex-edge-face-based grain reconstruction from the DCT data. Reprinted from [103], Copyright (2011), with permission from Elsevier

crystal orientation, are then assigned to each cell, with initial values determined through random initialisation [116], experimental data acquisition from physical samples [59], or extraction from simulation results [59].

- State update: Following state generation, state variables are updated through discrete time steps for all cells based on transformation rules. At each time step, the neighbourhood of each cell is identified (Fig 18), and transformation rules update each cell's state according to its previous state and the states of neighbouring cells. Both deterministic [117] and probabilistic [118] switching rules can be applied. A popular probabilistic criterion [119] is

$$w_{switch} = \frac{v}{v_{max}} \tag{1}$$

where w_{switch} is the local switching probability, v is the local grain boundary velocity [120] and v_{max} is the maximum velocity in the analytical domain for the previous time step.

CA models are widely used to explore PSPP linkages in polycrystalline materials due to their flexibility in selecting appropriate transformation rules. Table 3 presents the PSPP linkages in polycrystalline materials and assesses the benefits and drawbacks of evolutionary process reconstructions via CA models. CA models have been employed to reconstruct recrystallisation and grain growth evolution across various traditional manufacturing methods, including hot compression [119], hot tension [121], hot extrusion [122], hot rolling [123, 124], hot forming [125], heat-assisted incremental sheet forming [126], and annealing stages [127], as well as multi-pass compression and annealing [59]. These techniques take initial parameters such as grain size, orientation, boundary conditions, dislocation density, and thermo-mechanical factors (including temperature and strain rate) as input data [121]. Following the integration of thermal [125], mechanical [125], thermo-mechanical [125], nucleation [59], growth [111], dislocation density [111], and crystal plasticity models [121], the resulting output data reflect microstructural evolution, characterised by changes in grain sizes and shapes (Fig 19), as well as macroscopic properties such as flow stress [125], stress and strain response [121], stress and strain distribution [121], and dislocation density distribution [121]. Recrystallisation reconstruction through

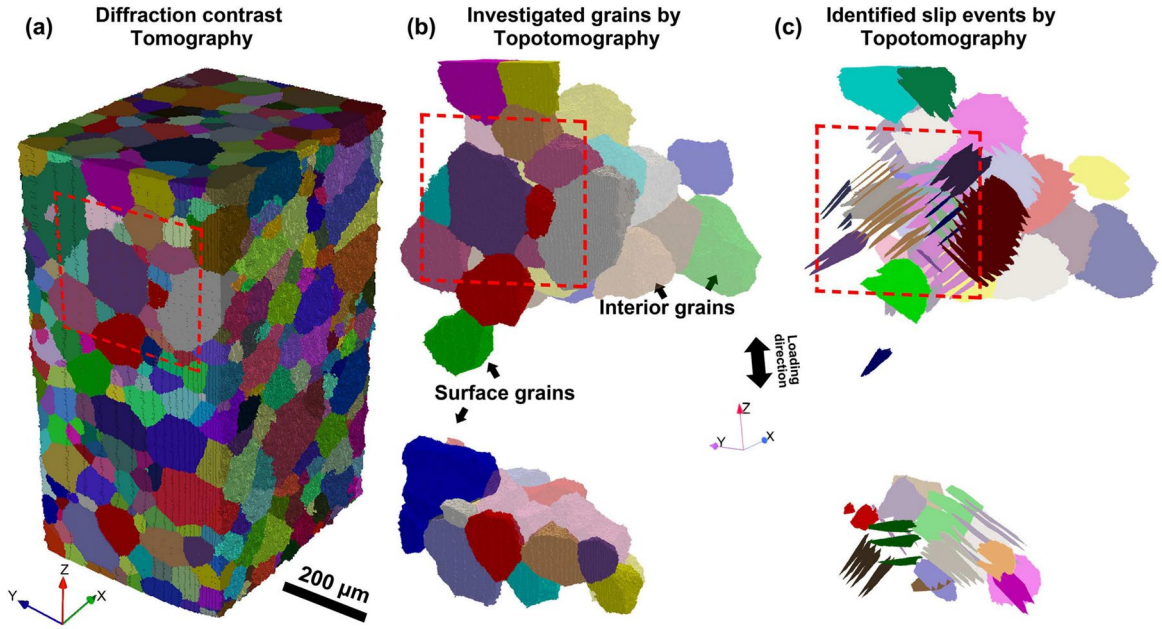

Fig. 13 **a** DCT reconstruction of the Ti-7Al specimen; **b** Investigation of interior and surface grains by TT; **c** Identification of bulk slip events by TT. Reprinted from [89], Copyright (2022), with permission from Elsevier

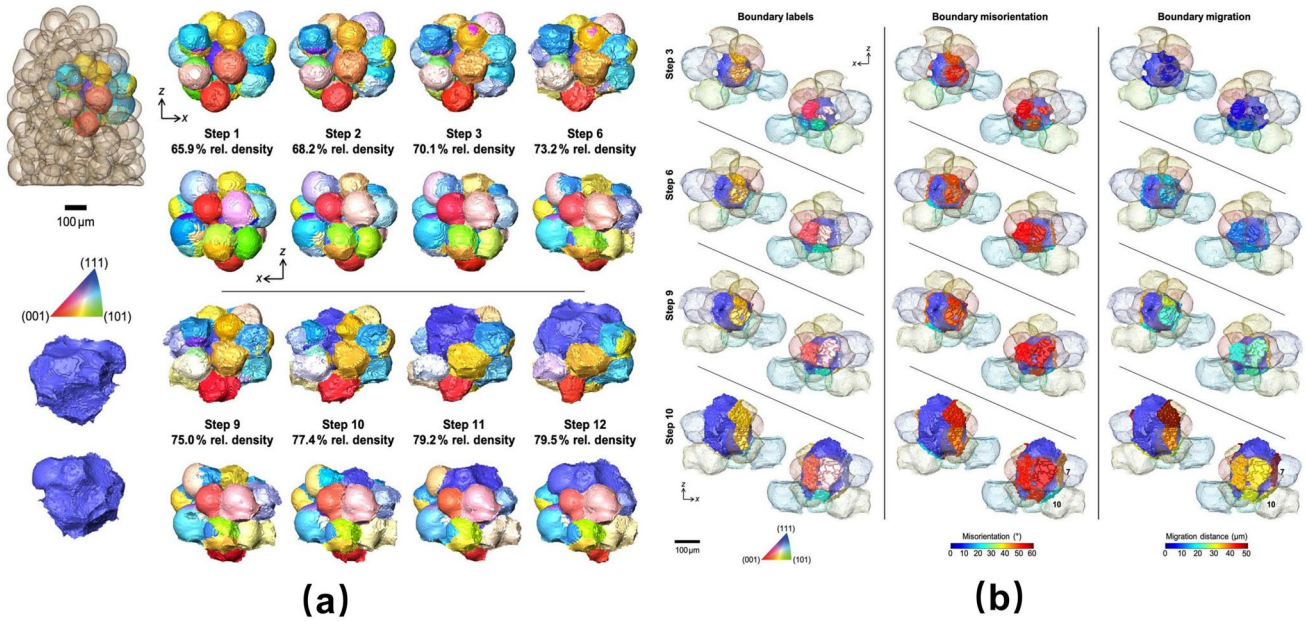

Fig. 14 **a** Time-lapse series of a fast-coarsening grain (blue color) in the selected region of interest (RoI) of powder metallurgy (illustrated left) during the sintering densification process. The top and bottom sequences for each time step show two different views of the ROI in the sample; **b** Time-resolved tracking of the grain boundaries of the fast-coarsening grain (solid) and several contacting grains (transparent) at selected time steps. The grains are colored by crystallographic orientation according to the inverse pole figure. Reprinted from [78], Copyright (2021), with permission from Elsevier

CA models is classified into Static recrystallisation (SRX) and Dynamic recrystallisation (DRX) [59]. For further details, readers are referred to [59] for SRX and [122] for DRX.

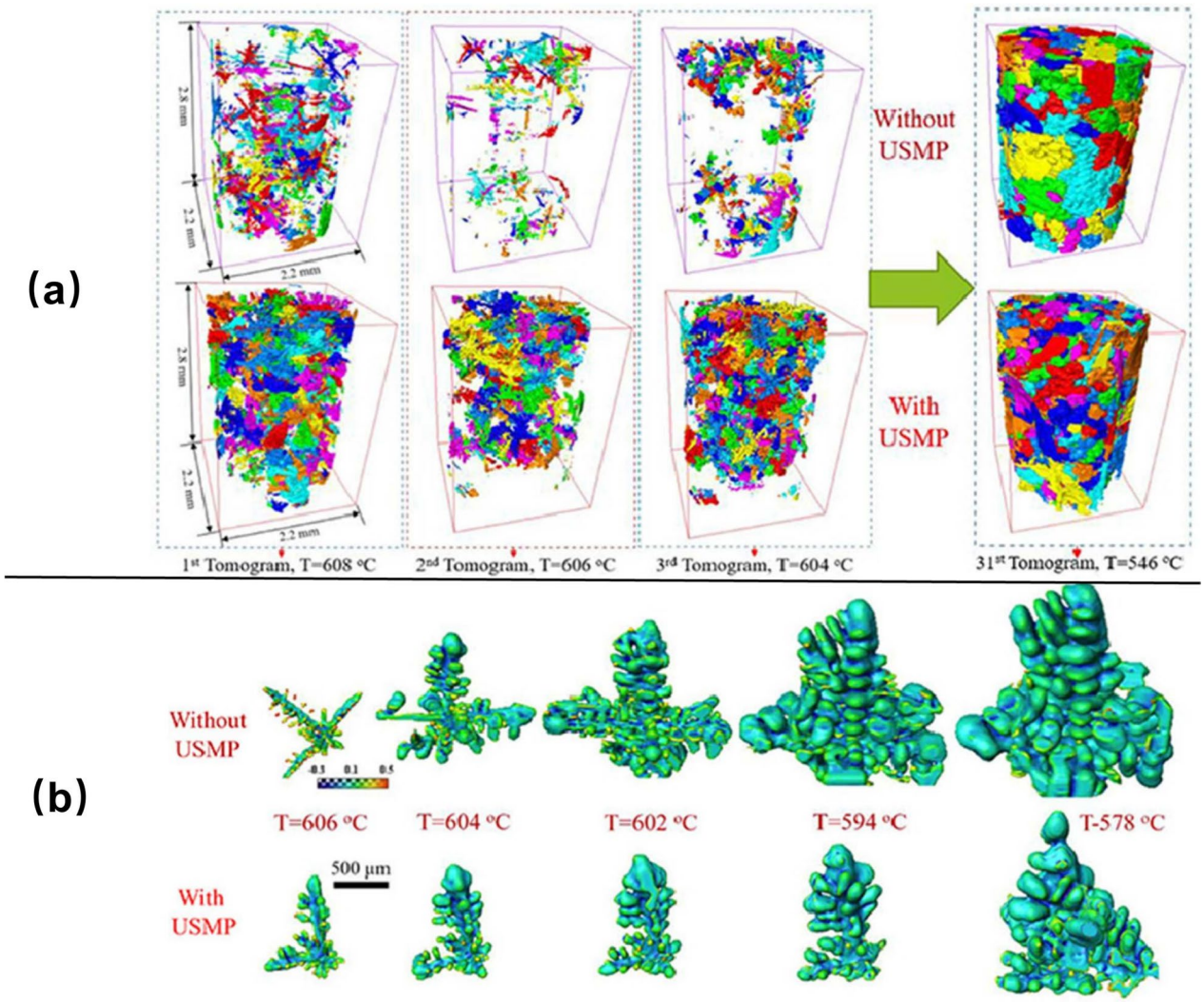

Fig. 15 **a** Volume renderings of the tomography scans of the Al dendrites in the absence and presence of ultrasound melt processing (USMP); **b** The growth and morphology evolution of individual Al dendrites in the absence and presence of USMP. Reprinted from [77], Copyright (2021), with permission from Elsevier

CA models for recrystallisation and grain growth reconstructions have seen significant advancements in recent years. For instance, researchers have integrated CA models with Crystal Plasticity Finite Element Method (CPFEM) [116, 121] and Finite Volume Method (FVM) [131] to improve predictive capabilities and tackle inhomogeneities and multi-scale deformation. A statistical ensemble CA model was introduced by [132] based on single units from a large bulk specimen, which exhibited remarkable accuracy and significantly reduced computational time. A three-dimensional Frontal Cellular Automata (FCA) model was developed by [123] for computation time reduction and 3D reconstruction (Fig 20). A Multilevel Cellular Automaton (MCA) model was developed by [125] to tackle the intricacies of recrystallisation nucleation and grain topological deformation. CA models provide several notable advantages for reconstructing recrystallisation and grain growth. Firstly, their grid discretisation structure is flexible and facilitates the capture of recrystallisation dynamics and topological characteristics [133]. Additionally, high spatial resolution can be achieved by adjusting the size of the discretisation cells [134]. Moreover, parallel computing is feasible since each cell's state update relies on data from its local neighbourhood, leading to enhanced computational efficiency [134]. Finally, the transformation rules in CA models also allow for easy calibration across various time and length scales. On one hand, these models can reconstruct recrystallisation and grain growth using straightforward transformation rules [111]. On the other hand, they can integrate thermodynamic, curvature-driven, and energy dissipation mechanisms into the transformation rules, enabling realistic characterisation of grain boundary migration [111]. The

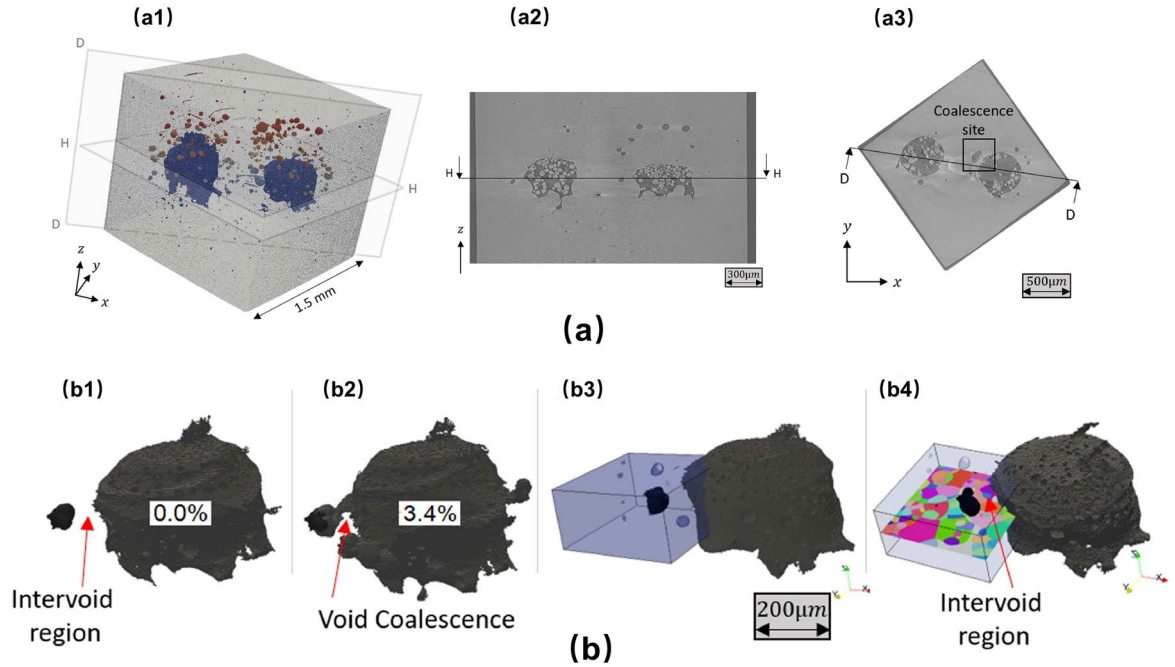

Fig. 16 Investigation of void coalescence in ductile failure using HEDM and μ-CT in a Ni-based superalloy: **a1** void distribution in the region of interest (ROI) determined through μ-CT, **a2** cross-section D of the ROI, **a3** cross-section H of the ROI. Extraction of the grain structure found through FF-HEDM reconstruction surrounding the coalescence site marked in **a3**: **b1** initial state before coalescence, **b2** at 3.4 % strain after coalescence, **b3** region extracted around the coalescence site, **b4** grain structure in the region of interest. Adapted from [76], Copyright (2020), with permission from Elsevier

limitations of CA models primarily stem from their aliased characterisation of interfaces and curvature. In these models, the interface comprises a single layer of cells separating two distinct local states (e.g., crystal orientations), leading to a stair-stepped structure with sharp discontinuities at edges and corners.

CA models are also extensively applied in reconstructing solidification evolution [135]. These techniques take state labels (e.g. solid, liquid, and void related to gas), grain information (e.g. grain ID, orientation, and envelope), and solidification parameters (e.g. temperature, diffusion coefficient, partition coefficient, and initial concentration) as input data [61]. Following the integration of thermal [61], nucleation [61], solute diffusion [59], growth [61], and crystal plasticity models [129], the resulting output data reflect microstructural evolution, characterised by changes in dendrite growth and solidified grain structure (Fig 21)), as well as macroscopic properties such as the stress and strain response and stress and strain distribution [129]. To establish PSPP linkages in solidification reconstructions, CA models must be integrated with numerical methods such as Lattice Boltzmann Method (LBM) [136], Finite Difference Method (FDM) [129], FVM [137], and CPFEM [61, 129] to model heat sources, heat transfer, fluid flow, and micromechanical behaviour. CA models for reconstructing solidification evolution were initially developed for the welding [138] and casting [139] processes. Recently, these techniques have been employed to reconstruct the solidification evolution of Additively Manufactured (AM) materials (Fig 22)). Examples of AM processes are Hybrid Deposition and Micro-Rolling (HDMR) [131], Laser Additive manufacturing (LAM) [112], Direct Laser Deposition (DLD) [61], Direct Energy Deposition (DED) [62], Powder Bed Laser Beam Melting (PB-LBM) [129], and Selective Laser Melting (SLM) [137].

Recent efforts in CA models for solidification reconstruction have centred on reducing computational cost and enhancing efficiency. For example, [141] introduced a high-efficiency Virtual Submesh Cellular Automata (VSCA) method to address the computational challenges associated with multiple orientations and large-scale reconstructions. Additionally, parallel computing has been successfully integrated into CA models, enhancing its capability to reconstruct solidification evolution in large 3D polycrystalline microstructures [140]. CA models for solidification reconstruction offer advantages similar to those found in recrystallisation and grain growth reconstruction, such as ease of implementation and high spatial resolution. CA models are also widely used for reconstructing solidified microstructures in additive manufacturing processes [113]. The accuracy of these reconstructions is enhanced by grounding CA models in the physics of dendritic tip kinetics

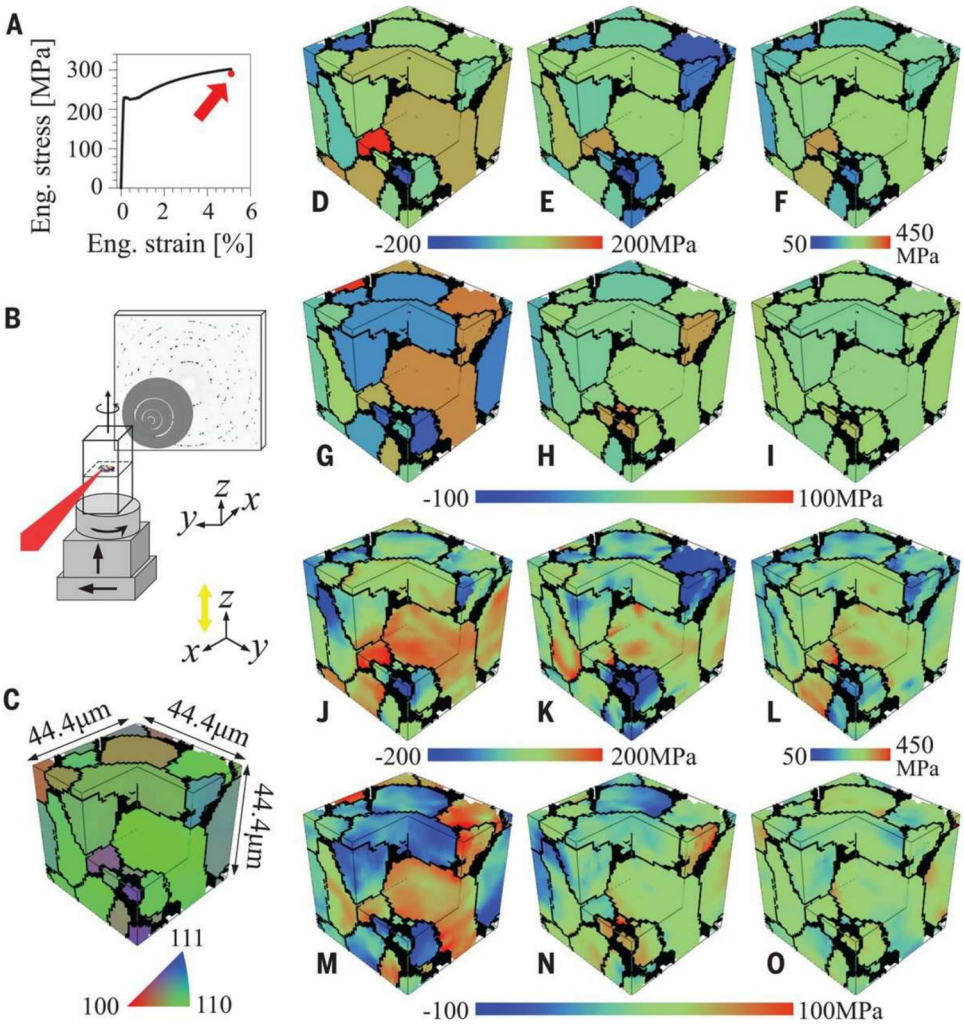

Fig. 17 3D intragranular local (type II) and grain-averaged (type III) stress tensor fields in plastically deformed bulk steel. **A** In situ stress-strain curve, after 5.1% of elongation, the scanning 3DXRD measurement was performed under an applied tensile force of 290 MPa, as represented by the arrow and dot in red; **B** Schematic diagram of the scanning 3DXRD setup; **C** 3D orientation map; **D** to **I** 3D type II fields of (**D**) σ_x (**E**) σ_y, (**F**) σ_z, (**G**) τ_{xy}, (**H**) τ_{yz}, and (**I**)τ_{zx}; **J** to **O** 3D intragranular type III fields of (**J**) σ_x, (**K**) σ_y, (**L**) σ_z, (**M**) τ_{xy}, (**N**) τ_{yz}, and (**O**)τ_{zx}. Reprinted from [86], Copyright (2020), with permission from "American Association for the Advancement of Science"

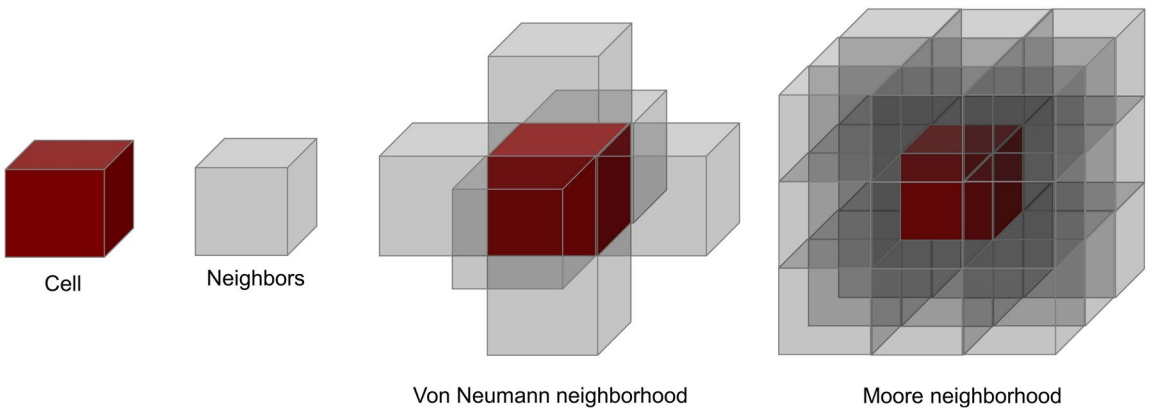

Fig. 18 Two common types of the neighbourhood for a cell in 3D cellular automaton: von Neumann neighbourhood and Moore neighbourhood

[142]. Additionally, CA models require less computational power [61] and can be applied to large 3D polycrystalline microstructures [141]. Finally, CA models utilize various techniques to assign crystallographic structures to grains, enabling the reconstruction of grain competition during solidification processes [113]. The main drawback of CA models for solidification reconstruction is their reliance on a single layer of cells to characterise the liquid-solid interface,

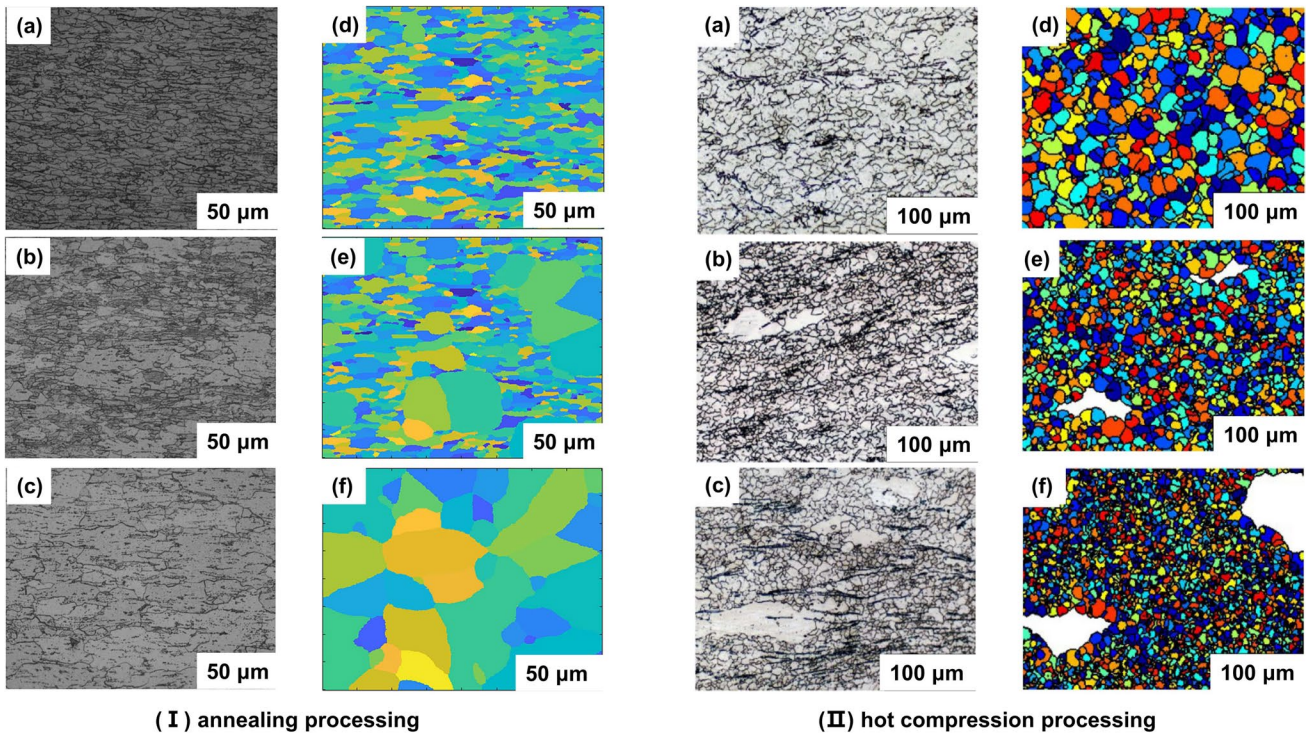

Fig. 19 Reconstructd recrystallisation and grain growth (**a**-**c**) using cellular automata and corresponding experimental comparison (**d**-**f**) of polycrystalline microstructures for grain coarsening and refinement at different stages under annealing (I), adapted from [127], Copyright (2022), with permission from Elsevier, and hot extrusion processing (II), adapted from [128], Copyright (2022), with permission from Elsevier

complicating the depiction of solute trapping phenomena. Additionally, dendrite tip kinetics in CA models typically assume local equilibrium, which becomes invalid under rapid cooling scenarios [113]. Furthermore, the grid discretisation inherent in these techniques limits their ability to accurately characterise finer microstructures, such as higher-order dendritic branches [61].

CA models have also been effectively employed to reconstruct solid-state phase transformations. These techniques take phase state variables, grain orientation, grain boundary, and phase transformation parameters (like solute concentration and temperature) as input data [133]. Following the integration of thermal [116], mechanical [133], thermo-mechanical [116], nucleation [133], growth [133], diffusion [143], and crystal plasticity [133] models, the resulting output data reflect microstructural evolution, characterised by changes in nucleation, growth, and impingement (Fig 23)), as well as the macroscopic properties such as stress and strain response [130]. CA models have been coupled with CPFEM [130, 144], LBM [145], and FVM [146] for flow, heat transfer, diffusion, and multi-scale deformation analyses. Researchers have employed CA models to reconstruct solid-state phase transformations in both traditional and additive manufacturing. Traditional manufacturing examples include cooling stages [147], annealing stages [148], grind-hardening [149], and multi-pass hot-rolling and cooling [144]. In additive manufacturing, methodologies such as SLM [150], Electron Beam Selective Melting (EBSM) [150, 151], and DED [143] have been applied. Like solidification, recrystallisation, and grain growth reconstructions, CA models for solid-state phase transformation reconstruction offer high spatial resolution and are straightforward to implement, avoiding the need to solve complex partial differential equations. These techniques effectively capture various aspects of microstructural physics in solid-state diffusional phase transformations [133]. Furthermore, CA models are computationally efficient due to their discrete structure, which is well-suited for parallel computing. However, they exhibit an aliased characterisation of the interface and curvature between thermodynamic phases, complicating the precise calculation of mean curvature.

3.2 Monte Carlo Methods

Monte Carlo (MC) models, derived from the Ising and Potts models [111, 112, 133], perform quantitative analysis of practical polycrystalline microstructures through probabilistic sampling. At each time step, a set of random states is generated and evaluated on discrete lattices until

Table 3 A summary of cellular automata for physical reconstructions in polycrystalline materials

Evolutionary processes	Properties and performance	Advantages	Disadvantages
Recrystallisation and grain growth	Flow stress and strain [127]; stress and strain response [121]; dislocation density distribution [121]; stress and strain distribution [121].	Easy implementation; high spatial resolution; high computational efficiency; complex recrystallisation reconstruction and realistic grain boundary migration characterisation.	Aliased characterisation of interface and curvature between grains.
Solidification	Stress and strain response and stress and strain distribution [129].	Easy implementation; high spatial resolution; the most prevalent; high accuracy reconstruction; low computation power; large 3D polycrystalline microstructures; crystallographic structure characterisation.	Aliased characterisation of solute trapping; weak characterisation of higher-order dendrites branches; invalid reconstruction under rapid cooling conditions.
Solid-state phase transformation	Stress and strain response and stress and strain distribution [130].	Easy implementation; high spatial resolution; complex microstructure physics characterisation; high computational efficiency.	Aliased characterisation of interface between thermodynamic phases; less accuracy.

the desired polycrystalline microstructure is realised. The workflow is summarised below.

- State generation: Like CA models, the analysis domain is first discretisad into lattices, and then mapped into a polycrystalline configuration to form N lattice sites. Each lattice site s_i corresponds to a single grain, which is represented by a set of neighbouring lattices that share the same crystal orientation. Initial lattice states (e.g., thermodynamic phases, dislocation densities and crystal orientations) can be determined by random initialisation [152], experimental data acquisition from physical samples[153], or extraction from simulation results [154]. Subsequently, the total energy E of the analysis domain can be defined as [111]

$$E = \sum_{i=1}^{N} \left(\sum_{j=1}^{n} \frac{1}{2} \gamma(s_i, s_j) + E_s(s_i) \right) \tag{2}$$

  where n is the number of neighbouring lattice sites for each lattice site s_i, E_s indicates the stored density energy at the lattice site s_i, and the grain boundary energy $\gamma(s_i, s_j)$ on lattice sites can be expressed as [112]

$$\gamma(s_i, s_j) = J \sum_{j=1}^{n} \left(1 - \delta_{O_{s_i} O_{s_j}} \right) \tag{3}$$

  where J is a constant, δ denotes the Kronecker symbol, and O_{s_i} and O_{s_j} are orientations of the current lattice site s_i and its neighbour. Enhanced versions of Equation 2 and Equation 3, which account for grain boundary angles and anisotropic effects, are detailed in [155].
- State update: Following state generation, grain nucleation and growth are initiated to release the stored energy. Subsequently, lattice states and sites are updated, and the energy change ΔE from Equation 2 is computed to assess the acceptance or rejection of grain nucleation and growth. A popular probability criterion is given below [134]:

$$w_{switch}(\Delta E) = \frac{1}{2} w_0 \left[1 - tanh\left(\frac{\Delta E}{2kT_s} \right) \right] \tag{4}$$

  where w_{switch} is the switching probability, w_0 is the reduced mobility, k is the Boltzmann constant and T_s is the temperature. A random number $\varepsilon \subset [0, 1]$ is created for each step: if $\varepsilon \leq w_{switch}$, the energy change is approved; otherwise, it is denied. Another frequently used probabilistic criterion can be stated as [112]:

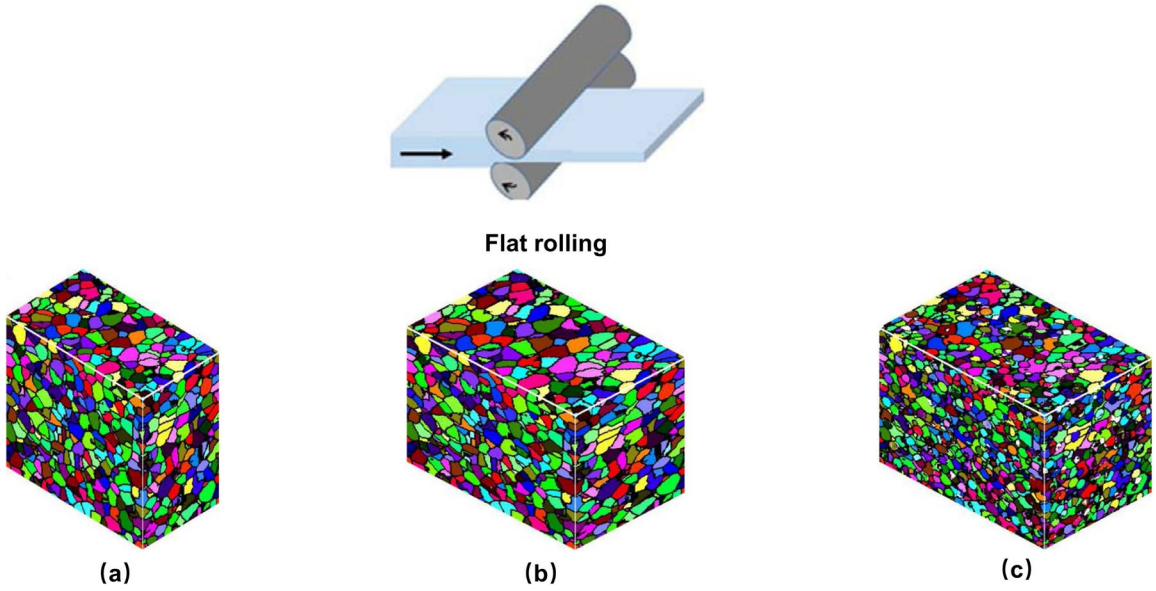

Fig. 20 Reconstructd recrystallisation using the 3D frontal cellular automata under flat rolling processing: **a** before the flat rolling, **b** after the flat rolling, **c** after the cooling. Adapted from [123], Copyright (2018), with permission from Elsevier

$$P = \begin{cases} 1, & \Delta E \leq 0 \\ exp\left(\frac{-\Delta E}{kT_s}\right), & \Delta E \geq 0 \end{cases} \tag{5}$$

Grain nucleation and growth are accepted when ΔE decreases. When ΔE increases, grain nucleation and growth are accepted with Boltzmann probability. Enhanced versions of Equation 5, which account for grain boundary mobility, are detailed in [155].

MC models, employing a probabilistic approach based on lattice site reorientation, are highly effective for tackling problems across various length and time scales [112]. Consequently, they are widely applied to reconstruct the evolutionary processes of recrystallisation, grain growth, solidification, and solid-state phase transformations in polycrystalline materials. MC models for recrystallisation and grain growth reconstructions take initial parameters such as grain size [156], grain orientation [155], grain boundary [153], dislocation density [111], and thermomechanical parameters (like temperature and strain rate) [157] as input data. Following the integration of thermal [111], mechanical [111], thermo-mechanical [158], nucleation [111], dislocation density [111], and crystal plasticity [159] models, the resulting output data reflect microstructural evolution, characterised by changes in grain sizes and shapes (Fig 24)), as well as the macroscopic properties, including flow stress [152], yield stress [158, 160], hardness [160], stress and strain response [159], stress and strain distribution [158, 159], dislocation density distribution [159], and damage initiation [158]. At each time step, grain nucleation occurs by introducing new grains at random points along grain boundaries. Each new grain consists of a small group of adjacent lattices with new orientation and zero stored energy [111]. Grain growth occurs by aligning the orientation of a randomly selected lattice site with that of its nearest neighbours [111]. MC models effectively reconstruct both SRX and DRX. For further details, readers are refered to [161] for SRX and [111] for DRX. Researchers have employed MC models to reconstruct the evolution of recrystallisation and grain growth processes in both traditional and additive manufacturing. Traditional manufacturing examples include annealing stages [162], hot rolling [152], hot extrusion [161], and equal channel angular extrusion [159]. In additive manufacturing, relevant methodologies include Powder Bed Fusion (PBF) [154], DED [154], Friction Stir Additive Manufacturing (FSAM) [163], and SLM [158]. MC models have integrated CPFEM [154, 154] to analyse heat transfer, thermo-mechanical behaviour, and multi-scale deformation.

MC models provide significant advantages for reconstructing recrystallisation and grain growth due to their simplicity of implementation, alongside moderate computational requirements [111]. The high efficiency of MC models is especially significant considering the algorithm's substantial potential for parallelisation [133]. However, MC models do not incorporate transformation rules, leading to reconstruction times unrelated to the actual physical processes. Thus, MC reconstruction outcomes do not adequately capture grain boundary-changing mechanisms. The grain growth index obtained from MC models also often diverges from its theoretical counterpart [111]. Consequently, scaling

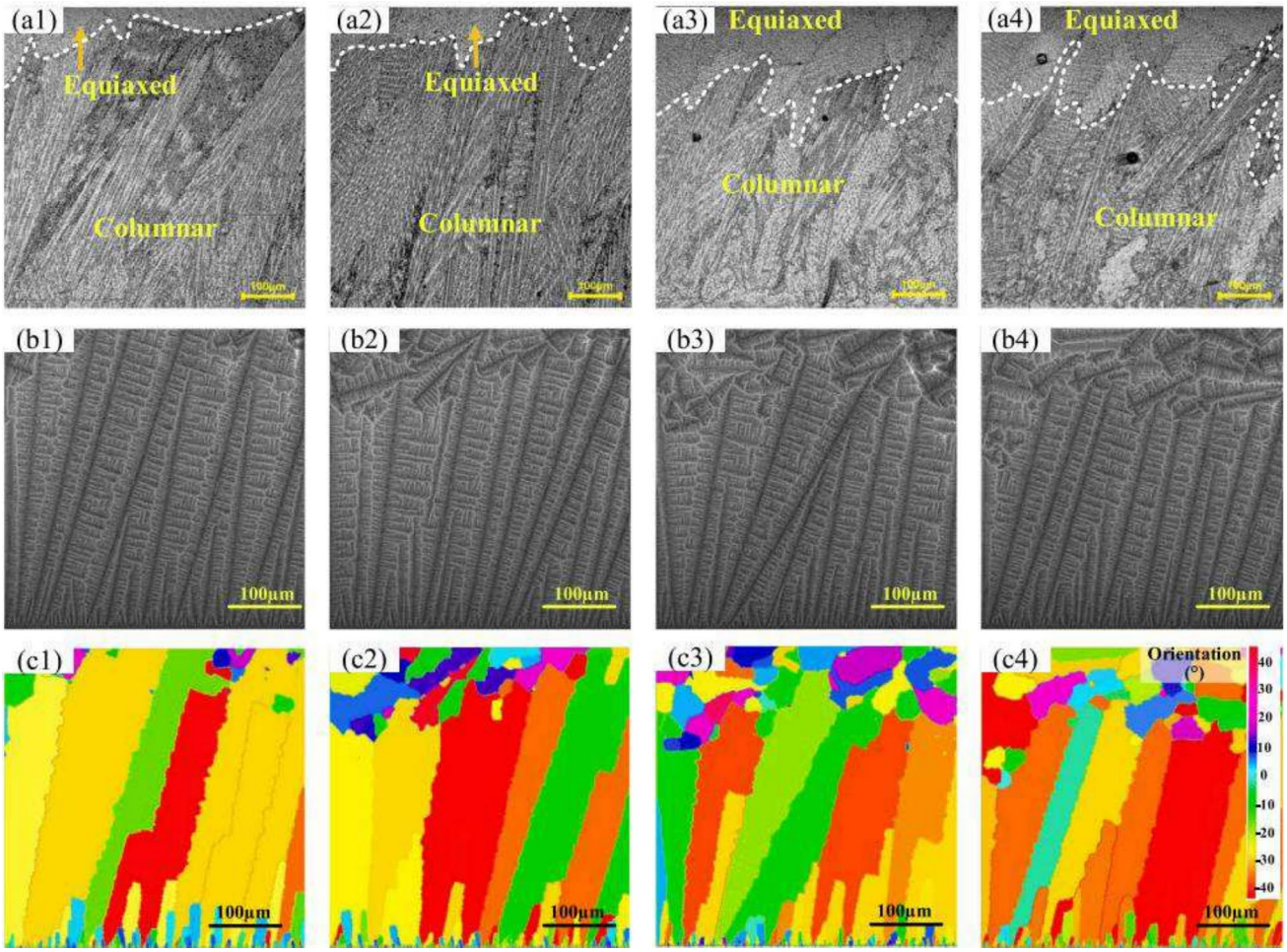

Fig. 21 Microstructures under different processing parameters: **a1**-**a4** dendrite structure reconstructed by experiment; **b1**-**b4** dendrite structure from CA reconstruction; **c1**-**c4** solidified grain structure from CA reconstruction. Reprinted from [62], Copyright (2022), with permission from Elsevier

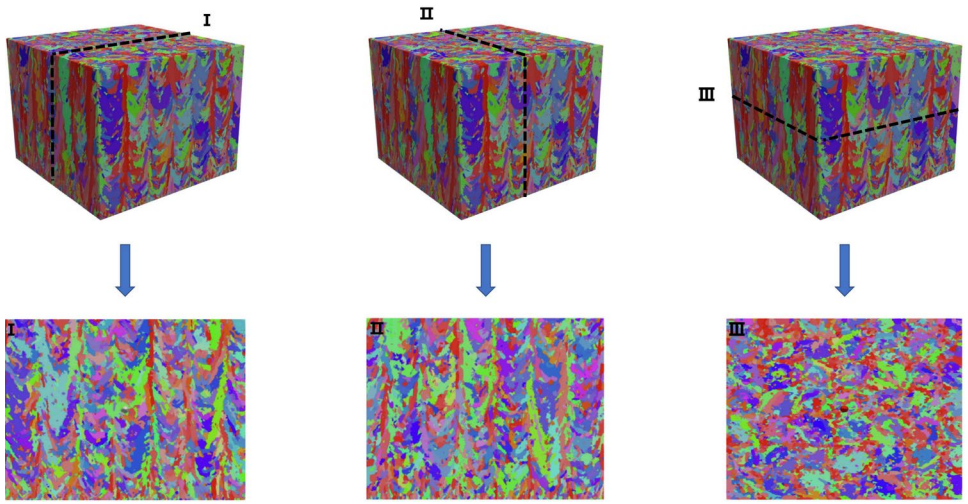

Fig. 22 Reconstruction of the solidified grain structure through cellular automata in additive manufacturing. Adapted from [140], Copyright (2021), with permission from Elsevier

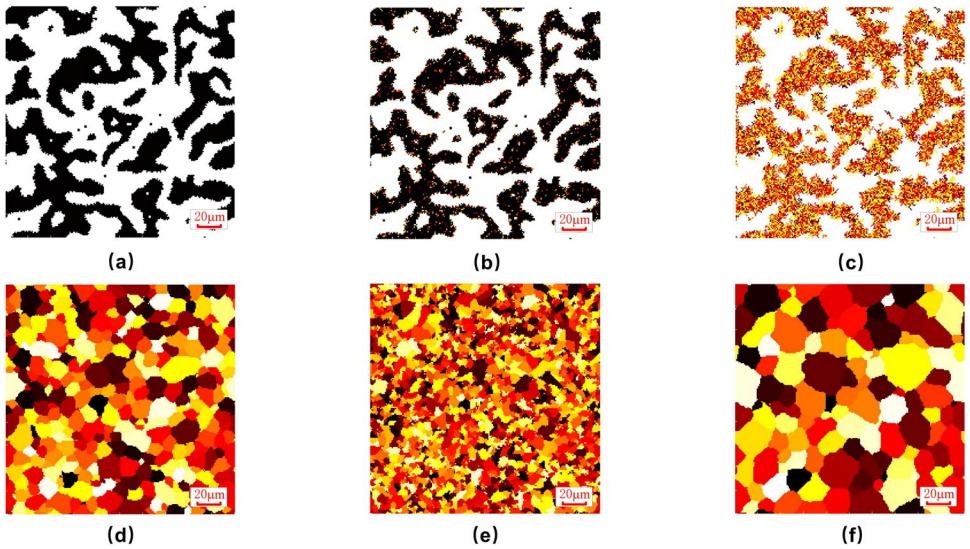

Fig. 23 Austenite transformation reconstruction using cellular automata at different evolutionary stages. **a**-**c** White means ferrite, black means pearlite and other colors mean austenite grains with different crystallographic orientations; **d**-**f** Different colors mean austenite grains with different crystallographic orientations. Open access from [149]

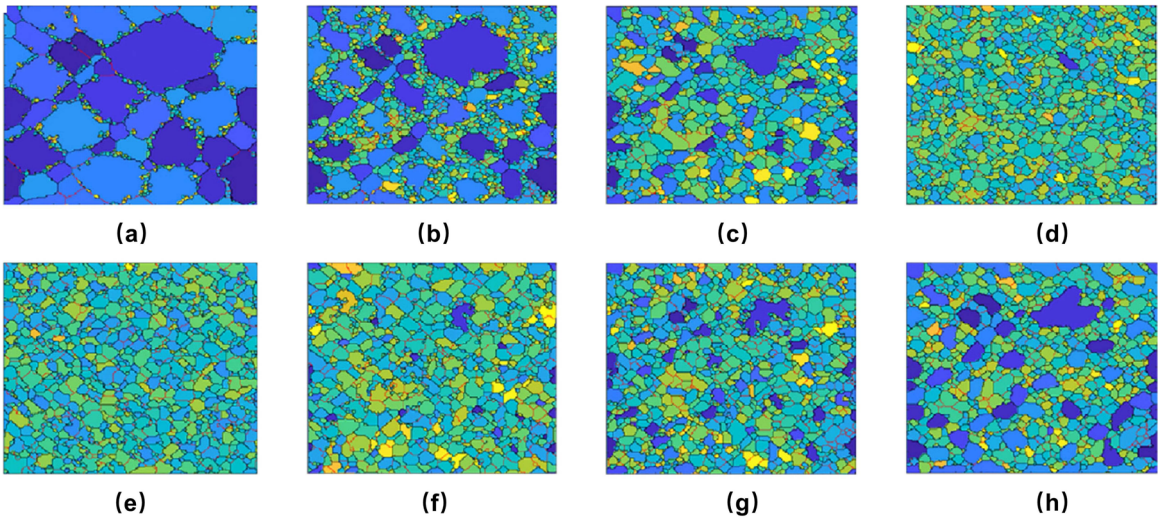

Fig. 24 Reconstructions of recrystallisation and grain growth using MC models: **a**-**d** grain refinement; **e**-**h** grain coarsening; Adapted from [157], Copyright (2021), with permission from Elsevier

or synchronising MC reconstruction time with real-time conditions is usually necessary [157].

The initial lattice states reconstructing solidification evolution in MC models are set to zero, indicating a liquid state. Following the integration of thermal, nucleation, and diffusion models, the output data reflect microstructural evolution, characterised by changes in solidified grain structures (Fig 25)). At each time step, grain nucleation is initiated by introducing nucleation sites to the liquid lattice states. Concurrently, grain growth occurs by aligning the orientation of a randomly selected lattice site with that of its nearest neighbours [164]. MC models for solidification reconstructions share advantages with recrystallisation and grain growth reconstructions, particularly regarding ease of implementation and low computational cost. Additionally, MC models demonstrate significant potential for capturing the morphology of AM microstructures [140] (Fig 26). However, they have limitation to characterise crystallographic texture [113, 165, 166], and are restricted to solid-state grain growth without consideration of growth kinetics [113]. The open-source software package SPPARKS supports solidification reconstructions using MC models [167].

MC models for solid-state phase transformation reconstructions take phase labels, phase boundaries, and phase transformation parameters (like diffusion coefficient and temperature) as input data. After incorporating the thermal, nucleation, and diffusion models, the resulting output data reflect microstructural evolution, characterised by the rearrangement of thermodynamic phases involving nucleation, growth, and impingement [133, 164]. At each time

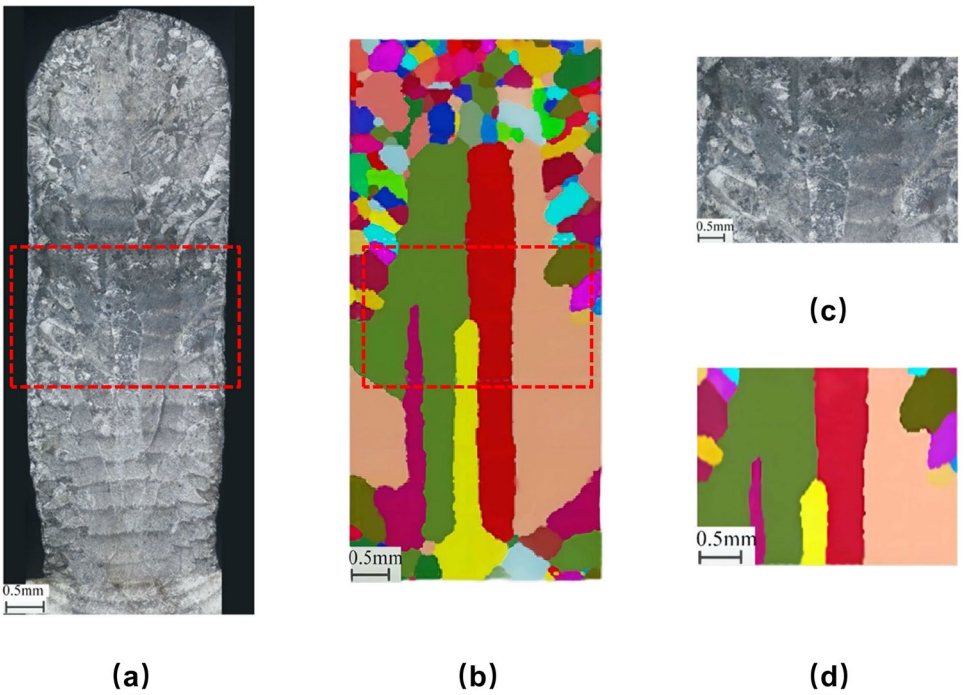

Fig. 25 Reconstruction of solidified grain structures from experiment and MC models: **a** experiment; **b** MC models; **c** enlarged illustration of experiment; **c** enlarged illustration of MC models. Adapted with permission from [164], 2022, Spring

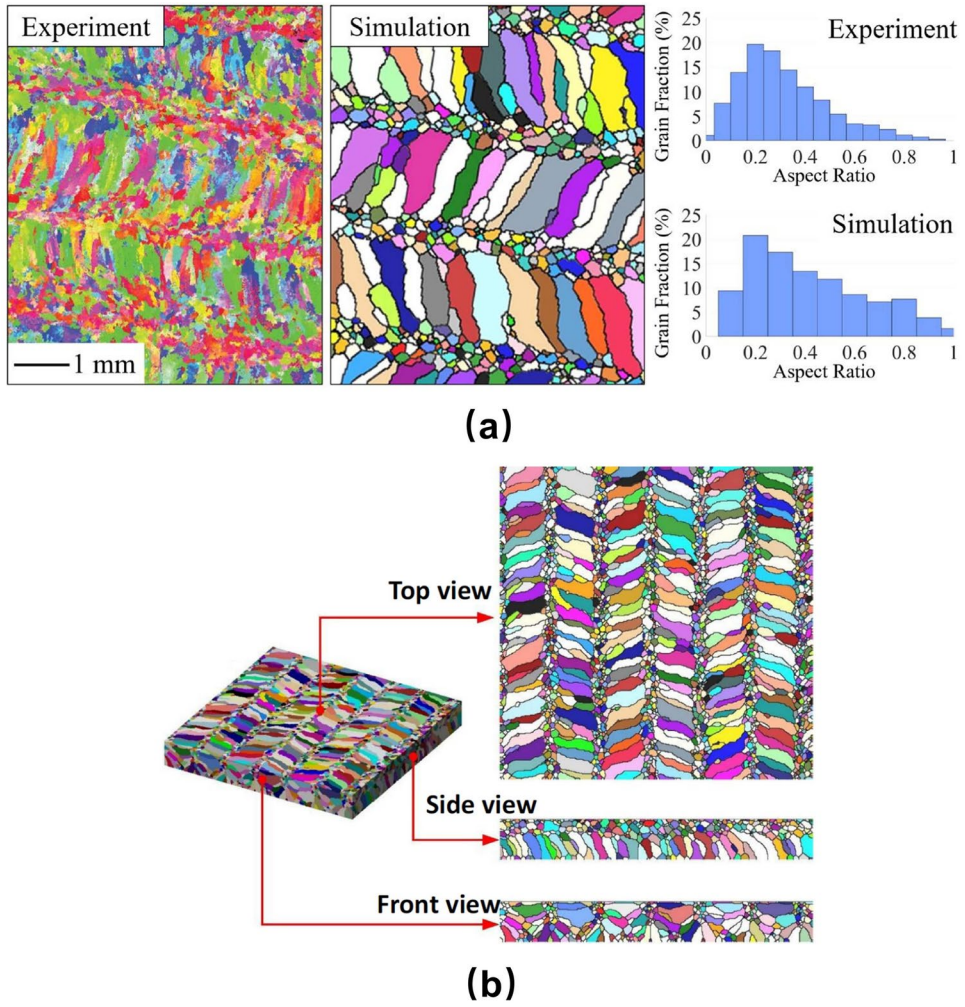

Fig. 26 Solidification reconstruction using MC models in additive manufacturing: **a** comparison between experiment and MC reconstruction; **b** 3D solidification reconstruction using MC models. Reprinted with permission from [168], 2019, Spring

step, new phase nucleation occurs by introducing nucleation sites along phase boundaries, while the migration of the new phase interface is governed by growth probabilities in various directions [164]. Like recrystallisation, growth, and solidification reconstructions, MC models for solid-state phase transformation reconstructions offer low computational costs and straightforward implementation without solving complex partial differential equations. However, state updates in MC models are dictated by minimising total energy, whereas CA models exhibit greater flexibility by aligning state updates with specific experimental systems. Consequently, MC models often lack explanations of physical length and time scales, complicating comparisons with experimental results [133, 169].

3.3 Phase Field Methods

In Phase Field (PF) models [112, 133], polycrystalline microstructures are represented by phase field variables, with grain boundaries depicted as diffuse transition interfaces. Partial differential equations describe the evolution of grain boundaries, while phase field variables are obtaiend through numerical solutions. The key workflow is outlined below.

- State generation: The phase field variables in PF models are classified into conserved variables, which convey composition information such as solute concentration, molar volume, and density [170], and non-conserved variables, which provide structural information, including grains and phases [171]. The total free energy in PF models is then defined as a function of state variables (e.g., temperature T, pressure p, stress/strain), along with phase field variables and their gradients [172], written as

$$F = \int_V f(c_1, c_2, ..., c_N, \eta_1, \eta_2, ..., \eta_K, \bigtriangledown c_1, \bigtriangledown c_2, ..., \bigtriangledown c_N, \bigtriangledown \eta_1, \bigtriangledown \eta_2, ..., \bigtriangledown \eta_K, p, T, ...)\, dV \tag{6}$$

  where c_i, $i = 1, 2, ..., N$ and η_j, $j = 1, 2, ..., K$ are the conserved variables and non-conserved variables respectively, N and K are the corresponding number of conserved variables and non-conserved variables, V is the entire volume of the analysis domain, f denotes the energy density, which includes (1) gradient terms relating to the energetic cost of interfaces (e.g. the interfacial free energy density [173] during solidification processes, the grain boundary energy density [171] and the gradient energy density [174] during recrystallisation and grain growth processes, and the gradient energy density [175] during solid-state phase transformation processes), (2) bulk energy density terms as a function of phase field variables, state variables, and external stimuli (e.g. the bulk free energy density [173] during solidification processes, the local free energy density [176], the potential energy density [174], the bulk free energy density [176], and the stored energy density [174, 176] during recrystallisation and grain growth processes, the chemical energy density [177], the elastic strain energy density [177], and the thermal energy density [177] during solid-state phase transformation processes), and (3) a potential with local minimums in two or more coexisting phases (e.g. the local free energy density [178] during solid-state phase transformation processes).
- Governing equation: After establishing the total free energy, the evolution laws for conserved variables c_i and non-conserved variables η_k are derived using the Cahn-Hilliard equation [179] equation and time-dependent Ginzburg-Landau (or Allen-Cahn) equation [180] respectively.

$$\frac{\partial c_i}{\partial t} = \bigtriangledown \cdot \left[D_{c_i} \bigtriangledown \left(\frac{\delta F}{\delta c_i} \right) \right] = \bigtriangledown \cdot \left[D_{c_i} \bigtriangledown \left(\frac{\partial f}{\partial c_i} - \bigtriangledown \cdot \frac{\partial f}{\partial \bigtriangledown c_i} \right) \right], \quad i = 1, 2, ..., N$$
$$\frac{\partial \eta_j}{\partial t} = -L_{\eta_j} \frac{\delta F}{\delta \eta_j} = -L_{\eta_j} \left(\frac{\partial f}{\partial \eta_j} - \bigtriangledown \cdot \frac{\partial f}{\partial \bigtriangledown \eta_j} \right), \quad j = 1, 2, ..., K \tag{7}$$

  where D_{c_i} and L_{η_j} are the kinetic coefficients related to atomic diffusion and interfacial mobilities.
- Discretisation and numerical solution: Grid [181] (e.g., multilevel grid (Fig 27a)) and vertex-edge-face-volume [181] (e.g., adaptive mesh refinement (Fig 27b)) discretisation methods have been used in PF models to define interfacial regions and track complicated interfacial dynamics. Equation 7 can be solved using numerical methods, including FDM [182], Spectral Method (SM) [173], and FEM [183]. In recent years, mesh-free methods have emerged as an alternative to grid-based and vertex-edge-face-volume discretisation schemes. For instance, smoothed particle hydrodynamics [184] constructs interfacial regions and dynamics from scattered points, eliminating the need for explicit mesh connectivity. Additionally, ML methods have been implemented to solve Equation 7 [172]. Several open-source software packages for PF models are available, including PRISMS-PF [185] and MMSP [186].

PF models directly incorporate phase transition thermodynamics into the governing equations, which automatically account for interface complexities such as normal vectors and curvature, leading to their widespread use in reconstructing evolutionary processes related to solidification, solid-state phase transformation, recrystallisation, and grain growth [184]. Table 4 presents the application of PF models and their strengths and drawbacks. In PF models for

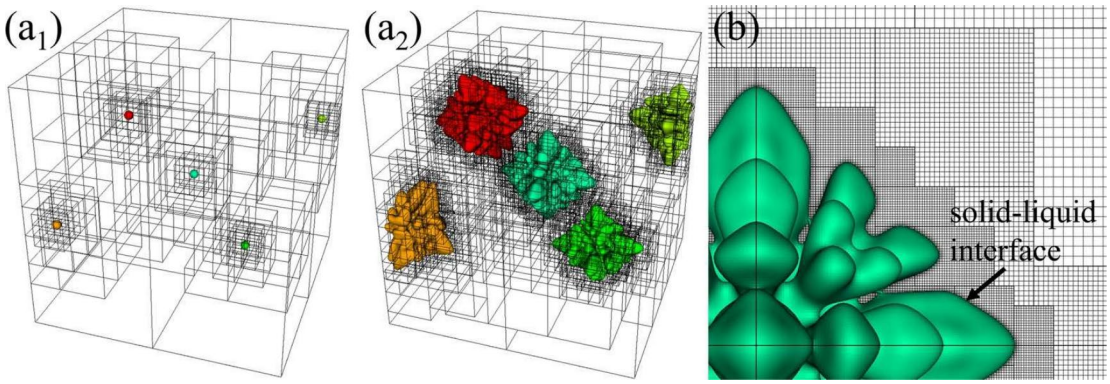

Fig. 27 ($a_1 - a_2$) Multilevel grid architecture superimposed on the multidendrite contours; **b** Illustration of the adaptive mesh refinement near solid-liquid interfaces. Adapted from [181], Copyright (2021), with permission from Elsevier

recrystallisation and grain growth reconstruction, non-conservative variables η_k are introduced to define grain regions, where $\eta_k = 1$ denotes the interior of grain k, $\eta_k = 0$ indicates the region outside grain k, and η_k transitions from 1 to 0 at the grain boundaries [174]. The total energy density f could encompass a combination of potential energy density, gradient energy density, and stored energy density [174]; local energy density, gradient energy density, and stored energy density [187]; or grain boundary energy density and stored energy density [171]. Following the integration of thermal [176, 188], mechanical [174], thermo-mechanical [189], nucleation [174], growth [190], dislocation density [174], and crystal plasticity [191] models, the resulting output data reflect microstructural evolution, characterised by changes in grain sizes and shapes (Fig 28 and Fig 29), as well as the macroscopic properties, including thermal conductivity [176], flow stress and strain [190], stress and strain response [174], and stress and strain distribution [189]. PF models effectively reconstruct both SRX and DRX. For further details, readers are referred to [192] for SRX and [193] for DRX. Numerical methods, such as CPFEM [189, 192], have been incorporated into PF models to simulate heat transfer, thermomechanical behaviour, and multi-scale deformation. PF models have been applied to reconstruct recrystallisation and grain growth processes in traditional and additive manufacturing. Traditional manufacturing processes include annealing stages [176], cold rolling [194], and hot working [174]. Methodologists involved in AM processes are mainly Friction Stir Welding (FSW) [195].

In recent years, there has been significant interest in understanding how bubbles [194], voids [171], plastic deformation [187], magnetic fields [201], ultrasonic vibrations [196], dislocation boundary spacings [202], grain boundary energy [203], stored energy [202], and second-phase particles [204] influence the processes of recrystallisation and grain growth. In contrast to CA models, PF models conceptualise grain boundaries as diffuse regions with finite thickness, enabling more accurate reconstruction without predefined shapes. However, PF models necessitate a finer grid to capture grain boundaries at the shortest length scales, resulting in increased computational costs [205]. In recent years, enhanced algorithms, such as the grain remapping algorithm for a reduced set of order parameters [190] and the Sharp Phase Field Method (SPFM) for a new inherently discrete formulation [206], alongside parallel computing [185], have been integrated into PF models to mitigate computational memory and time requirements. Additionally, PF methods face challenges in determining mobility coefficients and phenomenological parameters, including phase composition and solute diffusion [140].

In PF models, both conserved (c) and non-conserved (η) variables are employed to reconstruct solidification evolution, where $\eta = 0$ represents the bulk liquid, $\eta = 1$ denotes the bulk solid, and $0 < \eta < 1$ defines the interfacial region, while c describes the composition of liquid and solid phases [170]. The total energy density f could encompass a combination of bulk free energy density and interfacial free energy density [173]. Following the integration of thermal [207], nucleation [207], Computational Fluid Dynamics (CFD) [208], and crystal plasticity [198] models, the resulting output data reflect microstructural evolution, characterised by changes in dendrite growth (Fig 30), non-dendritic microstructure [209, 210], and solidified grains (e.g., the columnar-to-equiaxed grain transition Fig 31 and layer grains Fig 32), as well as the macroscopic properties, including stress and strain response [183], stress and strain distribution [198], dislocation density distribution [183], and cracking [199]. Numerical methods like CPFEM [198, 207], LBM [211] and Volume-Of-Fluid (VOF) [208] have been integrated into PF models to simulate heat transfer, fluid flow, and micromechanical behaviour. PF models have been applied to reconstruct solidification process in traditional [210] and additive manufacturing. Examples of AM

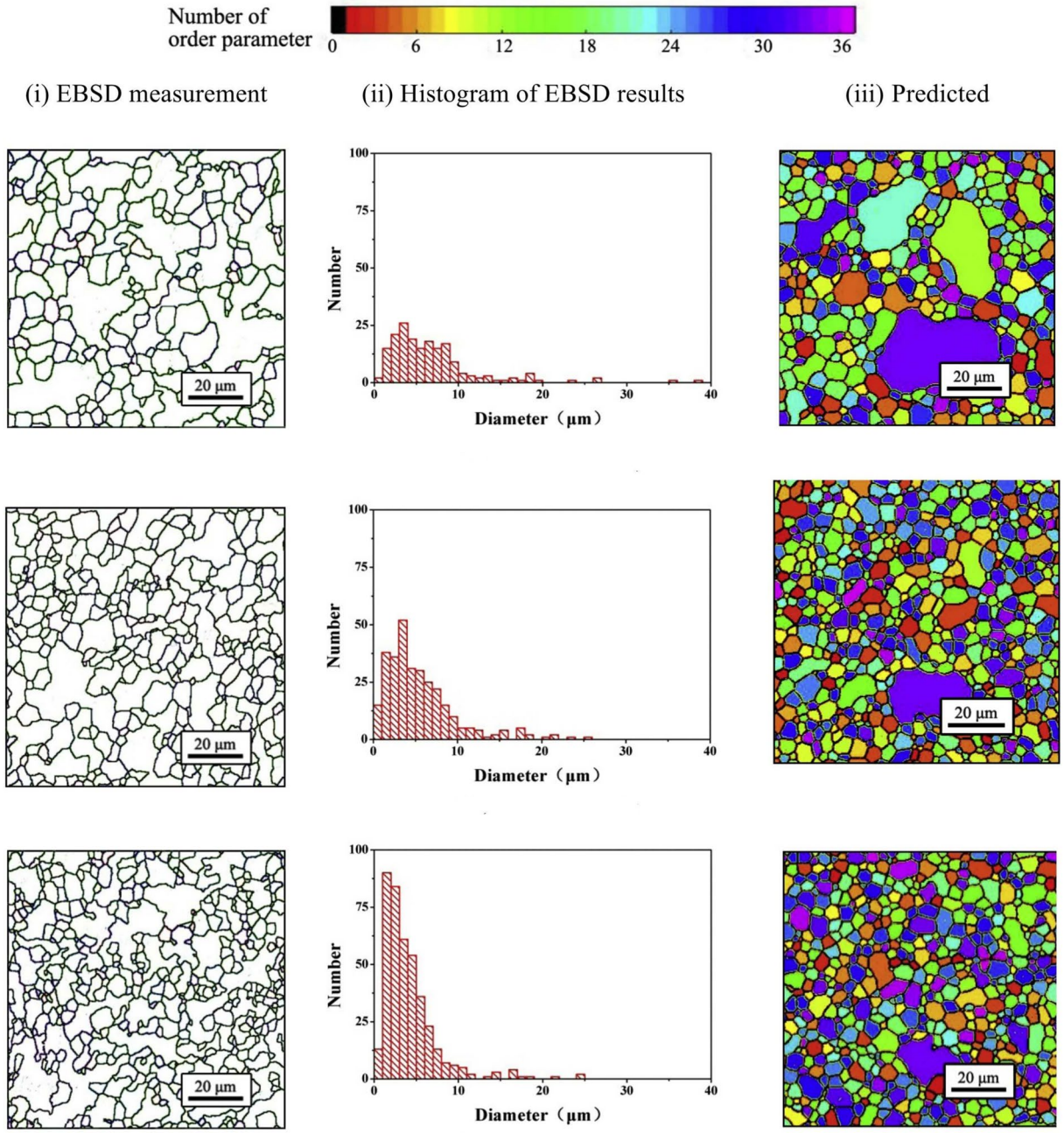

Fig. 28 Predicted grain size evolution using PF models (iii); Grain Size Evolution from Experimental Observations (i); Statistical results of grain size (ii). Reprinted from [196], Copyright (2020), with permission from Elsevier

processes are DED [208], Laser Powder Bed Fusion (LPBF) [198], and SLM [212].

There has also been significant interest in understanding how interfacial kinetic anisotropy [216], interface width [217], supergravity [218], convective conditions [219], build direction [207], melt convection [220], spatial length scales [221], second-phase particles [222] and solute segregation [221] influence the process of solidification. Additionally, advanced techniques have been developed for quantitative, accurate, and efficient reconstructions, such as the Dendritic Needle Network (DNN) scheme [223] for predicting solidification microstructures quantitatively, and the Recursive Grain Remapping (RGR) scheme [224] which optimises computational resources while improving the characterisation of columnar and irregularly shaped grains. PF models for solidification reconstructions offer advantages similar to those for recrystallisation and grain growth reconstructions, particularly in accurately characterising the solid-liquid

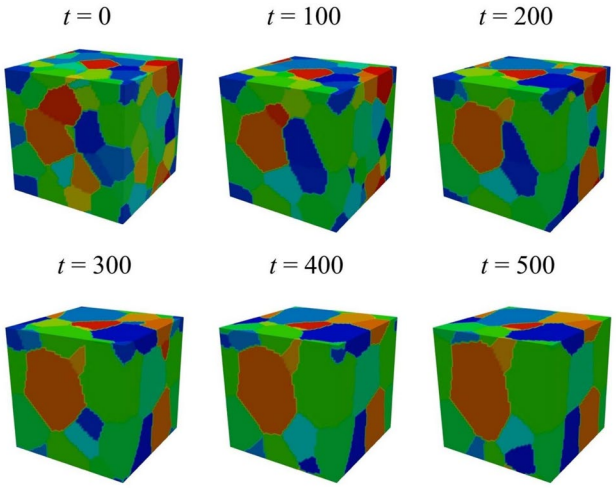

Fig. 29 Snapshots of grain coarsening using PF models at different evolutionary times. Adapted from [197], Copyright (2021), with permission from Elsevier

interface; however, they also present challenges, including higher computational costs and difficulties in determining mobility coefficients and phenomenological parameters. Like CA models, PF models utilize various techniques to characterise the crystallographic structure of grains, facilitating the reconstruction of grain competition during solidification [113]. Furthermore, PF models provide high physical fidelity and can capture subgrain features, such as higher-order dendrites and micro-segregation [113].

PF models reconstruct the evolution of solid-state phase transformations using non-conserved variables η_k, where η_k takes values between 0 and 1. A value of $\eta_k = 1$ corresponds to the k^{th} phase variant, while $\eta_k = 0$ represents all other phase variants [175]. The total energy density f could encompass a combination of bulk chemical-free energy density, gradient energy density, thermal energy density, and elastic energy density [177]. Following the integration of thermal [225], thermo-mechanical [226], nucleation [175], and crystal plasticity [178] models, the resulting output data reflect microstructural evolution, characterised by changes in rearrangement of thermodynamic phases involving nucleation, growth, and impingement (Fig 33)), as well as the macroscopic properties, including the stress and strain response [178, 226], stress and strain distribution [178], and fracture toughening [177]. Recent years have seen significant interest in how electric field [225], grain-boundary diffusion [227], and shape memory [226] influence the process of solid-state phase transformation. Furthermore, advanced techniques for enhancing the reconstruction of solid-state phase transformations have been integrated into PF models. Notable examples include the Landau-Ginzburg-Devonshire method [225] incorporating phase coexistence, the strain-induced transformation

Table 4 A summary of PF models for physical reconstructions in polycrystalline materials

Evolutional processes	Properties and performance	Advantages	Disadvantages
Recrystallisation and grain growth	Thermal conductivity [176]; flow stress and strain [190]; stress and strain response [174]; stress and strain distribution [189].	Better characterisation of interface and curvature between grains.	Higher computing cost; determination of mobility coefficients and phenomenological parameters.
Solidification	Stress and strain response [183]; stress and strain distribution [198]; dislocation density distribution [183]; cracking [199].	Better characterisation of the solid-liquid interface; better characterisation of higher-order dendrites branches; crystallographic characterisations.	Higher computing cost; determination of mobility coefficients; phenomenological parameters.
Solid-state phase transformation.	Stress and strain response [200]; stress and strain distribution [200]; fracture toughening [177].	Better characterisation of interface and curvature between thermodynamic phases.	Higher computing cost; determination of mobility coefficients and phenomenological parameters.

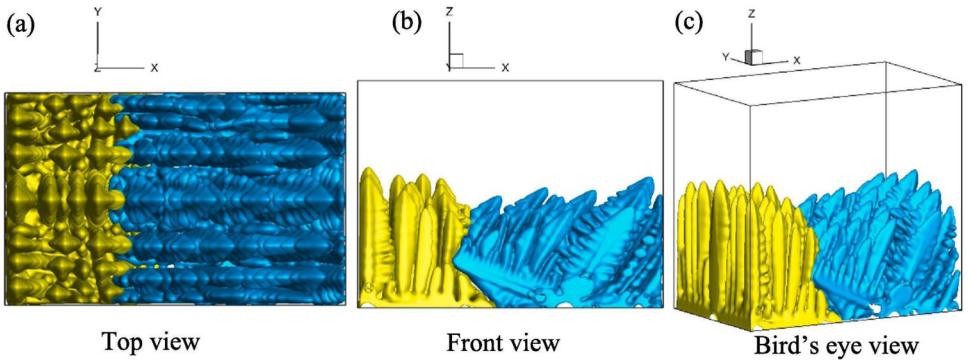

Fig. 30 Dendrite growth using PF models, (**a**) top view, (**b**) front view, and (**c**) bird's eye view. Adapted from [213], Copyright (2021), with permission from Elsevier

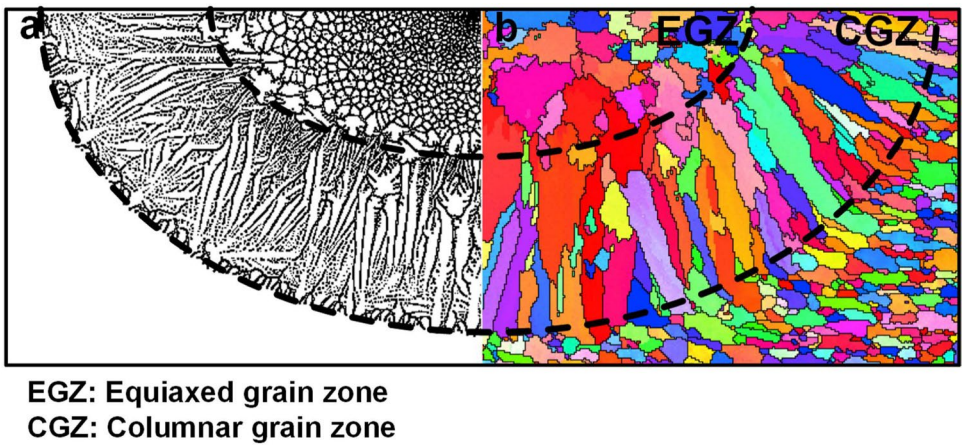

Fig. 31 Comparison of the columnar-to-equiaxed grain transition between (**a**) PF reconstruction and (**b**) experimental results. Adapted from [214], Copyright (2021), with permission from Elsevier

[228] aimed at optimising microstructural characteristics, the coupled diffusional/displacive mechanism for accurately replicating critical microstructural features [229], the scale-free mechanism for multivariant phase transformations [230], and the reactive diffusion mechanism for the transformation of three phases [231]. Like solidification, recrystallisation, and grain growth reconstruction processes, PF models that reconstruct solid-state phase transformation evolution offer improved characterisations of interfaces and curvature between thermodynamic phases. However, these models face challenges, including increased computational costs and the complexities of determining mobility coefficients and phenomenological parameters [133].

3.4 Level Set Methods

In Level Set (LS) models, the zero level set of smooth functions defines grain boundaries and curvatures, while microstructure evolution is dictated by the solutions of these functions [134]. The key steps are summarized below.

- State generation: The principle of reconstructing polycrystalline materials with LS models involves assigning each grain an independent level set function, $\phi_i(\boldsymbol{x}, t)$. The grain boundaries $\Gamma(t)$, are defined by the zero level set of these functions, expressed as

$$\phi_i(\boldsymbol{x}, t) = \pm\, d(\boldsymbol{x}, \Gamma), \quad \Gamma = \partial G_i = \{\boldsymbol{x} \in \Omega, \phi_i(\boldsymbol{x}, t) = 0\}$$
$$\boldsymbol{x} \in \Omega, \quad i = 1, 2, ..., N \tag{8}$$

  where $\boldsymbol{x}$ is any point in the analytical domain Ω, $d(\boldsymbol{x}, \Gamma)$ is the Euclidean distance between any point $\boldsymbol{x}$ and boundary interfaces $\Gamma(t)$, and N is the number of active level-set functions used to reconstruct different grains. The level set function $\phi_i(\boldsymbol{x}, t)$ is greater than zero inside grain G_i and less than zero outside grain G_i [232, 233].
- Governing equations: A velocity field $\boldsymbol{v}$ characterises the evolution of the interface $\Gamma(t)$, with its movement governed by the Hamilton-Jacobi equation [232]:

$$\frac{\partial \phi_i}{\partial t} + \boldsymbol{v} \nabla \phi_i = 0, \quad i = 1, 2, ..., N \tag{9}$$

  The velocity field $\boldsymbol{v}$ can be approximated by [232]:

$$\boldsymbol{v} = \mu P \boldsymbol{n} = -\mu \gamma \kappa \boldsymbol{n} \tag{10}$$

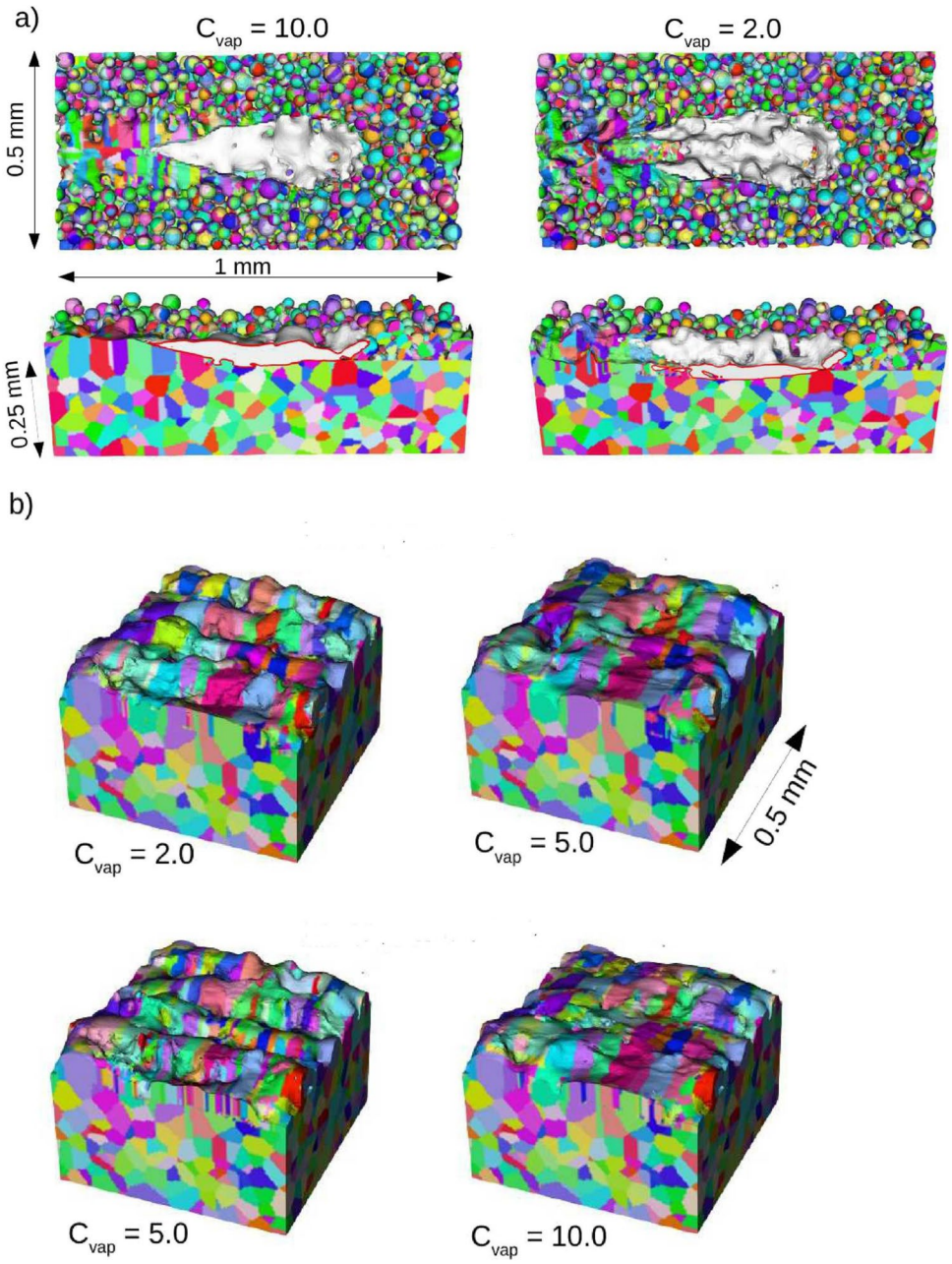

Fig. 32 **a** Power layer grains using PF models at different evaporation coefficients C_{vap}; **b** Solidified layer grains using PF models at different C_{vap}. Reprinted from [215], Copyright (2021), with permission from Elsevier

where μ represents the interface mobility, $\boldsymbol{n}$ denotes the outward vector normal to the interface, $P = -\gamma\kappa$ means the driving pressure, κ indicates the local mean curvature, and γ is the grain boundary energy. The reinitialisation procedure [234] often implicitly defines the interface $\Gamma(t)$ by treating the level set function in Equation 9 as a signed distance function. Enhanced definition of velocity fields have been proposed by considering stored energy [235], specific properties of thermodynamic phase interfaces [233], anisotropic grain boundary energy and mobility [232].

- Discretisation and numerical solution: Both grid [236, 237] and vertex-edge-face-volume [234] discretisation methods have been employed in LS models to specify the analytical domain. Recent advancements in vertex-edge-face-volume discretisation techniques, including mesh adaptation [238] and topological re-meshing [239] (Fig 34), have been achieved to reduce mesh density requirements, improve characterisations at interfaces, and decrease computational costs. Numerical methods including FDM [236] and FEM [233] are employed to solve Equation 9, implemented via grid and vertex-edge-face-volume discretisation techniques. Recently, the mesh-free interface finite element method has been developed as an alternative to grid and vertex-edge-face-volume schemes for solving level set equations [240].

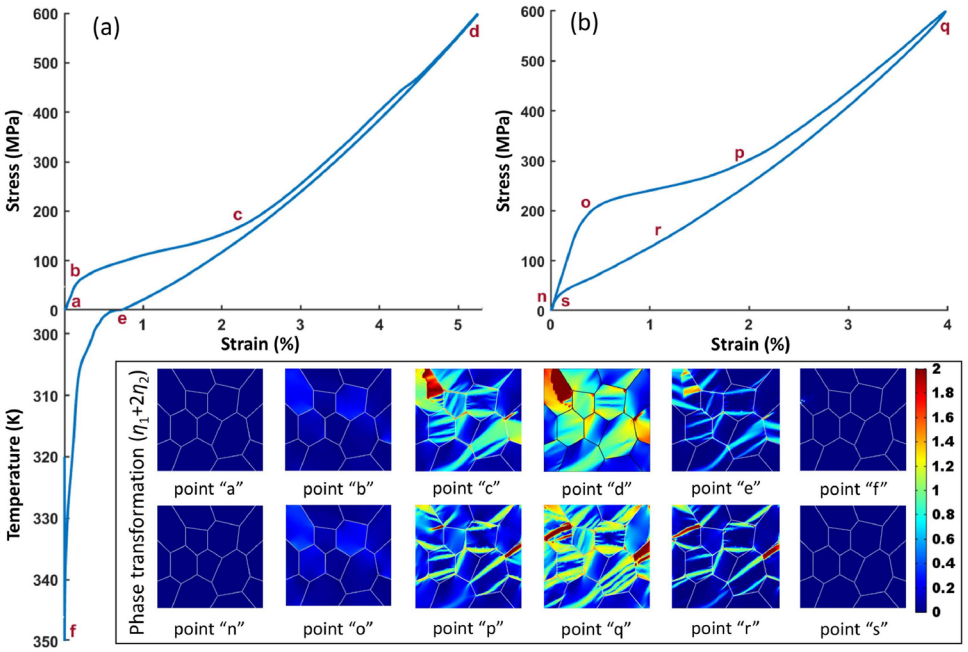

Fig. 33 Phase transformation reconstruction of shape memory alloy using PF models, where red means martensite, green means martensite, and blue means austenite. Adapted from [226], Copyright (2021), with permission from Elsevier

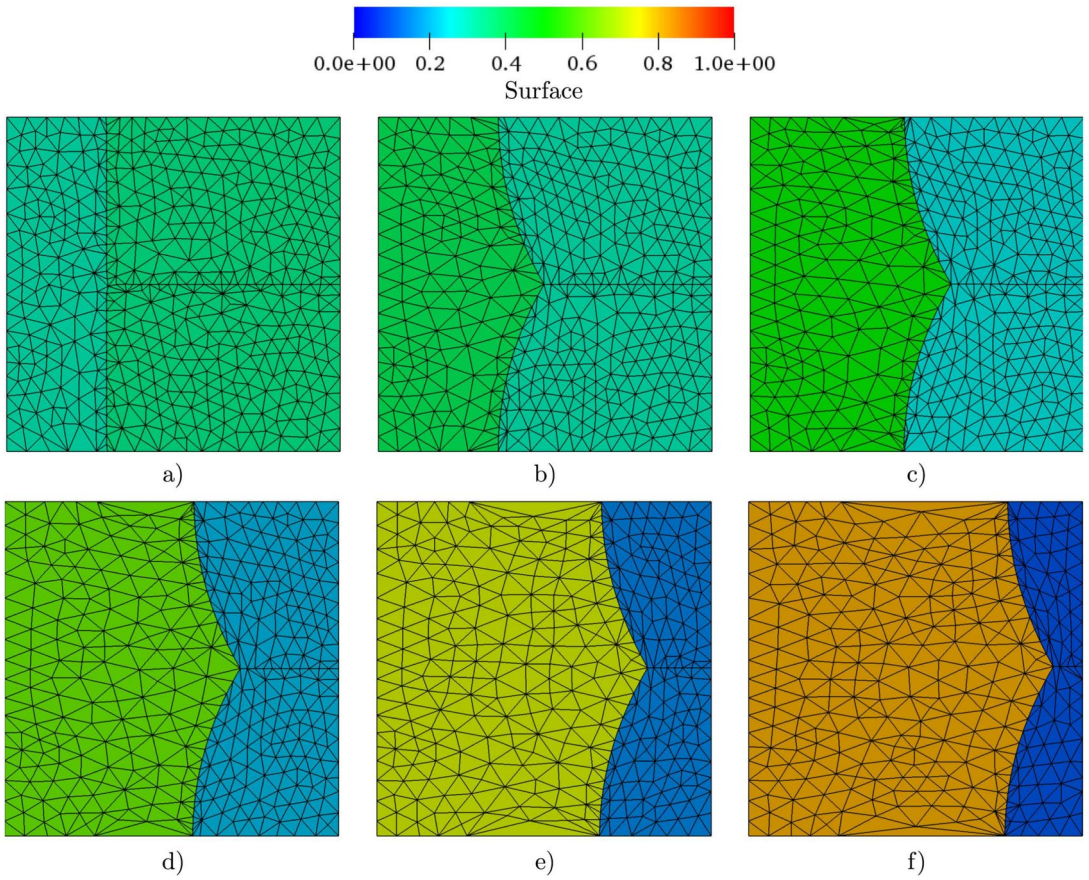

Fig. 34 Example of T-junction interface evolution using the LS-TRM method with three level set functions: **a** initial state, **b** state at $t = 0.1$, **c** state at $t = 0.2$, **d** state at $t = 0.3$, **e** state at $t = 0.4$, **f** state at $t = 0.5$. Reprinted from [239], Copyright (2020), with permission from Elsevier

Since their introduction, LS models have become a prominent approach for modelling multiphase propagating interface issues [184]. These methods have been employed to reconstruct evolutionary processes, including solidification, solid-state phase transformation, recrystallisation, and grain growth in polycrystalline materials. LS models for recrystallisation and grain growth reconstructions take dislocation density, grain size, and grain boundary as input data [241]. Following the integration of nucleation [242], dislocation density [242], growth [232], and crystal plasticity [243] models, the resulting output data reflect microstructural evolution, characterised by changes in grain sizes and shapes (such as grain refinement and coarsening) (Fig 35)), as well as the macroscopic properties, including stress and strain response [243], stress and strain distribution [243]. LS models effectively implement both SRX and DRX reconstructions. For further details, readers are referred to [235] for SRX and [242] for DRX.

LS models have also been successfully used for solidification [240] and solid-state phase transformation [244] reconstructions. LS models share advantages and disadvantages with PF models, particularly concerning their capacity for interface boundary characterisations and associated computational costs [111]. Furthermore, LS models are restricted to uniform deformation conditions, and the analysis of sharp grain boundary interfaces necessitates considerable computational effort, resulting in diminished efficiency [111, 245]. Additionally, a notable limitation of LS models is their inability to capture the evolution of crystallographic texture [245].

3.5 Others

Other physics-based models have also been employed to reconstruct evolutionary processes in polycrystalline materials, including vertex/front tracking for grain growth [246] and machine learning for solidification [113]. A detailed

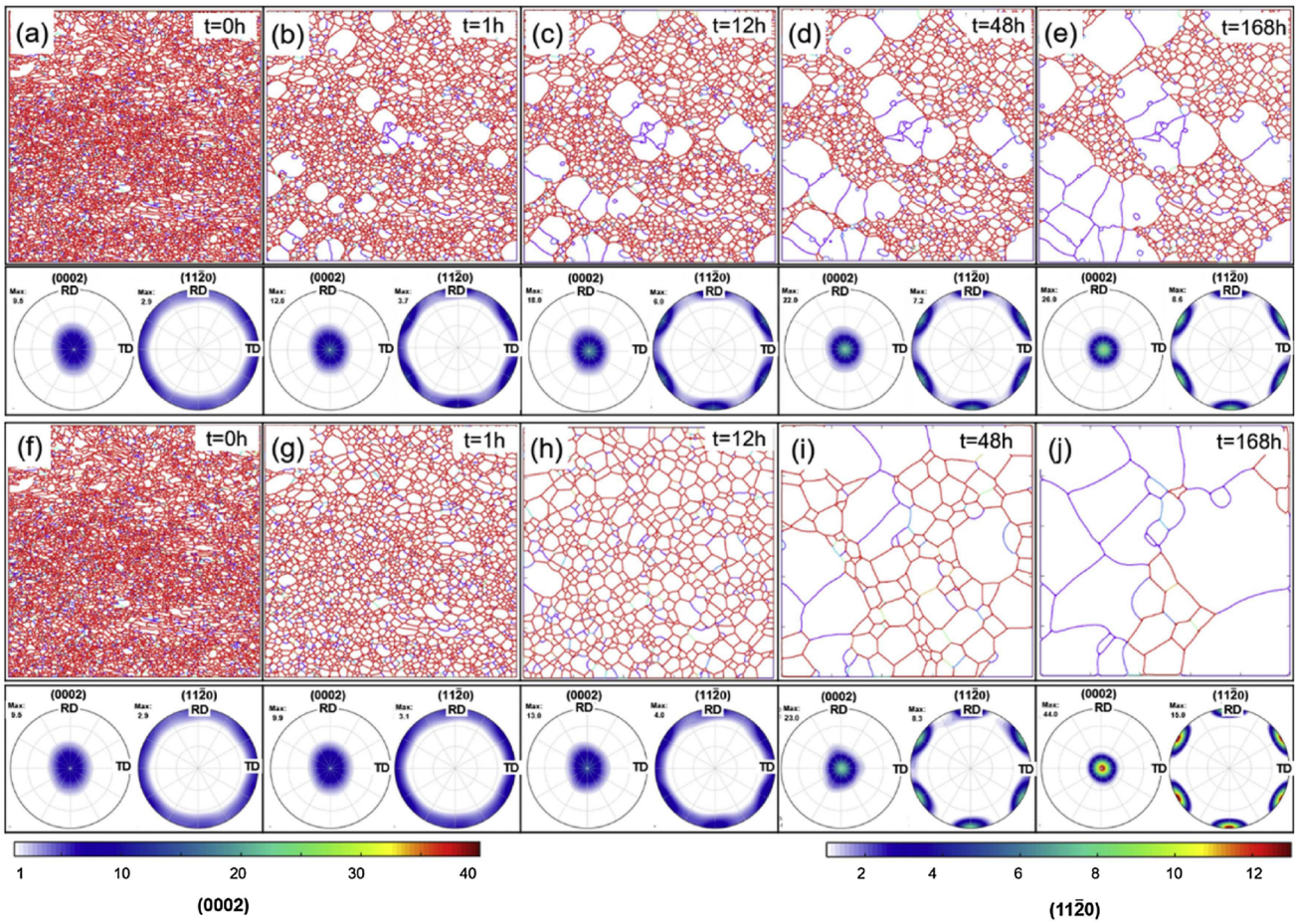

Fig. 35 Reconstructed grain coarsening microstructures using LS models and corresponding textures at different time steps: **a**, **f** initial experimental microstructure; **b**-**e** abnormal grain coarsening at an annealing temperature of 220 °C; **g**-**j** uniform grain coarsening at an annealing temperature of 350 °C. The colour of the grain boundaries indicates their relative mobility. Reprinted from [241], Copyright (2020), with permission from Elsevier

step-by-step description of each method falls outside the scope of this review. Readers are referred to the references for further information on each method's concepts, strengths, and weaknesses.

4 Geometry-Based Models

Geometry-based models disregard the evolutionary processes of microstructural formation, focusing directly the morphological and crystallographic information in polycrystalline materials. These models can be broadly categorised into shape-based reconstructions, texture synthesis, and others, which are discussed in the following subsections.

4.1 Shape-Based Reconstruction

In shape-based reconstruction, simplified geometries such as cubes [247], rhombic dodecahedrons [248], truncated octahedrons [249], Voronoi polyhedra [250], and ellipsoids [251] are utilized to characterise grain morphology, among which Voronoi tessellation and ellipsoid packing are most popular. Therefore, for ease of explanation, we further divide shape-based reconstruction into three groups: (a) simple geometries (e.g. cubes, rhombic dodecahedrons, and truncated octahedrons), (b) Voronoi tessellation, and (c) ellipsoid packing.

4.1.1 Simple Geometries

As one of the oldest approaches for polycrystalline reconstruction, researchers have long utilized simplified grain shapes to bridge the relationship between microscopic structures and macroscopic properties. Regular grain microstructures (Fig 36) facilitate numerical modelling and offer a novel mechanism to investigate the grain shape effects on grain interaction [252], crystallographic texture evolution [253], intergranular stress corrosion cracking [249] and aggregate response [254]. For example, in [255], grains were represented by homogenised squares to reconstruct crystallographic texture evolution with FEM. In [247], brick elements were utilized to represent a single averaged grain for investigating the relationship between micro and macro variables in crystal plasticity deformation. Another regular grain morphology utilized by [249] involved modelling a single grain as a rhombic dodecahedron to examine the impact of crystal shape on inter-granular interactions. Truncated octahedron-based grains were proposed by [249] to investigate stress corrosion cracking between grains. [254] represented grains using cubic, rhombic dodecahedral, and truncated octahedral morphologies simultaneously to investigate the effect of grain shape on the mechanical response of grain aggregates.

4.1.2 Voronoi Tessellation

Voronoi tessellation (VT) models partition the analysis domain into Voronoi polyhedra, which are formed as random seeds grow and merge [256]. The workflow is summarized below.

- Seeds generation: A 3D space $\boldsymbol{D} \in \boldsymbol{R}^3$ is defined and N seed points $\{S_i \in \boldsymbol{D} | i = 1, 2, ..., N\}$ are allocated within it. The coordinates of each seed may be generated randomly or determined by a Poisson point process.
- Voronoi tesselation: Each seed is linked to a Voronoi polyhedron $\boldsymbol{VP}(S_i)$, with its spatial area characterised in Equation 11.

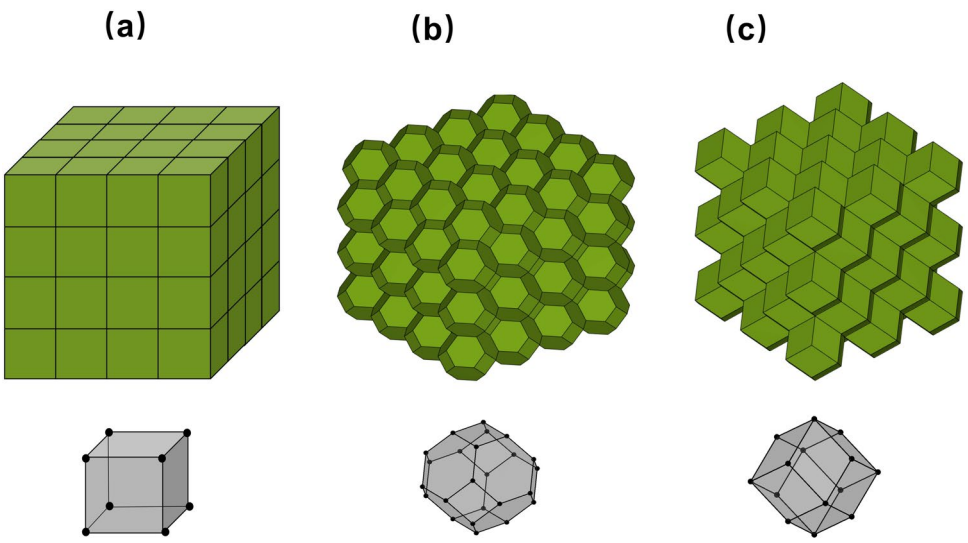

Fig. 36 Reconstructed polycrystalline microstructures with simple geometries: **a** cubes; **b** truncated octahedrons; **c** rhombic dodecahedrons;

$$\boldsymbol{VP}(S_i) = \{P(x,y,z) \in \boldsymbol{D} | d(P,S_i) < d(P,S_j), \quad \forall i \neq j \; i,j = 1,2,...,N\} \tag{11}$$

where $d(P, S)$ is the Euclidean distance between the set point P and the seed point S.

- Space discretisation: The space area of each Voronoi polyhedron $\boldsymbol{VP}(S_i)$ is specified by discretising the whole domain.
- Orientation assignment: Crystallographic orientations are asigned to each Voronoi polyhedron $\boldsymbol{VP}(S_i)$.

To enhance calculation efficiency, the hierarchical queue algorithm [257] is employed to implement the Euclidean distance function. The boundary recognition of Voronoi polyhedrons primarily relies on the distance to the corresponding seed. Alternatively, the relief immersion algorithm [258], derived from watershed segmentation, has also been utilized for boundary identification. Crystallographic orientation assignment can be based on a uniform distribution or a map extracted from a reference image [259]. Both grid [260] and vertex-edge-face-volume [260] discretisation techniques have been employed in VT models (Fig 37). In grid discretisation, [261] generated 3D random Voronoi polyhedrons with a common constrained surface by first creating grains beneath this surface through erosion or expansion of neighbouring voxels, followed by the immediate application of Voronoi tessellation to fill the remaining space. In the vertex-edge-face-volume discretisation, [262] developed a grain edge splitting procedure to produce 3D periodic high-quality elements. To address the over-discretisation issue resulting from the unavoidable formation of small Voronoi polyhedrons, [263] proposed a novel algorithm for geometry regulation, multi-meshing, and re-meshing of large-scale random 3D polycrystals (Fig 38).

To obtain a more realistic grain size distribution, a controlled Poisson-Voronoi tessellation model incorporating a single control parameter has been developed to accurately capture grain morphologies [264]. In [265], molecular dynamics and discrete element methods were combined to pack particles with controlled grain size distributions. Genetic algorithms were employed in [266] to modify the Poisson-Voronoi tessellation for a more precise characterisation of grain size distribution, and [267] introduced a constrained Voronoi model to create an approximate reconstruction of 3D polycrystalline microstructure, facilitating the interpretation of surface microstructural measurements. The power diagram (also known as the Laguerre diagram [268]) helps set the size of each Laguerre polyhedron $\boldsymbol{LP}(S_i)$ by adding a non-negative weight w_i:

$$\begin{aligned} \boldsymbol{LP}(S_i) &= \{P(x,y,z) \in \boldsymbol{D} | d_L(P,S_i) < d_L(P,S_j), \quad \forall i \neq j \; i,j = 1,2,...,N\} \\ d_L(P,S_\bullet) &= d_E(P,S_\bullet)^2 - w_\bullet \end{aligned} \tag{12}$$

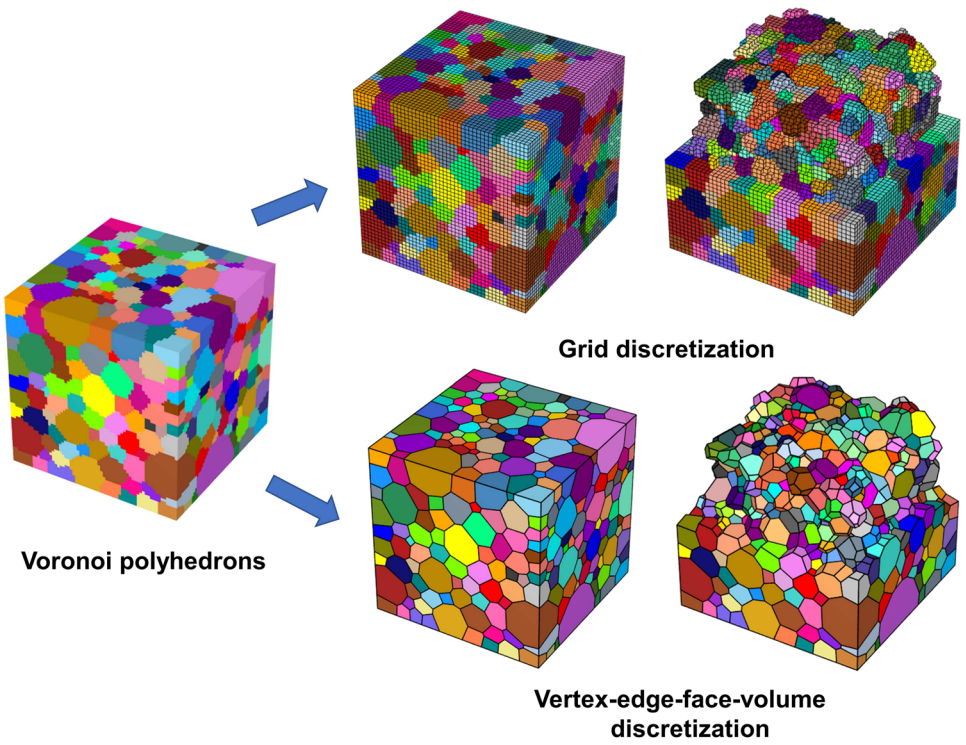

Fig. 37 Schematic visualisations of the grid and vertex-edge-face-volume discretisation for Voronoi polyhedrons

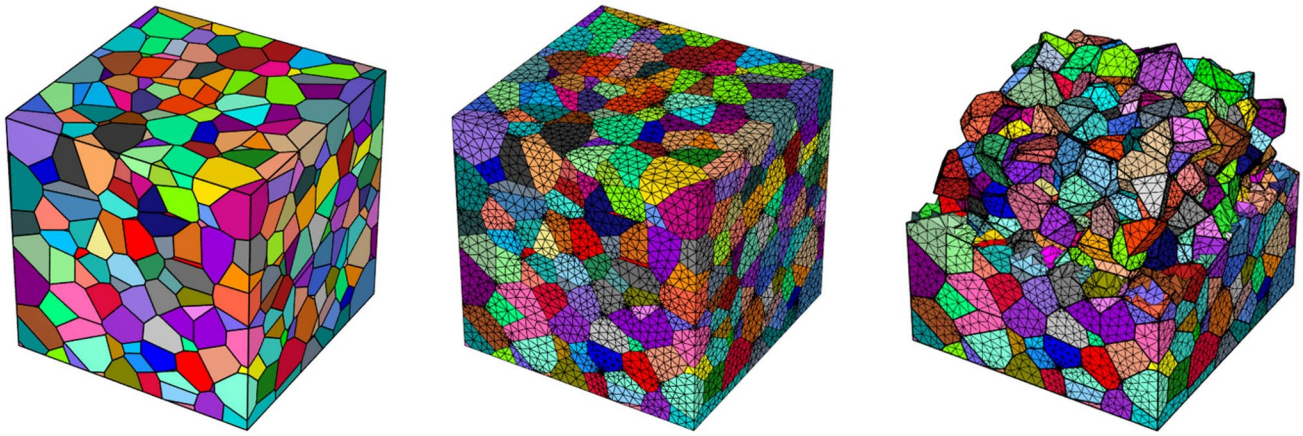

Fig. 38 Schematic visualisations of the multi-meshing and re-meshing of 3D large-scale Voronoi polyhedrons

where d_L is the power distance and d_E is the Euclidean distance. In recent years, the Laguerre-Voronoi (LV) model has gained popularity as an alternative to the Poisson-Voronoi (PV) model [16]. Research has demonstrated that LV models yield more accurate reconstructions of polycrystalline structures than PV models. Several open-source packages for VT models are available, including Neper [263] (Fig 38), Voro++ [269], Qhull [270], and MicroStructPy [271].

4.2 Ellipsoid Packing

Microstructural features generated by VT models may significantly diverge from experimental observations. To create polycrystalline microstructures that align morphological and crystallographic characteristics with reality, more accurate geometric units and enhanced statistical algorithms are required. Significant progress was reported in [251], where ellipsoids were used to reconstruct 3D aluminium polycrystal microstructures from experimental data of two orthogonal sections under the hypothesis that 2D orthogonal data

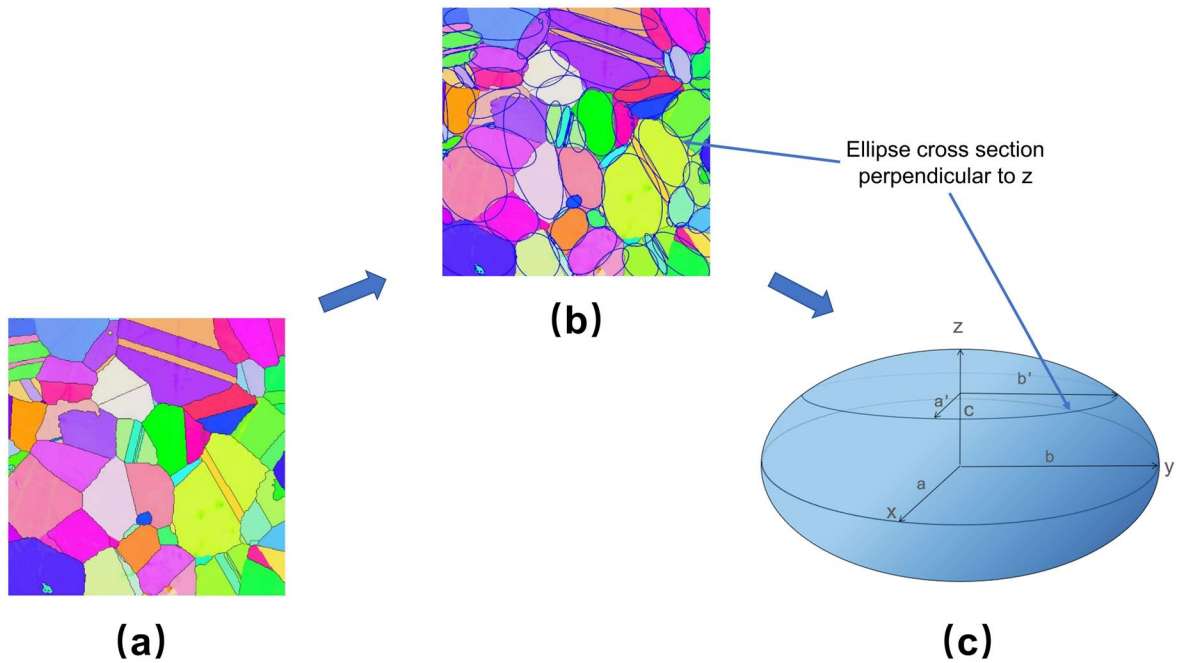

Fig. 39 Ellipsoid generation: **a** EBSD scan, **b** ellipse fitting, **c** projection ellipsoid

sufficiently characterise a 3D microstructure. The workflow is summarized below.

- Ellipsoid generation: Ellipsoids are generated following 2D experimental observations, as illustrated in Fig 39. Fig 39a shows the 2D EBSD scan perpendicular to the sample's normal direction, while Fig 39b demonstrates how grains are fitted with ellipses [272]. Subsequently, the distributions of the ellipse semiaxes $f(a')$, and $f(b')$ can be obtained. Similarly, when the 2D EBSD scan is oriented perpendicular to the sample's rolling direction, the distributions of the ellipse semiaxes $f(b')$, and $f(c')$ can also be accessed. Here $\{a', b', c'\}$ represent the semiaxes of ellipses. The next step involves an approximate calculation of the distribution of ellipsoid semiaxes:

$$< a' >= a\pi/4, a \approx 4a'/\pi; < b' >= b\pi/4, b \approx 4b'/\pi; \\ < c' >= c\pi/4, c \approx 4c'/\pi \tag{13}$$

  where $\{a, b, c\}$ are the semiaxes of the ellipsoid (Fig 39c). Next, the joint probability distribution $f(a, b)$ or $f(c, b)$ and the conditional probability distribution $f(c|b)$ or $f(a|b)$ can be quantified. Finally, the true 3D ellipsoid distribution can be estimated by Equation 14 [251].

$$f(a, b, c) = f(a, b) \cdot f(c|b) = f(c, b) \cdot f(a|b) \tag{14}$$

- Ellipsoid packing: Ellipsoids are packed into a defined space by sampling a set of overlapping ellipsoids from the distribution $f(a, b, c)$ and randomly placing them within that space.
- Space discretisation: The spatial area of each ellipsoid is defined without overlaps by discretising the entire domain. Initially, the grid discretisation technique partitions the entire domain into cubic lattices. Subsequently, the cellular automaton algorithm fills the space, with new ellipsoids nucleating at lattice centres and growing until they either contact other ellipsoids or reach the domain boundaries.
- Orientation assignment: Random crystallographic orientations are asigned to each newly generated ellipsoid [273]. Subsequently, the simulated annealing algorithm can be employed to identify an optimal configuration of orientations and misorientations that align with experimental observations [274]. Figure 40 presents some examples generated by the ellipsoid packing algorithm.

During the space discretisation step, grain boundaries formed by the cellular automaton process are often unrealistic and deviate from actual observations. To address this issue, the Monte Carlo grain growth method [275] has been implemented to relax the final grid-based structure, enabling grain boundaries to better align with experimental observations. The orthogonal EBSD scans-based method has been extended by [276] to reconstruct high purity aluminum with elongated grains (Fig 41). Instead of discretising the space by grids, vertex-edge-face-volume discretisation techniques were employed to characterise grain boundaries through Voronoi tessellation. Subsequently, Voronoi cells were aggregated and scaled by an affine stretch to match

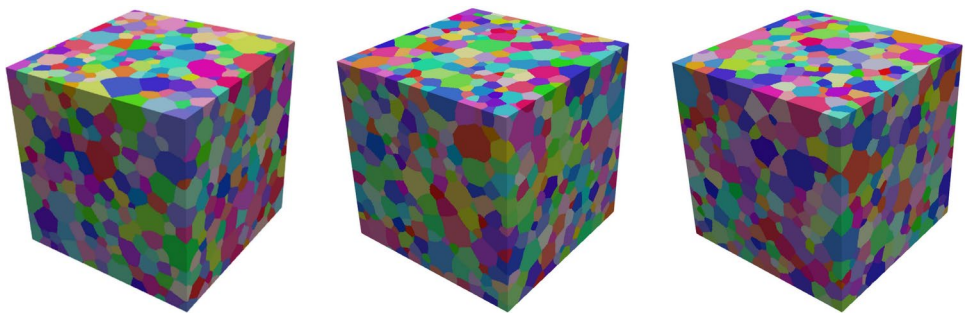

Fig. 40 Reconstructed polycrystalline microstructures through ellipsoid packing

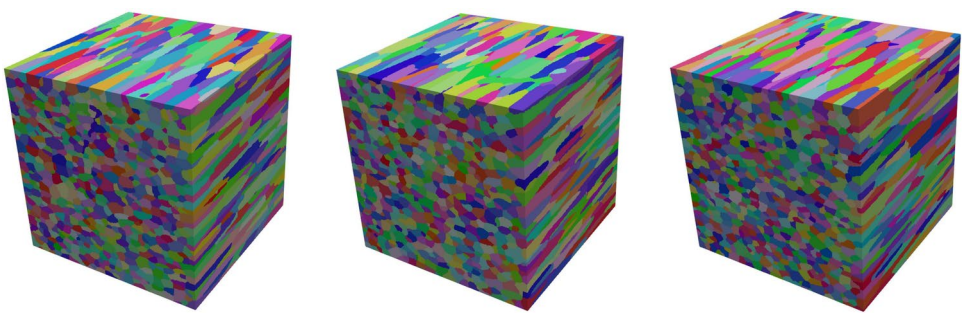

Fig. 41 Reconstructed polycrystalline microstructures with elongated grains

observed grain aspect ratios. Additionally, [277] proposed another 2D scan-based method to reconstruct 3D anisotropic polycrystalline microstructures with constrained surface ellipsoids. The aforementioned 2D EBSD section methods do not accurately depict how grains connect in 3D space. Furthermore, other morphological descriptors, such as grain neighbour relationships and shape orientation distributions, cannot be derived from these methods. To overcome these biases and limitations, [278] directly reconstructed the polycrystalline structure from 3D experimental data (Fig 42). The DREAME.3D software [57] encompasses most of the ellipsoid packing methods mentioned above.

Recent research on ellipsoid packing models has focused on optimised algorithms to enhance efficiency, synthesising polycrystalline microstructures with multiple phases, achieving precise characterisations, generating annealing twins and precipitates, and reconstructing polycrystalline microstructures in additive manufacturing. For instance, [279] employed ellipsoidal growth tessellations to streamline ellipsoid generation and packing processes. An advancing layer algorithm was developed in [280] for dense ellipse packing. Additionally, [281] introduced a random sequential addition algorithm based on grid discretisation techniques for efficient ellipsoid generation and packing. In multiphase microstructures, the initial-phase grain structure is created following the procedure outlined in [251]. Subsequent phases are nucleated randomly on the first-phase grain boundaries and grown until their volume fractions reach targeted values [282]. Furthermore, [283] incorporated second-phase particles into synthetic polycrystalline microstructures based on the pair-correlation function, while [284] reconstructed a dual-phase titanium structure using the transformation phase insertion algorithm. A general framework for generating, validating, and quantifying 3D anisotropic two-phase polycrystalline materials was proposed in [285]. Truncated grain size distributions was applied in [286] to eliminate unnaturally large grains. Additionally, the two-point correlation function [283] has been utilized to statistically characterise grain morphology, orientation, and spatial distribution for highly heterogeneous characterisations. For annealing twin reconstruction, [286] developed a twin insertion algorithm on the assumption that twin grains do not inhabit the boundary of the parent grain and completely separate them. [287] reconstructed twins based on parent grain size distribution, conditional probability distributions of twin distance and thickness, and joint probability of the number of twins. In precipitate reconstruction, [288] incorporated dispersed precipitates into reconstructed polycrystalline microstructures, considering factors such as shape, size, volume, orientation, two-point correlation, distance to surface, and random vector channel-width distributions. A genetic algorithm-based numerical approach was presented in [289] for optimising the selection of precipitate characterisations. In the context of polycrystalline microstructures in additive manufacturing, [290] proposed a universal material template for the standardised reconstruction of commonly utilized polycrystalline materials. Meanwhile, [291] introduced a novel framework for reconstructing polycrystalline microstructures in additive manufacturing, facilitating grain growth regeneration and specification of growth properties, which enhances the simulation of polycrystalline materials with spatial variations.

Compared to VT models, Ellipsoid Packing (EP) models generate polycrystalline microstructures that align more closely with experimental observations, making them a preferred method for exploring Structure-Properties-Performance (SPP) linkages in polycrystalline materials. For instance, [1] examined the influence of grain size and crystallographic polarity on stress hardening and anisotropic plasticity. In [292], EP models were integrated with uncertainty-quantified parametrically homogenised constitutive algorithms to establish a connection between mechanical property responses and microstructural characterisations. In [293], EP models were combined with ML to predict cyclic stress-strain responses.

Additionally, EP models have been utilized for microstructure-sensitive studies to optimise performance. For instance, [294] analysed and designed microstructural characterisations to quantify the probability of fatigue crack occurrence; [284] developed a database between microstructure and elasto-viscoplastic deformation in dual-phase titanium alloys; and [295] employed ML and data-consistent inversion to establish an inverse relationship between average grain size and average yield strength. In recent years,

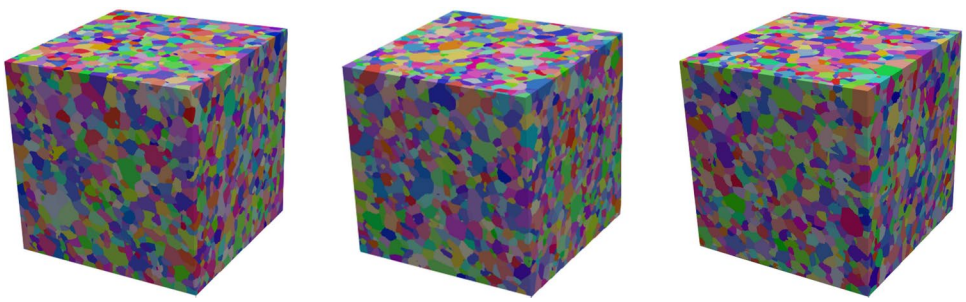

Fig. 42 Reconstructed polycrystalline microstructures from 3D experimental observations

EP models have been widely utilized in ML-based surrogate models to predict the properties of polycrystalline materials. The microstructure data reconstructed through EP models can be used directly as input for these surrogate models. Subsequently, DL networks, including convolutional neural networks [296], graph neural networks [297], and deep neural networks [298], can create the low-dimensional embeddings (physical features) of polycrystalline microstructures, which are then associated with target properties.

4.3 Texture Synthesis

Texture synthesis (TS) has been a popular research area in computer vision, addressing applications such as occlusion filling, image and video compression, and foreground removal. Pioneering work by [299] redefined the texture synthesis problem within an exemplar-based framework, treating the original image, $\boldsymbol{X}$, as a stationary Markov Random Field (MRF) characterised by specific properties:

- Locality: $f(X_i|all\ particles\ except\ i) = f(X_i|neighbours\ of\ particle\ i)\ i = 1, 2, ..., N$, where N is the number of particles that correspond to pixels or voxels in $\boldsymbol{X}$, X_i represents the local state in polycrystalline materials, like orientation colormap, phases, etc., $f(X_i|all\ particles\ except\ i)$ and $f(X_i|neighbours\ of\ particle\ i)$ are the conditional probability density of X_i.
- Stationarity: $f(X_i|neighbours\ of\ particle\ i)$ does not depend on the location of X_i.

TS models have been effectively utilized to reconstruct polycrystalline materials [300]. Figure 43 presents some examples generated by TS models. The workflow is summarized below.

- State generation: The synthesised domain, $\boldsymbol{Y}$, is first discretised into grids, referred to as pixels or voxels. The subsequent step involves defining $\boldsymbol{Y}$ as a Markov Random Field (MRF), where pixels or voxels representing different local states are connected to their neighbours. A pixel (voxel)'s neighbourhood is defined by enclosing it within a specified area and linking it to other pixels (voxels) within that region. The initial state can be established by randomly assigning states to each grid in $\boldsymbol{Y}$ [300] or by starting from a small seed image randomly selected from the original image, $\boldsymbol{X}$ [302].
- State update: After state generation, conditional probability density sampling from the original image $\boldsymbol{X}$ updates the local state of the selected pixel (or voxel) in the synthesized domain $\boldsymbol{Y}$ based on the known states of its neighbouring pixels (voxels). The update path could be implemented by a random order [300], a raster-scan order [303] or a layer-by-layer form [302]. In each update step, the conditional probability density $f(X_i|N^X)$ in $\boldsymbol{X}$ is assumed to be equal to the conditional probability density $f(Y_i|N^Y)$ in $\boldsymbol{Y}$. Here, N^X and N^Y denote the neighbourhood of particle i in the $\boldsymbol{X}$ and $\boldsymbol{Y}$, respectively. The best matching of N_B^X is determined by solving the following minimisation problem:

$$N_B^X = arg\ \min_{N_j^X} \sum_j \omega_j \left\| N_j^Y - N_j^X \right\|^2 \tag{15}$$

where j denotes the particles in N^X and N^Y, and ω is the Gaussian weighting function [300].

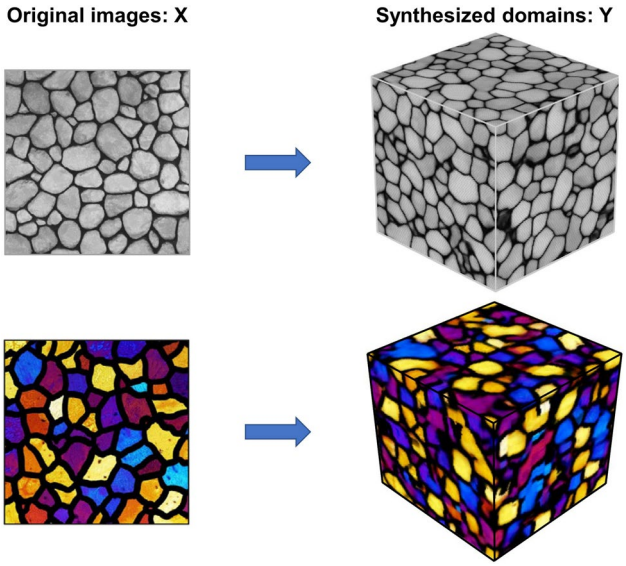

Fig. 43 Reconstructed 3D polycrystalline microstructures from experimental 2D polycrystalline microstructures through texture synthesis [301]

Polycrystalline microstructures generated by shape-based models are largely idealised, failing to account for the complexities of real-world grain shapes [304]. TS models, particularly patch-based schemes, offer a compelling alternative due to their capacity to capture intricate features such as grain boundaries [305]. Furthermore, TS models can reconstruct larger microstructure regions (centimetre scale) essential for engineering analysis by utilising small-scale experimental data (micron scale) [302]. However, reconstruction quality in TS models is unstable, influenced by specific parameters such as neighbourhood size, overlap size, and number of replicates; hence, sensitivity analysis is necessary to optimise these parameters for optimal quality [301]. Additionally, reconstruction paths can significantly affect results, potentially leading to the loss of spatial correlations [20]. Currently, direct colourmaps linking orientation and colour space are the predominant techniques for

orientation colouring [301]. However, inherent discontinuities and ambiguities in characterising crystallographic features have hindered their broader application in constructing SPP linkages.

4.4 Other Geometry-Based Models

Other geometry-based models, including high-order characterisation, reduced-order strategies, and machine learning, have been employed to capture morphological and crystallographic features. Figure 44 illustrates examples generated by these models. A brief overview of each approach is provided in this subsection, including their strengths and weaknesses.

High-order characterisation models employ optimisation methods such as simulated annealing [283] (Fig 44b) and phase recovery [12] to minimise system energy functions until the target threshold is achieved. These models effectively generate statistically equivalent representative volume elements with high-order characterisation distributions. However, local material states are limited to a discrete set of material phases. Further refinement may be necessary when examining more complex local states of polycrystalline materials, such as crystal lattice orientation.

Reduced-order strategies such as Principal Component Analysis (PCA) [309] (Fig 44c), nonlinear dimensionality reduction (Fig 44d), and multiscale approaches [310] have been applied to geometric reconstruction of polycrystalline materials. These methods enhance computational efficiency and represent complex material states more effectively than high-order characterisation models. Future research should prioritise reduced-order reconstructions for realistic microstructures over idealised stochastic characteristics.

Machine learning-based methods, including Convolutional Deep Belief Networks (CDBN) [311], Variational Autoencoders (VAE) [312], and deep transfer learning [308] (Fig 44e), have recently been employed for geometric reconstructions of polycrystalline materials. While these models effectively capture morphological information, they face challenges in accurately characterising crystallographic features due to discontinuity and ambiguity issues in orientation colouring.

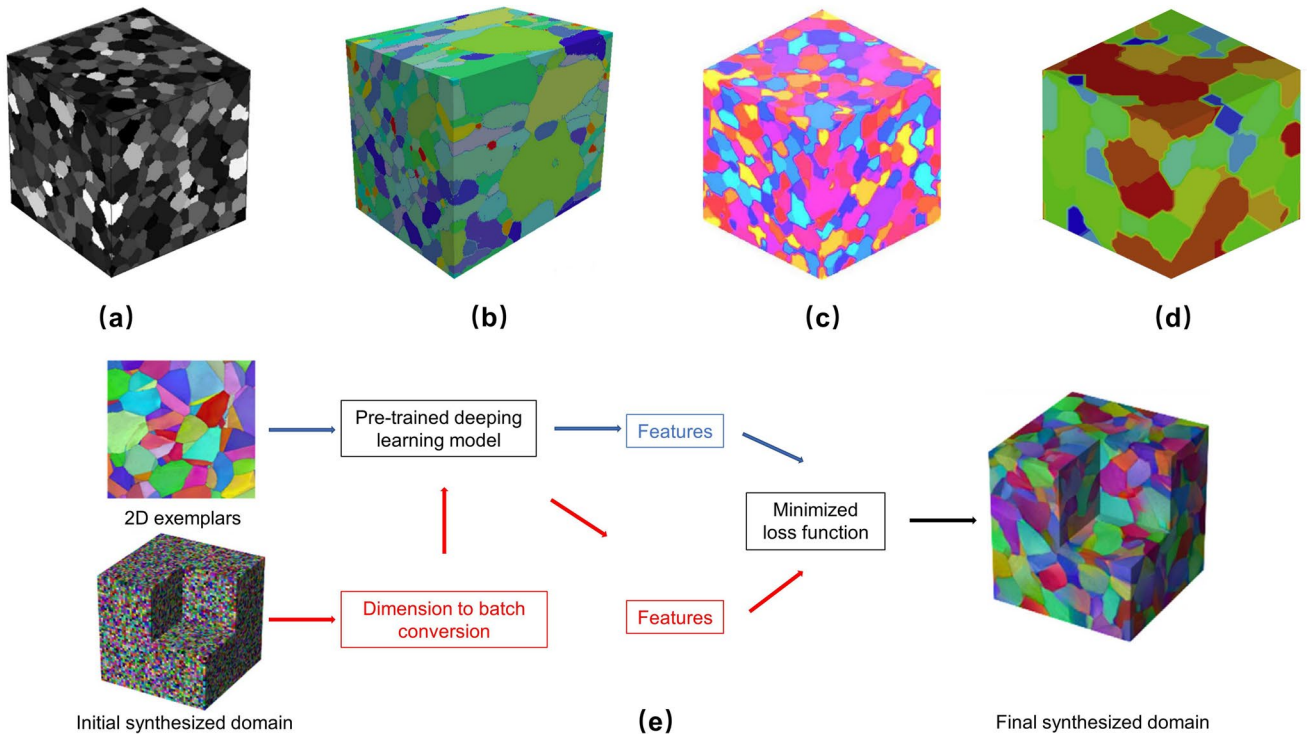

Fig. 44 Rreconstructed 3D polycrystalline microstructures through phase recovery (**a**) [12]; simulated annealing (**b**) [283]; principal component analysis (c) [306]; nonlinear dimensionality reduction (**d**) [307]; transfer learning (**e**) [308]

5 Conclusions, Challenges, and Perspectives

5.1 Conclusions

In polycrystalline materials' morphological characterisations (e.g., precipitates, grains, cracks, porosities, minerals, and thermodynamic phases). OM, SEM, and computed tomography (CT) are imaging technologies employed to acquire morphological data. PFIB/SEM, FIB/SEM, BIB/SEM, TB/SEM, RM/SEM, and Manual Collection System (MCS)/SEM deliver adequate resolutions towards 1 *nm*. MCS/OM, S-μCT, μCT, and Nano-CT are suitable for resolutions at micron and submicron scales. Figure 45 illustrates the volume and resolution of various imaging systems for crystallographic characterisations in polycrystalline materials. OIM techniques, including SPED, OMiTEM, EBSD, and X-ray diffraction, are employed to acquire crystallographic data. OMiTEM and SPED achieve sufficient nano-level precision, imaging grains with reconstruction sizes between 0.001 and 1 μm^3. PFIB and FIB are effective for imaging submicron grains, with reconstruction sizes ranging from 100 to 1E5 μm^3. BIB/EBSD, TB/EBSD, HEDM, SR-DCT, Lab-DCT, RM/EBSD, and MCS/EBSD can image microstructure grains with sizes from 1E6 to 1E10 μm^3. Additionally, TT and S3DXRD can capture subgrains sized between 1E4 and 1E7 μm^3. Only TEM-based OIM techniques, such as OMiTEM and SPED, provide adequate nanoscale precision for crystallographic data collection, while destructive systems like

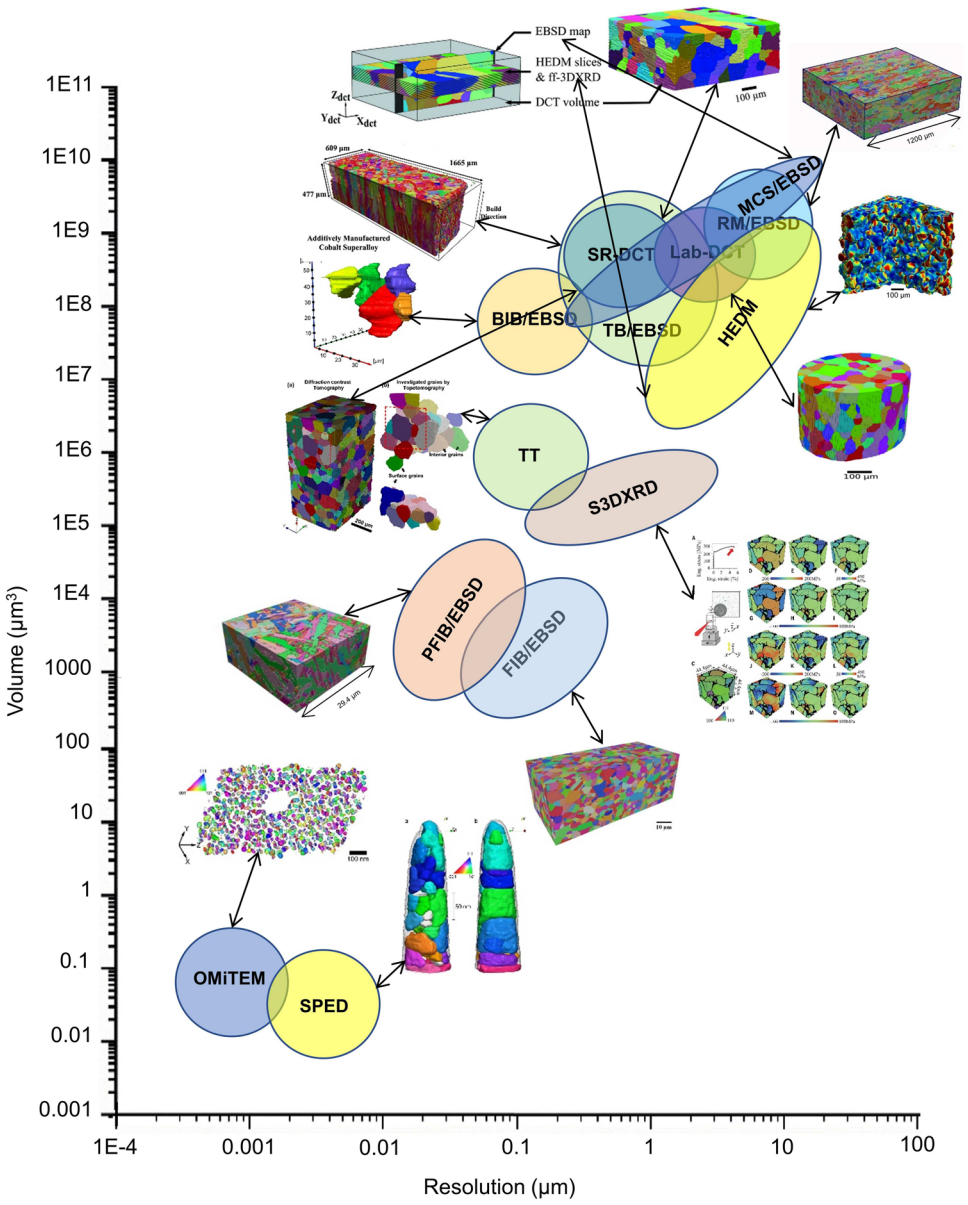

Fig. 45 Volume collected and resolution for various crystallographic data collection systems in polycrystalline materials: SPED ([27]), OMiTEM ([26]), FIB ([9]), PFIB ([31]), TT ([89]), S3XRD ([86]), BIB ([35]), TB ([33]), SR-DCT ([89, 98]), Lab-DCT ([99]), RM [30]), HEDM ([88, 98]), and MCS ([98]) (All figures have been granted copyright)

PFIB and FIB are suited for imaging morphological and crystallographic data at the submicron scale.

In physics-based models, CA, MC, PF, LS, and vertex/front tracking models have been applied to reconstruct recrystallisation and grain growth processes. All, except vertex/front tracking, have been used to construct PSPP linkages. While PF, LS, and vertex/front tracking models can better characterise grain boundaries and curvatures than MC and CA models, they are less commonly used for recrystallisation and grain growth reconstructions due to greater complexity and higher computational cost [111]. The popularity of MC and CA models lies in their ease of implementation and high computational efficiency, especially with parallelisation. Additionally, CA models offer flexible transformation rules, allowing calibration across time and length scales, capturing recrystallisation dynamics and topological characteristics, and realistically characterising grain boundary migration [245]. Owing to their superior real-time, real-space scalability, efficiency, and flexibility, CA models are the most widely used methods for reconstructing recrystallisation and grain growth, particularly in DRX reconstructions [128]. In reconstructions of solidification evolution, CA, MC, PF, and MC models have been employed to reconstruct dendrite growth and solidified grain structures. Only CA and PF models have been utilized to construct PSPP linkages, as other models do not capture crystallographic texture evolution. While MC models show potential for reconstructing the microstructure of AM materials, their accuracy is limited by the need to calibrate length and time scales [61]. LS models have become prominent for modelling multiphase propagating interface problems; however, they are less efficient than PF models due to the initialisation of implicit functions and the computation of extended interfacial velocity fields [184]. PF and CA models are the most widely used methods for reconstructing dendrite growth during solidification evolution [136]. Although CA models offer lower computational cost than PF models, they inadequately reconstruct intricate dendritic details [61]. In contrast, PF models offer superior physical fidelity and can accurately depict subgrain features, such as high-order dendrites and micro-segregation [113]. Similar to solidification reconstructions, PF and CA models are the predominant approaches for reconstructing solid-state phase transformations and are exclusively employed in constructing PSPP linkages. However, due to the aliased interface reconstruction between thermodynamic phases, CA models exhibit lower accuracy in reconstructing solid-state diffusional phase transformations compared to PF models [133].

In geometry-based models, only EP models have been utilized to construct SPP linkages, as they effectively generate stochastic polycrystalline microstructures that closely align with experimental observations. Other methods fail to accurately capture the stochastic microstructure characteristics of polycrystalline materials. Morphological features such as grain size and shape, produced by simple geometries and VT, may significantly deviate from experimental observations. TS, machine learning, and high-order characterisation models need to be revised for accurate reconstructions of crystallographic features, while reduced-order strategies are overly idealised to reconstruct realistic stochastic characteristics.

In general, experimental models deliver high-fidelity, physically accurate data but tend to be resource-intensive, requiring significant time and financial investment. Physical models provide flexibility in capturing the effects of processing parameters such as temperature, diffusion coefficients, and strain rates on microstructural evolution. However, the underlying assumptions-such as those concerning thermal nucleation, solute diffusion, and growth-are often idealised, limiting their capacity to accurately replicate realistic microstructures. Geometrical models, on the other hand, offer computational speed and scalability, enabling rapid, large-scale generation of microstructure reconstructions, yet they generally fail to capture the complex, heterogeneous nature of real-world grains. In summary, experimental models offer the highest accuracy but at the expense of efficiency, geometrical models prioritise efficiency over accuracy, and physical models strike a balance between both.

5.2 Challenges

In experimental reconstruction, the main challenges lie on enhancing data collection systems and advancing data processing techniques [33]. For instance, hybrid and multibeam milling can be applied in serial sectioning to produce high-quality and thin sections, while non-destructive reconstructions can employ modified X-ray sources such as synchrotron CT with Kirkpatrick-Baez mirrors to attain nanometre-scale resolution [24]. Various imaging techniques, including SEM and EBSD for serial sectioning, X-ray microtomography and X-ray diffraction for non-destructive reconstruction, can be integrated to provide comprehensive crystallographic and morphological data. Correlative measurements across multiple length scales can be developed to address downscaling requirements and enhance upscaling outcomes. Researchers can establish quantitative multimodel dataset registration and fusion methodologies to integrate data from both destructive and non-destructive reconstructions [33]. In advanced data processing, serial sectioning should emphasise optimal indexing segmentation of fine intragranular features, such as overlapping phase patterns, and 3D reconstruction of parent grains [38]. For non-destructive reconstruction, new algorithms are expected to address partially overlapped peak diffraction and generalise models to accommodate 3D peaks in deformed grains [96].

In physics-based models, challenges remain in refining methods to enhance fidelity and efficiency. Nucleation [111, 133], anisotropic grain growth [113, 133], rapid solidification [113], and impingement processes [133] are difficult to address quantitatively and predictively with current theoretical hypotheses. Consequently, identifying detailed input parameters [112, 133], proposing improved algorithms [112, 133], and developing advanced models [112] are essential for overcoming these challenges and achieving accurate, efficient, robust, and quantitative reconstructions of microstructure evolution. Another crucial advancement involves integrating geometry-based models with multi-field simulations, including temperature fields (e.g., thermal models), flow fields (e.g., diffusion and CFD models), and stress fields (e.g., mechanical, thermo-mechanical, and crystal plasticity models), which is vital for multiscale simulations linking microscale changes to macroscale properties and performance [111]. Moreover, digital reconstructions produced by physics-based models lack experimental validation. Experimental reconstruction offers precise insights into grain coarsening and refinement, dendrite and solidified grain structures, thermodynamic phase morphologies, grain boundary migration, and higher-order dendrite merging. Observations from experiments should validate reconstruction results from physics-based models.

In geometry-based models, polycrystalline microstructures generated by EP models do not adequately capture the complexities of real-world grain shapes. TS and ML models present attractive alternatives for EP models due to their capability to characterise intricate features such as grain boundaries [308]. However, in practice, TS and ML models have certain limitations in constructing SPP linkages. For instance, orientation colour maps used in TS and ML models are often coloured directly by Euler angles $(\varphi_1, \phi, \varphi_2)$ or Rodrigues-Frank vectors (ρ_1, ρ_2, ρ_3) [301, 308]. The resultant topological discrepancy between unconnected orientation and connected colour spaces can lead to colour discontinuities. Furthermore, neglecting crystal symmetry may introduce colour ambiguity, where identical orientations can be represented by different colours [313, 314]. Lastly, reconstructions produced by TS and ML models are implicit and do not explicitly quantify microstructural features [20]. Thus, challenges faced by TS and ML models include addressing discontinuity and ambiguity issues to align with measured crystallographic characteristics accurately. Simultaneously, new algorithms should be developed to quantify microstructural reconstructions of polycrystalline materials explicitly.

A key performance indicator of experimental approaches is the measurement resolution, which directly relates to the capacity of data collection, i.e. the resulting dataset size. For the synthetic approaches, which include both physics-based and geometry-based models, their efficiency will improve with the growth of computational resources, but their accuracy (or fidelity) may not equally benefit from the increased computing power. Moreover, different methods have different features, strengths, and weaknesses that are often beyond the efficiency and accuracy aspects, which are not directly linked to dataset size or computing power.

5.3 Perspectives

Vast databases generated through digital reconstructions can be characterised by key morphological and crystallographic descriptors (e.g., grain size, grain orientation), which are correlated with materials processing parameters (e.g., deformation, thermal history) and specific materials properties and performance (e.g., stress and strain responses, stress and strain fields, ductile failure, brittle fracture, fatigue failure) [315]. These databases facilitate the construction of forward and inverse PSPP linkages in data-driven modelling to optimise manufacturing processes (cause-effect design) or develop new polycrystalline materials (goals-driven design) [20, 316].

Acknowledgements The authors would like to thank the supports from Chinese Scholarship Council, Swansea University, and the Royal Society (IF\R2\23200112, IEC\NSFC\191628).

Author Contributions B. Chen: carried out the literature study and drafted the article D. Li: provided initial guidance for the research direction and key references P. Davies: reviewed the draft manuscript and provided detailed comments R. Johnston: reviewed the draft manuscript and provided detailed comments X. Ge: helped in data processing and reference analysis C. Li: provided research supervision and secured resources to support the work

Data Availability No datasets were generated or analysed during the current study.

Declarations

Competing Interests The authors declare no competing interests.

References

1. Motaman SA, Haase C (2021) The microstructural effects on the mechanical response of polycrystals: a comparative experimental-numerical study on conventionally and additively manufactured metallic materials. Int J Plast 140:102941. https://doi.org/10.1016/j.ijplas.2021.102941
2. Motaman SAH, Roters F, Haase C (2020) Anisotropic polycrystal plasticity due to microstructural heterogeneity: a multi-scale experimental and numerical study on additively manufactured metallic materials. Acta Mater 185:340–369. https://doi.org/10.1016/j.actamat.2019.12.003
3. Błachnio J, Spychała J, Zasada D (2021) Analysis of structural changes in a gas turbine blade as a result of high temperature and stress. Eng Fail Anal 127:105554. https://doi.org/10.1016/j.engfailanal.2021.105554
4. Han Z, Zhang L, Azzam R, Zhou J, Wang S (2021) A statistical index indicating the degree and mechanical effects of grain size heterogeneity in rocks. Eng Geol 293:106292. https://doi.org/10.1016/j.enggeo.2021.106292
5. Gong Z, Zhao W, Guan K, Rao P, Zeng Q, Liu J, Feng Z (2020) Influence of grain boundary and grain size on the mechanical properties of polycrystalline ceramics: grain-scale simulations. J Am Ceram Soc 103(10):5900–5913. https://doi.org/10.1111/jace.17286
6. Torquato S, Lu B (1993) Chord-length distribution function for two-phase random media. Phys Rev E 47(4):2950. https://doi.org/10.1103/PhysRevE.47.2950
7. Torquato S (2002) Statistical description of microstructures. Annu Rev Mater Res 32(1):77–111. https://doi.org/10.1146/annurev.matsci.32.110101.155324
8. Latypov MI, Kühbach M, Beyerlein IJ, Stinville J-C, Toth LS, Pollock TM, Kalidindi SR (2018) Application of chord length distributions and principal component analysis for quantification and representation of diverse polycrystalline microstructures. Mater Charact 145:671–685. https://doi.org/10.1016/j.matchar.2018.09.020
9. Groeber M, Ghosh S, Uchic MD, Dimiduk DM (2008) A framework for automated analysis and simulation of 3d polycrystalline microstructures.: part 1: statistical characterization. Acta Mater 56(6):1257–1273. https://doi.org/10.1016/j.actamat.2007.11.041
10. Motaman SAH, Kibaroglu D (2024) The anisotropic grain size effect on the mechanical response of polycrystals: the role of columnar grain morphology in additively manufactured metals. J Mater Sci Technol 181:240–256. https://doi.org/10.1016/j.jmst.2023.10.010
11. Torquato S, Stell G (1982) Microstructure of two-phase random media. i. the n-point probability functions. J Chem Phys 77(4):2071–2077. https://doi.org/10.1063/1.444011
12. Fullwood DT, Niezgoda SR, Kalidindi SR (2008) Microstructure reconstructions from 2-point statistics using phase-recovery algorithms. Acta Mater 56(5):942–948. https://doi.org/10.1016/j.actamat.2007.10.044
13. Seibert P, Raßloff A, Kalina KA, Gussone J, Bugelnig K, Diehl M, Kästner M (2023) Two-stage 2d-to-3d reconstruction of realistic microstructures: implementation and numerical validation by effective properties. Comput Methods Appl Mech Eng 412:116098. https://doi.org/10.1016/j.cma.2023.116098
14. Segurado J, Lebensohn RA, LLorca J (2018) Computational homogenization of polycrystals. Adv Appl Mech 51:1–114. https://doi.org/10.1016/bs.aams.2018.07.001
15. Bargmann S, Klusemann B, Markmann J, Schnabel JE, Schneider K, Soyarslan C, Wilmers J (2018) Generation of 3d representative volume elements for heterogeneous materials: a review. Prog Mater Sci 96:322–384. https://doi.org/10.1016/j.pmatsci.2018.02.003
16. Kuhn J, Schneider M, Sonnweber-Ribic P, Böhlke T (2020) Fast methods for computing centroidal laguerre tessellations for prescribed volume fractions with applications to microstructure generation of polycrystalline materials. Comput Methods Appl Mech Eng 369:113175. https://doi.org/10.1016/j.cma.2020.113175
17. Niezgoda SR, Turner DM, Fullwood DT, Kalidindi SR (2010) Optimized structure based representative volume element sets reflecting the ensemble-averaged 2-point statistics. Acta Mater 58(13):4432–4445. https://doi.org/10.1016/j.actamat.2010.04.041
18. Fullwood DT, Niezgoda SR, Adams BL, Kalidindi SR (2010) Microstructure sensitive design for performance optimization. Prog Mater Sci 55(6):477–562. https://doi.org/10.1016/j.pmatsci.2009.08.002
19. Matouš K, Geers MG, Kouznetsova VG, Gillman A (2017) A review of predictive nonlinear theories for multiscale modeling of heterogeneous materials. J Comput Phys 330:192–220. https://doi.org/10.1016/j.jcp.2016.10.070
20. Bostanabad R, Zhang Y, Li X, Kearney T, Brinson LC, Apley DW, Liu WK, Chen W (2018) Computational microstructure characterization and reconstruction: review of the state-of-the-art techniques. Prog Mater Sci 95:1–41. https://doi.org/10.1016/j.pmatsci.2018.01.005
21. Robertson IM, Schuh CA, Vetrano JS, Browning ND, Field DP, Jensen DJ, Miller MK, Baker I, Dunand DC, Dunin-Borkowski R et al (2011) Towards an integrated materials characterization toolbox. J Mater Res 26(11):1341–1383. https://doi.org/10.1557/jmr.2011.41
22. Ullah A, Liu G, Luan J, Li W, Rahman M, Ali M (2014) Three-dimensional visualization and quantitative characterization of grains in polycrystalline iron. Mater Charact 91:65–75. https://doi.org/10.1016/j.matchar.2014.02.009
23. Hatakeyama T, Sawada K, Hara T, Sekido K, Kimura K (2021) Three-dimensional analysis of the precipitation behavior of 18cr-9ni-3cu-nb-n steel at 973 k. Scr Mater 200:113904. https://doi.org/10.1016/j.scriptamat.2021.113904
24. Wang Y, Miller J (2020) Current developments and applications of micro-ct for the 3d analysis of multiphase mineral systems in geometallurgy. Earth Sci Rev 211:103406. https://doi.org/10.1016/j.earscirev.2020.103406
25. Poulsen HF (2020) Multi scale hard x-ray microscopy. Curr Opin Solid State Mater Sci 24(2):100820. https://doi.org/10.1016/j.cossms.2020.100820
26. Zhu W, Wu G, Godfrey A, Schmidt S, He Q, Feng Z, Huang T, Zhang L, Huang X (2022) Five-parameter grain boundary character distribution of gold nanoparticles based on three dimensional orientation mapping in the tem. Scr Mater 214:114677. https://doi.org/10.1016/j.scriptamat.2022.114677
27. Harrison P, Zhou X, Das SM, Lhuissier P, Liebscher CH, Herbig M, Ludwig W, Rauch EF (2022) Reconstructing dual-phase nanometer scale grains within a pearlitic steel tip in 3d through 4d-scanning precession electron diffraction tomography and automated crystal orientation mapping. Ultramicroscopy 238:113536. https://doi.org/10.1016/j.ultramic.2022.113536
28. Schwartz AJ, Kumar M, Adams BL, Field, DP Electron Backscatter Diffraction in Materials Science vol. 2. Springer, New York. https://doi.org/10.1007/978-0-387-88136-2
29. Garner A, Donoghue J, Geurts R, Al Aboura Y, Winiarski B, Prangnell PB, Burnett TL (2022) Large-scale serial sectioning of environmentally assisted cracks in 7xxx al alloys using femtosecond laser-pfib. Mater Charact 188:111890. https://doi.org/10.1016/j.matchar.2022.111890
30. Rowenhorst DJ, Nguyen L, Murphy-Leonard AD, Fonda RW (2020) Characterization of microstructure in additively

manufactured 316l using automated serial sectioning. Curr Opin Solid State Mater Sci 24(3):100819. https://doi.org/10.1016/j.cossms.2020.100819
31. DeMott R, Collins P, Kong C, Liao X, Ringer S, Primig S (2020) 3d electron backscatter diffraction study of α lath morphology in additively manufactured ti-6al-4v. Ultramicroscopy 218:113073. https://doi.org/10.1016/j.ultramic.2020.113073
32. Kammer D, Voorhees P (2008) Analysis of complex microstructures: serial sectioning and phase-field simulations. MRS Bull 33(6):603–610. https://doi.org/10.1557/mrs2008.125
33. Echlin MP, Burnett TL, Polonsky AT, Pollock TM, Withers PJ (2020) Serial sectioning in the sem for three dimensional materials science. Curr Opin Solid State Mater Sci 24(2):100817. https://doi.org/10.1016/j.cossms.2020.100817
34. Alkemper J, Voorhees P (2001) Quantitative serial sectioning analysis. J Microsc 201(3):388–394. https://doi.org/10.1046/j.1365-2818.2001.00832.x
35. Winiarski B, Gholinia A, Mingard K, Gee M, Thompson G, Withers P (2017) Broad ion beam serial section tomography. Ultramicroscopy 172:52–64. https://doi.org/10.1016/j.ultramic.2016.10.014
36. Uchic MD, Holzer L, Inkson BJ, Principe EL, Munroe P (2007) Three-dimensional microstructural characterization using focused ion beam tomography. MRS Bull 32(5):408–416. https://doi.org/10.1557/mrs2007.64
37. Xu W, Ferry M, Cairney J, Humphreys F (2007) Three-dimensional investigation of particle-stimulated nucleation in a nickel alloy. Acta Mater 55(15):5157–5167. https://doi.org/10.1016/j.actamat.2007.05.045
38. DeMott R, Haghdadi N, Kong C, Gandomkar Z, Kenney M, Collins P, Primig S (2021) 3d electron backscatter diffraction characterization of fine α titanium microstructures: collection, reconstruction, and analysis methods. Ultramicroscopy 230:113394. https://doi.org/10.1016/j.ultramic.2021.113394
39. Spowart JE (2006) Automated serial sectioning for 3-d analysis of microstructures. Scr Mater 55(1):5–10. https://doi.org/10.1016/j.scriptamat.2006.01.019
40. Ghosh S, Bhandari Y, Groeber M (2008) Cad-based reconstruction of 3d polycrystalline alloy microstructures from fib generated serial sections. Comput Aided Des 40(3):293–310. https://doi.org/10.1016/j.cad.2007.11.003
41. Lenthe WC, Echlin MP, Stinville JC, De Graef M, Pollock TM (2020) Twin related domain networks in rené 88dt. Mater Charact 165:110365. https://doi.org/10.1016/j.matchar.2020.110365
42. Ullah A, Liu G, Wang H, Khan M, Khan DF, Luan J (2013) Optimal approach of three-dimensional microstructure reconstructions and visualizations. Mater Express 3(2):109–118. https://doi.org/10.1166/mex.2013.1108
43. Wang H, Xue W, Kang R, Zhang Y, Liu G (2019) Topology characteristics of three-dimensional grains in polycrystalline materials. Sci China Technol Sci 62(2):263–268. https://doi.org/10.1007/s11431-017-9303-8
44. Polonsky AT, Lenthe WC, Echlin MP, Livescu V, Gray GT III, Pollock TM (2020) Solidification-driven orientation gradients in additively manufactured stainless steel. Acta Mater 183:249–260. https://doi.org/10.1016/j.actamat.2019.10.047
45. Rottmann PF, Polonsky AT, Francis T, Emigh MG, Krispin M, Rieger G, Echlin MP, Levi CG, Pollock TM (2021) Tribeam tomography and microstructure evolution in additively manufactured alnico magnets. Mater Today 49:23–34. https://doi.org/10.1016/j.mattod.2021.05.003
46. Hielscher R, Nyyssönen T, Niessen F, Gazder AA (2022) The variant graph approach to improved parent grain reconstruction. Materialia 22:101399. https://doi.org/10.48550/arXiv.2201.02103
47. Niessen F, Nyyssönen T, Gazder AA, Hielscher R (2022) Parent grain reconstruction from partially or fully transformed microstructures in MTEX. J Appl Crystallogr 55(1):180–94. https://doi.org/10.48550/arXiv.2104.14603
48. Polonsky AT, Raghavan N, Echlin MP, Kirka MM, Dehoff RR, Pollock TM (2022) Scan strategies in ebm-printed in718 and the physics of bulk 3d microstructure development. Mater Charact 190:112043. https://doi.org/10.1016/j.matchar.2022.112043
49. Salanov AN, Kochurova NM, Serkova AN, Kalinkin AV, Isupova LA, Parmon VN (2019) Oxidation and recrystallization of platinum group metals (pt, pd, rh) in oxygen. surface and subsurface reconstruction of polycrystalline platinum during annealing in the o2 atmosphere over the temperature range of 600–1400 k. Appl Surf Sci 490:188–203. https://doi.org/10.1016/j.apsusc.2019.05.289
50. Saville AI, Vogel SC, Creuziger A, Benzing JT, Pilchak AL, Nandwana P, Klemm-Toole J, Clarke KD, Semiatin SL, Clarke AJ (2021) Texture evolution as a function of scan strategy and build height in electron beam melted ti-6al-4v. Addit Manuf 46:102118. https://doi.org/10.1016/j.addma.2021.102118
51. Sangid MD, Rotella J, Naragani D, Park J-S, Kenesei P, Shade PA (2020) A complete grain-level assessment of the stress-strain evolution and associated deformation response in polycrystalline alloys. Acta Mater 201:36–54. https://doi.org/10.1016/j.actamat.2020.09.051
52. Chu T, Ranson W, Sutton MA (1985) Applications of digital-image-correlation techniques to experimental mechanics. Exp Mech 25(3):232–244. https://doi.org/10.1007/bf02325092
53. Abuzaid WZ, Sangid MD, Carroll JD, Sehitoglu H, Lambros J (2012) Slip transfer and plastic strain accumulation across grain boundaries in hastelloy x. J Mech Phys Solids 60(6):1201–1220. https://doi.org/10.1016/j.jmps.2012.02.001
54. Sutton MA, Li N, Joy D, Reynolds AP, Li X (2007) Scanning electron microscopy for quantitative small and large deformation measurements part i: sem imaging at magnifications from 200 to 10000. Exp Mech 47(6):775–787. https://doi.org/10.1007/s11340-007-9042-z
55. Collins TJ (2007) Imagej for microscopy. Biotechniques 43(S1):25–30. https://doi.org/10.2144/000112517
56. Bachmann F, Hielscher R, Schaeben H (2010) Texture analysis with mtex–free and open source software toolbox. In: Solid State Phenom, vol. 160, pp. 63–68. Trans Tech Publ. https://doi.org/10.4028/www.scientific.net/SSP.160.63
57. Groeber MA, Jackson MA (2014) Dream. 3d: a digital representation environment for the analysis of microstructure in 3d. Integr Mater Manuf Innov 3(1):56–72. https://doi.org/10.1186/2193-9772-3-5
58. Ji H, Cai Z, Pei W, Huang X, Lu Y (2020) Drx behavior and microstructure evolution of 33cr23ni8mn3n: experiment and finite element simulation. J Mater Res Technol 9(3):4340–4355. https://doi.org/10.1016/j.jmrt.2020.02.059
59. Wang J, Chen G, Huang S, Zhang H, Chen Q, Zhang C, Du Z (2022) Multi-scale modeling and simulation for multi-pass processing of ta-2.5 w alloy. Int J Mech Sci 218:107069. https://doi.org/10.1016/j.ijmecsci.2022.107069
60. Zhang C, Du Y, Zhang L, Jin C, Zhou X, Li F (2022) Hot deformation behavior of c276 superalloy in shifted strain rate compression: experiments and cellular automaton modelling. J Alloys Compd 898:162775. https://doi.org/10.1016/j.jallcom.2021.162775
61. Meng G, Gong Y, Zhang J, Zhu L, Xie H, Zhao J (2022) Multi-scale simulation of microstructure evolution during direct laser deposition of inconel718. Int J Heat Mass Transf 191:122798. https://doi.org/10.1016/j.ijheatmasstransfer.2022.122798
62. Zhang J, Meng G, Zhu L, Xu P, Wang S, Xue P, Yang Z (2022) Research on the evolution mechanism of solidified structure

during laser cladding in718 alloy. Appl Therm Eng 215:118925. https://doi.org/10.1016/j.applthermaleng.2022.118925
63. Le J, Boehlert C, Huang G, Mao J, Lei L, Han Y, Lu W (2022) Tib whisker induced variant selection in titanium matrix composites. Scr Mater 217:114772. https://doi.org/10.1016/j.scriptamat.2022.114772
64. Viganò N, Ludwig W (2020) X-ray orientation microscopy using topo-tomography and multi-mode diffraction contrast tomography. Curr Opin Solid State Mater Sci 24(4):100832. https://doi.org/10.1016/j.cossms.2020.100832
65. Miki H, Yoneyama A, Hirano K (2022) Visualizing morphological structures of rice grains in precooked products using synchrotron radiation x-ray phase-contrast computed tomography. Food Funct. https://doi.org/10.1039/d2fo02714c
66. Hong C, Zhang Y, Lindkvist A, Liu W, Tischler J, Xu R, Jensen DJ (2021) Recrystallization boundary migration in the 3d heterogeneous microstructure near a hardness indent. Scr Mater 205:10. https://doi.org/10.1016/j.scriptamat.2021.114187
67. Poulsen HF (2012) An introduction to three-dimensional x-ray diffraction microscopy. J Appl Crystallogr 45(6):1084–1097. https://doi.org/10.1107/S0021889812039143
68. Lindkvist A, Fang H, Juul Jensen D, Zhang Y (2021) Optimizing laboratory x-ray diffraction contrast tomography for grain structure characterization of pure iron. J Appl Crystallogr 54(1):99–110. https://doi.org/10.1107/S1600576720014673
69. King A, Ludwig W, Herbig M, Buffiere J-Y, Khan A, Stevens N, Marrow T (2011) Three-dimensional in situ observations of short fatigue crack growth in magnesium. Acta Mater 59(17):6761–6771. https://doi.org/10.1016/j.actamat.2011.07.034
70. Larson B, Yang W, Ice G, Budai J, Tischler J (2002) Three-dimensional x-ray structural microscopy with submicrometre resolution. Nature 415(6874):887–890. https://doi.org/10.1038/415887a
71. Nygren KE, Pagan DC, Bernier JV, Miller MP (2020) An algorithm for resolving intragranular orientation fields using coupled far-field and near-field high energy x-ray diffraction microscopy. Mater Charac 165:110366. https://doi.org/10.1016/j.matchar.2020.110366
72. Naragani DP, Shade PA, Kenesei P, Sharma H, Sangid MD (2019) X-ray characterization of the micromechanical response ahead of a propagating small fatigue crack in a ni-based superalloy. Acta Mater 179:342–359. https://doi.org/10.1016/j.actamat.2019.08.005
73. King A, Johnson G, Engelberg D, Ludwig W, Marrow J (2008) Observations of intergranular stress corrosion cracking in a grain-mapped polycrystal. Science 321(5887):382–385. https://doi.org/10.1126/science.1156211
74. Bonnin A, Wright JP, Tucoulou R, Palancher H (2014) Impurity precipitation in atomized particles evidenced by nano x-ray diffraction computed tomography. Appl Phys Lett 105(8):084103. https://doi.org/10.1063/1.4894009
75. Ludwig W, King A, Reischig P, Herbig M, Lauridsen EM, Schmidt S, Proudhon H, Forest S, Cloetens P, Du Roscoat SR et al (2009) New opportunities for 3d materials science of polycrystalline materials at the micrometre lengthscale by combined use of x-ray diffraction and x-ray imaging. Mater Sci Eng A 524(1–2):69–76. https://doi.org/10.1016/j.msea.2009.04.009
76. Naragani DP, Park J-S, Kenesei P, Sangid MD (2020) Void coalescence and ductile failure in in718 investigated via high-energy synchrotron x-ray tomography and diffraction. J Mech Phys Solids 145:104155. https://doi.org/10.1016/j.jmps.2020.104155
77. Zhang Z, Wang C, Koe B, Schlepütz CM, Irvine S, Mi J (2021) Synchrotron x-ray imaging and ultrafast tomography in situ study of the fragmentation and growth dynamics of dendritic microstructures in solidification under ultrasound. Acta Mater 209:116796. https://doi.org/10.1016/j.actamat.2021.116796
78. McDonald SA, Burnett TL, Donoghue J, Gueninchault N, Bale H, Holzner C, Lauridsen EM, Withers PJ (2021) Tracking polycrystal evolution non-destructively in 3d by laboratory x-ray diffraction contrast tomography. Mater Charac 172:110814. https://doi.org/10.1016/j.matchar.2020.110814
79. Ravi P, Naragani D, Kenesei P, Park J-S, Sangid MD (2021) Direct observations and characterization of crack closure during microstructurally small fatigue crack growth via in-situ high-energy x-ray characterization. Acta Mater 205:116564. https://doi.org/10.1016/j.actamat.2020.116564
80. Ge M, Huang X, Yan H, Gursoy D, Meng Y, Zhang J, Ghose S, Chiu WK, Brinkman KS, Chu YS (2022) Three-dimensional imaging of grain boundaries via quantitative fluorescence x-ray tomography analysis. Commun Mater 3(1):1–11. https://doi.org/10.1038/s43246-022-00259-x
81. Ice GE, Budai JD, Pang JW (2011) The race to x-ray microbeam and nanobeam science. Science 334(6060):1234–1239. https://doi.org/10.1126/science.1202366
82. Dai J, Xia J, Chai L, Murty KL, Guo N, Daymond MR (2020) Correlation of microstructural, textural characteristics and hardness of ti-6al-4v sheet β -cooled at different rates. J Mater Sci 55(19):8346–8362. https://doi.org/10.1007/s10853-020-04603-9
83. Levine LE, Larson BC, Yang W, Kassner ME, Tischler JZ, Delos-Reyes MA, Fields RJ, Liu W (2006) X-ray microbeam measurements of individual dislocation cell elastic strains in deformed single-crystal copper. Nat Mater 5(8):619–622. https://doi.org/10.1038/nmat1698
84. Hayashi Y, Hirose Y, Seno Y (2015) Polycrystal orientation mapping using scanning three-dimensional x-ray diffraction microscopy. J Appl Crystallogr 48(4):1094–1101. https://doi.org/10.1107/S1600576715009899
85. Henningsson A, Hendriks, J (2021) Intragranular strain estimation in far-field scanning x-ray diffraction using a gaussian process. J Appl Crystallogr 54(4). https://doi.org/10.1107/s1600576721005112
86. Hayashi Y, Setoyama D, Hirose Y, Yoshida T, Kimura H (2019) Intragranular three-dimensional stress tensor fields in plastically deformed polycrystals. Science 366(6472):1492–1496. https://doi.org/10.1126/science.aax9167
87. Johnson QC, Kenesei P, Petruzza S, Plumb J, Sharma H, Park J-S, Marsden E, Matheson K, Czabaj MW, Spear AD (2023) Mapping 3d grain and precipitate structure during in situ mechanical testing of open-cell metal foam using micro-computed tomography and high-energy x-ray diffraction microscopy. Mater Charac 195:112477. https://doi.org/10.1016/j.matchar.2022.112477
88. Reischig P, Ludwig W (2020) Three-dimensional reconstruction of intragranular strain and orientation in polycrystals by near-field x-ray diffraction. Curr Opin Solid State Mater Sci 24(5):100851. https://doi.org/10.1016/j.cossms.2020.100851
89. Stinville J, Ludwig W, Callahan P, Echlin M, Valle V, Pollock T, Proudhon H (2022) Observation of bulk plasticity in a polycrystalline titanium alloy by diffraction contrast tomography and topotomography. Mater Charac 188:111891
90. Herbig M, King A, Reischig P, Proudhon H, Lauridsen EM, Marrow J, Buffière J-Y, Ludwig W (2011) 3-d growth of a short fatigue crack within a polycrystalline microstructure studied using combined diffraction and phase-contrast x-ray tomography. Acta Mater 59(2):590–601. https://doi.org/10.1016/j.actamat.2010.09.063
91. Lauridsen EM, Schmidt S, Suter R, Poulsen HF (2001) Tracking: a method for structural characterization of grains in powders or polycrystals. J Appl Crystallogr 34(6):744–750. https://doi.org/10.1107/S0021889801014170
92. Schmidt S (2014) Grainspotter: a fast and robust polycrystalline indexing algorithm. J Appl Crystallogr 47(1):276–284. https://doi.org/10.1107/S1600576713030185

93. Poulsen HF, Fu X (2003) Generation of grain maps by an algebraic reconstruction technique. J Appl Crystallogr 36(4):1062–1068. https://doi.org/10.1107/S0021889803011063
94. Schmidt S, Olsen UL, Poulsen HF, Sørensen HO, Lauridsen EM, Margulies L, Maurice C, Jensen DJ (2008) Direct observation of 3-d grain growth in al–0.1% mn. Scr Mater 59(5):491–494. https://doi.org/10.1016/j.scriptamat.2008.04.049
95. Suter R, Hennessy D, Xiao C, Lienert U (2006) Forward modeling method for microstructure reconstruction using x-ray diffraction microscopy: Single-crystal verification. Rev Sci Instrum 77(12):123905. https://doi.org/10.1063/1.2400017
96. Liu Z, Sharma H, Park JS, Kenesei P, Miceli A, Almer J, Kettimuthu R, Foster I (2022) BraggNN: fast X-ray Bragg peak analysis using deep learning. IUCrJ 9(1):104–13. https://doi.org/10.48550/arXiv.2008.08198
97. Avizo for materials science (2018). https://www.fei.com/software/avizo-for-materials-science
98. Renversade L, Quey R, Ludwig W, Menasche D, Maddali S, Suter RM, Borbely A (2016) Comparison between diffraction contrast tomography and high-energy diffraction microscopy on a slightly deformed aluminium alloy. IUCrJ 3(1):32–42. https://doi.org/10.1107/s2052252515019995
99. Fang H, Juul Jensen D, Zhang Y (2021) Improved grain mapping by laboratory x-ray diffraction contrast tomography. IUCrJ 8(4):559–573. https://doi.org/10.1107/S2052252521003730
100. Yang L, Hilty F, Muralikrishnan V, Silva-Reyes K, Harley JB, Krause AR, Tonks MR (2022) Calculating the grain boundary inclination of voxelated grain structures using a smoothing algorithm. Scr Mater 218:114796. https://doi.org/10.1016/j.scriptamat.2022.114796
101. Henningsson NA, Hall SA, Wright JP, Hektor J (2020) Reconstructing intragranular strain fields in polycrystalline materials from scanning 3DXRD data. Appl Crystallogr 53(2):314–25. https://doi.org/10.1107/S1600576720001016
102. Reid AC, Langer SA, Lua RC, Coffman VR, Haan S-I, García RE (2008) Image-based finite element mesh construction for material microstructures. Comput Mater Sci 43(4):989–999. https://doi.org/10.1016/j.commatsci.2008.02.016
103. Simonovski I, Cizelj L (2011) Automatic parallel generation of finite element meshes for complex spatial structures. Comput Mater Sci 50(5):1606–1618. https://doi.org/10.1016/j.commatsci.2010.12.014
104. Simons H, King A, Ludwig W, Detlefs C, Pantleon W, Schmidt S, Stöhr F, Snigireva I, Snigirev A, Poulsen HF (2015) Dark-field x-ray microscopy for multiscale structural characterization. Nat Commun 6(1):1–6. https://doi.org/10.1038/ncomms7098
105. Poulsen H, Cook P, Leemreize H, Pedersen A, Yildirim C, Kutsal M, Jakobsen A, Trujillo J, Ormstrup J, Detlefs C (2018) Reciprocal space mapping and strain scanning using x-ray diffraction microscopy. J Appl Crystallogr 51(5):1428–1436. https://doi.org/10.1107/S1600576718011378
106. Ludwig W, Lauridsen EM, Schmidt S, Poulsen HF, Baruchel J (2007) High-resolution three-dimensional mapping of individual grains in polycrystals by topotomography. J Appl Crystallogr 40(5):905–911. https://doi.org/10.1107/S002188980703035X
107. Fang H, Hovad E, Zhang Y, Clemmensen LK, Ersbøll BK, Juul Jensen D (2021) Deep learning for improving non-destructive grain mapping in 3D. IUCrJ 8(5):719–31. https://doi.org/10.1107/S2052252521005480
108. Wu G, Zhu W, He Q, Feng Z, Huang T, Zhang L, Schmidt S, Godfrey A, Huang X (2020) 2d and 3d orientation mapping in nanostructured metals: a review. NMS 2(1):50–57. https://doi.org/10.1016/j.nanoms.2020.03.006
109. Liu H, Schmidt S, Poulsen HF, Godfrey A, Liu Z, Sharon J, Huang X (2011) Three-dimensional orientation mapping in the transmission electron microscope. Science 332(6031):833–834. https://doi.org/10.1126/science.1202202
110. Eggeman AS, Krakow R, Midgley PA (2015) Scanning precession electron tomography for three-dimensional nanoscale orientation imaging and crystallographic analysis. Nat Commun 6(1):1–7. https://doi.org/10.1038/ncomms8267
111. Derazkola HA, Garcia E, Murillo-Marrodán A, Fernandez AC (2022) Review on modeling and simulation of dynamic recrystallization of martensitic stainless steels during bulk hot deformation. J Mater Res Technol 1(18):2993–3025. https://doi.org/10.1016/j.jmrt.2022.03.179
112. Zhang Z, Wang Y, Ge P, Wu T (2022) A review on modelling and simulation of laser additive manufacturing: Heat transfer, microstructure evolutions and mechanical properties. Coatings 12(9):1277. https://doi.org/10.3390/coatings12091277
113. Li J, Zhou X, Brochu M, Provatas N, Zhao YF (2020) Solidification microstructure simulation of ti-6al-4v in metal additive manufacturing: a review. Addit Manuf 31:100989. https://doi.org/10.1016/j.addma.2019.100989
114. Janssens KG (2003) Random grid, three-dimensional, space-time coupled cellular automata for the simulation of recrystallization and grain growth. Model Simul Mat Sci Eng 11(2):157. https://doi.org/10.1088/0965-0393/11/2/304
115. Yazdipour N, Davies CH, Hodgson PD (2008) Microstructural modeling of dynamic recrystallization using irregular cellular automata. Comput Mater Sci 44(2):566–576. https://doi.org/10.1016/j.commatsci.2008.04.027
116. Chen S-F, Bandyopadhyay K, Basak S, Hwang B, Shim J-H, Lee J, Lee M-G (2021) Predictive integrated numerical approach for modeling spatio-temporal microstructure evolutions and grain size dependent phase transformations in steels. Int J Plast 139:102952. https://doi.org/10.1016/j.ijplas.2021.102952
117. Hesselbarth HW, Göbel I (1991) Simulation of recrystallization by cellular automata. Acta Met Mater 39(9):2135–2143. https://doi.org/10.1016/0956-7151(91)90183-2
118. Popova E, Staraselski Y, Brahme A, Mishra R, Inal K (2015) Coupled crystal plasticity-probabilistic cellular automata approach to model dynamic recrystallization in magnesium alloys. Int J Plast 66:85–102. https://doi.org/10.1016/j.ijplas.2014.04.008
119. Hallberg H, Wallin M, Ristinmaa M (2010) Simulation of discontinuous dynamic recrystallization in pure cu using a probabilistic cellular automaton. Comput Mater Sci 49(1):25–34. https://doi.org/10.1016/j.commatsci.2010.04.012
120. Gottstein G, Shvindlerman LS (2009) Grain boundary migration in metals: thermodynamics, kinetics, applications. CRC press, Boca Raton, pp 134–140. https://doi.org/10.1201/9781420054361
121. Fan R, Wu Y, Chen M, Zhao J (2022) Prediction of anisotropic deformation behavior of ta32 titanium alloy sheet during hot tension by crystal plasticity finite element model. Mater Sci Eng A 843:143137. https://doi.org/10.1016/j.msea.2022.143137
122. Chen F, Zhu H, Chen W, Ou H, Cui Z (2021) Multiscale modeling of discontinuous dynamic recrystallization during hot working by coupling multilevel cellular automaton and finite element method. Int J Plast 145:103064. https://doi.org/10.1016/j.ijplas.2021.103064
123. Łach Ł, Nowak J, Svyetlichnyy D (2018) The evolution of the microstructure in aisi 304l stainless steel during the flat rolling-modeling by frontal cellular automata and verification. J Mater Process Technol 255:488–499. https://doi.org/10.1016/j.jmatprotec.2017.12.001
124. Zheng C, Xiao N, Li D, Li Y (2008) Microstructure prediction of the austenite recrystallization during multi-pass steel strip

hot rolling: a cellular automaton modeling. Comput Mater Sci 44(2):507–514. https://doi.org/10.1016/j.commatsci.2008.04.010
125. Chen F, Tian X, Wu G, Zhu H, Ou H, Cui Z (2022) Coupled quantitative modeling of microstructural evolution and plastic flow during continuous dynamic recrystallization. Int J Plast 156:103372. https://doi.org/10.1016/j.ijplas.2022.103372
126. Li W, Li S, Li X, Xu D, Shao Y, Attallah MM, Essa K (2022) Crystal plasticity model of induction heating-assisted incremental sheet forming with recrystallisation simulation in cellular automata. Int J Adv Manuf Technol 123(3):903–25. https://doi.org/10.1007/s00170-022-10203-5
127. Asgharzadeh A, Tiji SAN, Park T, Pourboghrat F (2022) Prediction of softening kinetics and recrystallization texture in non-isothermally annealed bulged tubes using cpfem and ca models. Mater Sci Eng A 832:142308. https://doi.org/10.1016/j.msea.2021.142308
128. He YY, Bai SW, Fang G (2022) Coupled CA-FE simulation for dynamic recrystallization of magnesium alloy during hot extrusion. J Magnes Alloys 10(3):769–85. https://doi.org/10.1016/j.jma.2020.08.023
129. Romanova V, Mohebbi MS, Dymnich E, Balokhonov R, Ploshikhin V (2022) A physically-based computational approach for processing-microstructure-property linkage of materials additively manufactured by laser powder bed fusion. Int J Mech Sci 219:107103. https://doi.org/10.1016/j.ijmecsci.2022.107103
130. Trinh TD, Iwamoto T (2021) A crystal plasticity simulation on strain-induced martensitic transformation in crystalline trip steel by coupling with cellular automata. Metals 11(8):1316. https://doi.org/10.3390/met11081316
131. Zhou X, Zhang H, Wang G, Bai X, Fu Y, Zhao J (2016) Simulation of microstructure evolution during hybrid deposition and micro-rolling process. J Mater Sci 51(14):6735–6749. https://doi.org/10.1007/s10853-016-9961-0
132. Kühbach M, Gottstein G, Barrales-Mora L (2016) A statistical ensemble cellular automaton microstructure model for primary recrystallization. Acta Mater 107:366–376. https://doi.org/10.1016/j.actamat.2016.01.068
133. Liu X, Li H, Zhan M (2018) A review on the modeling and simulations of solid-state diffusional phase transformations in metals and alloys. Manuf Rev 5:10. https://doi.org/10.1051/mfreview/2018008
134. Hallberg H (2011) Approaches to modeling of recrystallization. Metals 1(1):16–48. https://doi.org/10.3390/met1010016
135. Rodgers TM, Moser D, Abdeljawad F, Jackson ODU, Carroll JD, Jared BH, Bolintineanu DS, Mitchell JA, Madison JD (2021) Simulation of powder bed metal additive manufacturing microstructures with coupled finite difference-monte carlo method. Addit Manuf 41:101953. https://doi.org/10.1016/j.addma.2021.101953
136. Lee W, Jeong Y, Lee J-W, Lee H, Kang S-H, Kim Y-M, Yoon J (2020) Numerical simulation for dendrite growth in directional solidification using lbm-ca (cellular automata) coupled method. J Mater Sci Technol 49:15–24. https://doi.org/10.1016/j.jmst.2020.01.047
137. Xu F, Xiong F, Li M-J, Lian Y (2022) Three-dimensional numerical simulation of grain growth during selective laser melting of 316l stainless steel. Materials 15(19):6800. https://doi.org/10.3390/ma15196800
138. Xue C, Blanc N, Soulié F, Bordreuil C, Deschaux-Beaume F, Guillemot G, Bellet M, Gandin C-A (2022) Structure and texture simulations in fusion welding processes-comparison with experimental data. Materialia 21:101305. https://doi.org/10.1016/j.mtla.2021.101305
139. Wei J, Wang X, Cai L, Yao M (2022) Modeling of the nonuniform microstructure and microsegregation formation of the shell in round billet continuous casting. Steel Res Int. https://doi.org/10.1002/srin.202100793
140. Teferra K, Rowenhorst DJ (2021) Optimizing the cellular automata finite element model for additive manufacturing to simulate large microstructures. Acta Mater 213:116930. https://doi.org/10.1016/j.actamat.2021.116930
141. Shi L, Xu S, Lu H, Chen C, Shuai S, Hu T, Kao A, Wang J, Ren Z (2022) A high-efficiency virtual submesh cellular automata method for solidification simulation with low mesh anisotropy. ISIJ Int 62(8):1674–1683. https://doi.org/10.2355/isijinternational.ISIJINT-2022-066
142. Li J, Zhou X, Meng Q, Brochu M, Chekir N, Sixsmith J, Hascoët J, Zhao YF (2021) Deterministic modeling of solidification microstructure formation in directed energy deposition fabricated ti6al4v. Addit Manuf 46:102182. https://doi.org/10.1016/j.addma.2021.102182
143. Liu S, Shin YC (2020) Prediction of 3d microstructure and phase distributions of ti6al4v built by the directed energy deposition process via combined multi-physics models. Addit Manuf 34:101234. https://doi.org/10.1016/j.addma.2020.101234
144. Lin X, Zou X, An D, Krakauer BW, Zhu M (2021) Multi-scale modeling of microstructure evolution during multi-pass hot-rolling and cooling process. Materials 14(11):2947. https://doi.org/10.3390/ma14112947
145. Łach Ł, Svyetlichnyy D (2020) Development of hybrid model for modeling of diffusion phase transformation. Eng Comput. https://doi.org/10.1108/ec-02-2019-0059
146. Boccardo AD, Dardati P, Godoy LA (2018) A cellular automaton-finite difference simulation of the ausferritic transformation in ductile iron. Mater Sci Technol 34(14):1710–1722. https://doi.org/10.1080/02670836.2018.1475035
147. Fang H, Tang Q, Zhang Q, Fan Y, Pan S, Rettenmayr M, Zhu M (2022) Simulation of the peritectic phase transition in fe-c alloys. Materials 15(2):537. https://doi.org/10.3390/ma15020537
148. Jia C, Zheng C, Li D (2020) Cellular automaton modeling of austenite formation from ferrite plus pearlite microstructures during intercritical annealing of a c-mn steel. J Mater Sci Technol 47:1–9. https://doi.org/10.1016/j.jmst.2020.02.002
149. Guo Y, Liu M, Yin M, Yan Y (2020) Modeling of the evolution of the microstructure and the hardness penetration depth for a hypoeutectoid steel processed by grind-hardening. Metals 10(9):1182. https://doi.org/10.3390/met10091182
150. Chen S, Xu Y, Jiao Y (2018) A hybrid finite-element and cellular-automaton framework for modeling 3d microstructure of ti-6al-4v alloy during solid-solid phase transformation in additive manufacturing. Model Simul Mat Sci Eng 26(4):045011. https://doi.org/10.1088/1361-651x/aabcad
151. Yu Y, Kenevisi MS, Yan W, Lin F (2020) Modeling precipitation process of al-cu alloy in electron beam selective melting with a 3d cellular automaton model. Addit Manuf 36:101423. https://doi.org/10.1016/j.addma.2020.101423
152. Hore S, Das SK, Banerjee S, Mukherjee S (2013) A multiscale coupled monte carlo model to characterize microstructure evolution during hot rolling of mo-trip steel. Acta Mater 61(19):7251–7259. https://doi.org/10.1016/j.actamat.2013.08.030
153. Kim T-Y, Na T-W, Shim H-S, Gil K, Hwang N-M (2022) Effect of the magnitude of sub-boundary angles on the abnormal grain growth rate of goss grains in fe-3% si steel. Mater Charact 184:111655. https://doi.org/10.1016/j.matchar.2021.111655
154. Sunny S, Yu H, Mathews R, Malik A, Li W (2021) Improved grain structure prediction in metal additive manufacturing using a dynamic kinetic monte carlo framework. Addit Manuf 37:101649. https://doi.org/10.1016/j.addma.2020.101649
155. Jedrychowski M, Bacroix B, Tarasiuk J, Wroński S (2021) Monte carlo modelling of recrystallization in alpha zirconium. Comput

Mater Sci 199:110742. https://doi.org/10.1016/j.commatsci.2021.110742
156. Beck M, Morse M, Corolewski C, Fritchman K, Stifter C, Poole C, Hurley M, Frary M (2017) Understanding the effect of grain boundary character on dynamic recrystallization in stainless steel 316l. Metall Mater Trans A 48(8):3831–3842. https://doi.org/10.1007/s11661-017-4133-7
157. Yu P, Wu C, Shi L (2021) Analysis and characterization of dynamic recrystallization and grain structure evolution in friction stir welding of aluminum plates. Acta Mater 207:116692. https://doi.org/10.1016/j.actamat.2021.116692
158. Sunny S, Gleason G, Bailey K, Mathews R, Malik A (2021) Importance of microstructure modeling for additively manufactured metal post-process simulations. Int J Eng Sci 166:103515. https://doi.org/10.1016/j.ijengsci.2021.103515
159. Tutcuoglu AD, Vidyasagar A, Bhattacharya K, Kochmann D (2019) Stochastic modeling of discontinuous dynamic recrystallization at finite strains in hcp metals. J Mech Phys Solids 122:590–612. https://doi.org/10.1016/j.jmps.2018.09.032
160. Zhang Z, Tan Z-J, Li J-Y, Zu Y-F, Sha J-J (2020) Integrated modeling of process-microstructure-property relations in friction stir additive manufacturing. ACTA METALL SIN-ENGL 33(1):75–87. https://doi.org/10.1007/s40195-019-00945-9
161. Eivani A, Jafarian H, Zhou J (2020) Simulation of peripheral coarse grain structure during hot extrusion of aa7020 aluminum alloy. J Manuf Process 57:881–892. https://doi.org/10.1016/j.jmapro.2020.07.011
162. Mohseni M, Eivani A, Vafaeenezhad H, Jafarian H, Salehi M, Zhou J (2021) An experimental and theoretical investigation of the effect of second-phase particles on grain growth during the annealing of hot-rolled az61 magnesium alloy. J Mater Res Technol 15:3585–3597. https://doi.org/10.1016/j.jmrt.2021.09.049
163. Khodabakhshi F, Derazkola HA, Gerlich A (2020) Monte carlo simulation of grain refinement during friction stir processing. J Mater Sci 55(27):13438–13456. https://doi.org/10.1007/s10853-020-04963-2
164. Zhang Z, Ge P, Li JY, Ren DX, Wu T (2022) Monte carlo simulations of solidification and solid-state phase transformation during directed energy deposition additive manufacturing. Progress Addit Manuf 7(4):671–82. https://doi.org/10.1007/s40964-021-00253-8
165. Rodgers TM, Madison JD, Tikare V (2017) Simulation of metal additive manufacturing microstructures using kinetic monte carlo. Comput Mater Sci 135:78–89. https://doi.org/10.1016/j.commatsci.2017.03.053
166. Pauza J, Tayon W, Rollett A (2021) Computer simulation of microstructure development in powder-bed additive manufacturing with crystallographic texture. Model Simul Mat Sci Eng 29(5):055019. https://doi.org/10.1088/1361-651x/ac03a6
167. Plimpton S, Corbett Battaile MC, Holm L, Thompson A, Tikare V, Wagner G, Zhou X, Cardona CG, Slepoy A (2009) Crossing the mesoscale no-man's land via parallel kinetic monte carlo. Sandia Report SAND2009-6226 1. https://doi.org/10.2172/966942
168. Li W, Soshi M (2019) Modeling analysis of the effect of laser transverse speed on grain morphology during directed energy deposition process. J Adv Manuf Technol 103(9):3279–3291. https://doi.org/10.1007/s00170-019-03690-6
169. Zhang Z, Tan Z, Yao X, Hu C, Ge P, Wan Z, Li J, Wu Q (2019) Numerical methods for microstructural evolutions in laser additive manufacturing. Comput Math Appl 78(7):2296–2307. https://doi.org/10.1016/j.camwa.2018.07.011
170. Berry J, Perron A, Fattebert J-L, Roehling JD, Vrancken B, Roehling TT, Rosas DL, Turner JA, Khairallah SA, McKeown JT et al (2021) Toward multiscale simulations of tailored microstructure formation in metal additive manufacturing. Mater Today 51:65–86. https://doi.org/10.1016/j.mattod.2021.09.024
171. Zhang C, Yadav V, Moelans N, Jensen DJ, Yu T (2022) The effect of voids on boundary migration during recrystallization in additive manufactured samples-a phase field study. Scr Mater 214:114675. https://doi.org/10.1016/j.scriptamat.2022.114675
172. Tourret D, Liu H, LLorca J (2022) Phase-field modeling of microstructure evolution: recent applications, perspectives and challenges. Prog Mater Sci 123:100810. https://doi.org/10.1016/j.pmatsci.2021.100810
173. Sinhababu A, Bhattacharya A (2022) A fixed grid based accurate phase-field method for dendritic solidification in complex geometries. Comput Mater Sci 202:110973. https://doi.org/10.1016/j.commatsci.2021.110973
174. Li Z, Tang S, Liang C, Liu W, Ma Y (2022) Phase-field investigation on the grain evolution and mechanical response during dynamic recrystallization of deforming tungsten. Mater Today Commun 32:104174. https://doi.org/10.1016/j.mtcomm.2022.104174
175. Da Y, Xiao Y, Zhong Z, Pan Z, Jiao Z (2022) Predictions on conductivity and mechanical property evolutions of yttria-stabilized zirconia in solid oxide fuel cells based on phase-field modeling of cubic-tetragonal phase transformation. J Eur Ceram Soc 42(8):3489–3499. https://doi.org/10.1016/j.jeurceramsoc.2022.03.012
176. Li B, Jin S, Xue B, Liang L, Lu G-H (2022) Phase-field microstructure-based effective thermal conductivity calculations in tungsten. Nucl Fusion 62(7):076041. https://doi.org/10.1088/1741-4326/ac6284
177. Cissé C, Zaeem MA (2021) Transformation-induced fracture toughening in cualbe shape memory alloys: a phase-field study. Int J Mech Sci 192:106144. https://doi.org/10.1016/j.ijmecsci.2020.106144
178. Xu B, Yu C, Kang G (2021) Phase field study on the microscopic mechanism of grain size dependent cyclic degradation of super-elasticity and shape memory effect in nano-polycrystalline niti alloys. Int J Plast 145:103075. https://doi.org/10.1016/j.ijplas.2021.103075
179. Cahn JW (1961) On spinodal decomposition sur la decomposition spinodale über die umsetzung an der spinodalen. Acta Metall 9(9):795–801. https://doi.org/10.1016/0001-6160(61)90182-1
180. Allen SM, Cahn JW (1979) A microscopic theory for antiphase boundary motion and its application to antiphase domain coarsening. Acta Metall 27(6):1085–1095. https://doi.org/10.1016/0001-6160(79)90196-2
181. Zhang A, Du J, Guo Z, Wang Q, Xiong S (2021) Evolution of specific interface area during solidification: a three-dimensional thermosolutal phase-field study. Comput Phys Commun 267:108042. https://doi.org/10.1016/j.cpc.2021.108042
182. Ji K, Tabrizi AM, Karma A (2022) Isotropic finite-difference approximations for phase-field simulations of polycrystalline alloy solidification. J Comput Phys 457:111069. https://doi.org/10.1016/j.jcp.2022.111069
183. Lindroos M, Pinomaa T, Ammar K, Laukkanen A, Provatas N, Forest S (2022) Dislocation density in cellular rapid solidification using phase field modeling and crystal plasticity. Int J Plast 148:103139. https://doi.org/10.1016/j.ijplas.2021.103139
184. Ghoneim AY (2020) A smoothed particle hydrodynamics-phase field method with radial basis functions and moving least squares for meshfree simulation of dendritic solidification. Appl Math Model 77:1704–1741. https://doi.org/10.1016/j.apm.2019.09.017
185. DeWitt S, Rudraraju S, Montiel D, Andrews WB, Thornton K (2020) Prisms-pf: a general framework for phase-field modeling with a matrix-free finite element method. Npj Comput Mater 6(1):1–12. https://doi.org/10.1038/s41524-020-0298-5

186. Javaheri DL (2017) Jason Gruber: Mesoscale microstructure simulation project (mmsp). https://github.com/mesoscale/mmsp
187. Hamed A, Rayaprolu S, Winther G, El-Azab A (2022) Impact of the plastic deformation microstructure in metals on the kinetics of recrystallization: a phase-field study. Acta Mater 240:118332. https://doi.org/10.1016/j.actamat.2022.118332
188. Cai Y, Sun C, Li Y, Hu S, Zhu N, Barker EI, Qian L (2020) Phase field modeling of discontinuous dynamic recrystallization in hot deformation of magnesium alloys. Int J Plast 133:102773. https://doi.org/10.1016/j.ijplas.2020.102773
189. Sadeghian B, Taherizadeh A, Atapour M, Saeidi N, Alhaji A (2021) Phase-field simulation of microstructure evolution during friction stir welding of 304 stainless steel. Mech Mater 163:104076. https://doi.org/10.1016/j.mechmat.2021.104076
190. Zhang Q, Fang G (2022) An efficient grain remapping algorithm for phase-field modeling of dynamic recrystallization. Comput Mater Sci 215:111778. https://doi.org/10.1016/j.commatsci.2022.111778
191. Zhao P, Wang Y, Niezgoda SR (2018) Microstructural and micromechanical evolution during dynamic recrystallization. Int J Plast 100:52–68. https://doi.org/10.1016/j.ijplas.2017.09.009
192. Min K, Jeong W, Hong S, Lee C, Cha P-R, Han H, Lee M-G (2020) Integrated crystal plasticity and phase field model for prediction of recrystallization texture and anisotropic mechanical properties of cold-rolled ultra-low carbon steels. Int J Plast 127:102644. https://doi.org/10.1016/j.ijplas.2019.102644
193. Zhu N, Sun C, Li YL, Qian L, Hu SY, Cai Y, Feng Y (2021) Modeling discontinuous dynamic recrystallization containing second phase particles in magnesium alloys utilizing phase field method. Comput Mater Sci 200:110858. https://doi.org/10.1016/j.commatsci.2021.110858
194. Jiang Y, Xin Y, Liu W, Sun Z, Chen P, Sun D, Zhou M, Liu X, Yun D (2022) Phase-field simulation of radiation-induced bubble evolution in recrystallized u-mo alloy. Nucl Eng Technol 54(1):226–233. https://doi.org/10.1016/j.net.2021.07.034
195. Yang C, Wu C, Shi L (2020) Phase-field modelling of dynamic recrystallization process during friction stir welding of aluminium alloys. Sci Technol Weld Join 25(4):345–358. https://doi.org/10.1080/13621718.2019.1706261
196. Yang C, Wu C, Shi L (2020) Effect of ultrasonic vibration on dynamic recrystallization in friction stir welding. J Manuf Process 56:87–95. https://doi.org/10.1016/j.jmapro.2020.04.064
197. Yamanaka A, Maeda Y, Sasaki K (2019) Ensemble kalman filter-based data assimilation for three-dimensional multi-phase-field model: estimation of anisotropic grain boundary properties. Mater Des 165:107577. https://doi.org/10.1016/j.matdes.2018.107577
198. Zhang X, Ye W, Mushongera L, Liao Y (2022) Unravelling heterogeneities in sub-grain cellular structure and micromechanical response of additive manufactured ti-nb alloys. Addit Manuf 59:103146. https://doi.org/10.1016/j.addma.2022.103146
199. Han C, Jiang P, Geng S, Gao S, Mi G, Wang C (2021) Multiphase-field simulation of grain coalescence behavior and its effects on solidification cracking susceptibility during welding of al-cu alloys. Mater Des 211:110146. https://doi.org/10.1016/j.matdes.2021.110146
200. Xu B, Xiong J, Yu C, Wang C, Wang Q, Kang G (2022) Improved elastocaloric effect of niti shape memory alloys via microstructure engineering: a phase field simulation. Int J Mech Sci 222:107256. https://doi.org/10.1016/j.ijmecsci.2022.107256
201. Rezaei Y, Jafari M, Jamshidian M (2021) Phase-field modeling of magnetic field-induced grain growth in polycrystalline metals. Comput Mater Sci 200:110786. https://doi.org/10.1016/j.commatsci.2021.110786
202. Yadav V, Moelans N, Zhang Y, Jensen DJ (2021) Effects of dislocation boundary spacings and stored energy on boundary migration during recrystallization: a phase-field analysis. Acta Mater 221:117377. https://doi.org/10.1016/j.actamat.2021.117377
203. Miyoshi E, Takaki T, Sakane S, Ohno M, Shibuta Y, Aoki T (2021) Large-scale phase-field study of anisotropic grain growth: effects of misorientation-dependent grain boundary energy and mobility. Comput Mater Sci 186:109992. https://doi.org/10.1016/j.commatsci.2020.109992
204. Wang M, Xu Y, Hu J, Fang F, Jin J, Jia T, Peng Q (2022) Phase-field simulation on the effect of second-phase particles on abnormal growth of goss grains in fe-3% si steels. Nanomaterials 12(23):4148. https://doi.org/10.3390/nano12234148
205. Hosseinzadeh H, Nematollahi M, Safaei K, Abedi H, Bayati P, Javan R, Poorganji B, Yuan L, Elahinia M (2022) A numerical approach to model microstructure evolution for niti shape memory alloy in laser powder bed fusion additive manufacturing. Integr Mater Manuf Innov 11(1):121–138. https://doi.org/10.1007/s40192-022-00252-9
206. Dimokrati A, Le Bouar Y, Benyoucef M, Finel A (2020) S-pfm model for ideal grain growth. Acta Mater 201:147–157. https://doi.org/10.1016/j.actamat.2020.09.073
207. Azizi H, Ebrahimi A, Ofori-Opoku N, Greenwood M, Provatas N, Mohammadi M (2021) Characterizing the microstructural effect of build direction during solidification of laser-powder bed fusion of al-si alloys in the dilute limit: a phase-field study. Acta Mater 214:10.1016/j.actamat.2021.116983. https://doi.org/10.1016/j.actamat.2021.116983
208. Xiao Y, Wan Z, Liu P, Wang Z, Li J, Chen L (2022) Quantitative simulations of grain nucleation and growth at additively manufactured bimetallic interfaces of ss316l and in625. J Mater Process Technol 302:117506. https://doi.org/10.1016/j.jmatprotec.2022.117506
209. Ren J-K, Sun M-Y, Chen Y, Xu B, Liu W-F, Jiang H-Y, Cao Y-F, Li D-Z (2022) The non-dendritic microstructure arising from grain boundary formation and wetting: a phase-field simulation and experimental investigation of semi-solid deformation. Mater Des 223:111111. https://doi.org/10.1016/j.matdes.2022.111111
210. Ren J-K, Chen Y, Cao Y-F, Xu B, Sun M-Y, Li D-Z (2021) A phase-field simulation of the solidification process under compression. J Mater Res Technol 13:2210–2219. https://doi.org/10.1016/j.jmrt.2021.05.081
211. Yamanaka N, Sakane S, Takaki T (2021) Multi-phase-field lattice boltzmann model for polycrystalline equiaxed solidification with motion. Comput Mater Sci 197:110658. https://doi.org/10.1016/j.commatsci.2021.110658
212. Okugawa M, Ohigashi Y, Furishiro Y, Koizumi Y, Nakano T (2022) Equiaxed grain formation by intrinsic heterogeneous nucleation via rapid heating and cooling in additive manufacturing of aluminum-silicon hypoeutectic alloy. J Alloys Compd. https://doi.org/10.1016/j.jallcom.2022.165812
213. Guo C, Weng K, Wang J, Zhao H, Dong X, Fan Y, Li J (2022) Competitive growth of diverging columnar grains during directional solidification: a three-dimensional phase-field study. Comput Mater Sci 210:111061. https://doi.org/10.1016/j.commatsci.2021.111061
214. Lingda X, Guoli Z, Gaoyang M, Chunming W, Ping J (2021) A phase-field simulation of columnar-to-equiaxed transition in the entire laser welding molten pool. J Alloys Compd 858:157669. https://doi.org/10.1016/j.jallcom.2020.157669
215. Laskowski R, Ahluwalia R, Hock GTW, Ying CS, Sun C-N, Wang P, Cheh DTC, Sharon NML, Vastola G, Zhang Y-W (2022) Concurrent modeling of porosity and microstructure in multilayer three-dimensional simulations of powder-bed fusion additive manufacturing of inconel 718. Addit Manuf 60:103266. https://doi.org/10.1016/j.addma.2022.103266

216. Chadwick AF, Voorhees PW (2021) The development of grain structure during additive manufacturing. Acta Mater 211:116862. https://doi.org/10.1016/j.actamat.2021.116862
217. Chen W, Zhao Y, Yang S, Zhang D, Hou H (2021) Three-dimensional phase-field simulations of the influence of diffusion interface width on dendritic growth of fe-0.5 wt.% c alloy. Adv Compos Hybrid Mater 4(2):371–378. https://doi.org/10.1007/s42114-021-00215-2
218. Zhang Z, Hou X, Zhang Y, Wei H, Wang J (2022) Phase field simulation of solidification under supergravity. Acta Mech Sin 38(8):122031. https://doi.org/10.1007/s10409-022-22031-x
219. Laxmipathy VP, Wang F, Selzer M, Nestler B (2021) A two-dimensional phase-field study on dendritic growth competition under convective conditions. Comput Mater Sci 186:109964. https://doi.org/10.1016/j.commatsci.2020.109964
220. Qu W, Luo M, Guo Z, Hu X, Zhang A, Zhang F, Lu H, Zhang Y, Li D (2020) Microstructural evolution mechanism of semi-solid slurry: a study using phase-field-lattice-boltzmann scheme. J Mater Process Technol 280:116592. https://doi.org/10.1016/j.jmatprotec.2020.116592
221. Pinomaa T, Lindroos M, Walbrühl M, Provatas N, Laukkanen A (2020) The significance of spatial length scales and solute segregation in strengthening rapid solidification microstructures of 316l stainless steel. Acta Mater 184:1–16. https://doi.org/10.1016/j.actamat.2019.10.044
222. Wang Y, Shi J (2019) Engulfment and distribution of second-phase nanoparticle during dendrite solidification of an al-si binary alloy: a simulation study. Appl Phys A 125(6):1–12. https://doi.org/10.1007/s00339-019-2738-y
223. Chen C-H, Tabrizi AM, Geslin P-A, Karma A (2021) Dendritic needle network modeling of the columnar-to-equiaxed transition. part ii: three dimensional formulation, implementation and comparison with experiments. Acta Mater 202:463–477. https://doi.org/10.1016/j.actamat.2020.10.012
224. Chadwick AF, Voorhees PW (2022) Recursive grain remapping scheme for phase-field models of additive manufacturing. Int J Numer Methods Eng. https://doi.org/10.1002/nme.6966
225. Fan L, Werner W, Subotić S, Schneider D, Hinterstein M, Nestler B (2022) Multigrain phase-field simulation in ferroelectrics with phase coexistences: an improved phase-field model. Comput Mater Sci 203:111056. https://doi.org/10.1016/j.commatsci.2021.111056
226. Cissé C, Zaeem MA (2020) An asymmetric elasto-plastic phase-field model for shape memory effect, pseudoelasticity and thermomechanical training in polycrystalline shape memory alloys. Acta Mater 201:580–595. https://doi.org/10.1016/j.actamat.2020.10.034
227. Bhattacharya A, Mondal K, Upadhyay C, Sangal S (2020) A phase-field investigation of the effect of grain-boundary diffusion on austenite to ferrite transformation. Comput Mater Sci 173:109428. https://doi.org/10.1016/j.commatsci.2019.109428
228. Tzini MI, Aristeidakis JS, Christodoulou PI, Kermanidis AT, Haidemenopoulos GN, Krizan D (2022) Multi-phase field modeling in TRIP steels: distributed vs. average stability and strain-induced transformation of retained austenite. Mater Sci Eng: A 833:142341
229. Zhang X, Shen G, Li C, Gu J (2020) Phase-field simulation of austenite reversion in a fe-9.6 ni-7.1 mn (at.%) martensitic steel governed by a coupled diffusional/displacive mechanism. Mater Des 188:108426. https://doi.org/10.1016/j.matdes.2019.108426
230. Babaei H, Levitas VI (2020) Finite-strain scale-free phase-field approach to multivariant martensitic phase transformations with stress-dependent effective thresholds. J Mech Phys Solids 144:104114. https://doi.org/10.1016/j.jmps.2020.104114
231. Wang F, Altschuh P, Matz AM, Heimann J, Matz BS, Nestler B, Jost N (2019) Phase-field study on the growth of magnesium silicide occasioned by reactive diffusion on the surface of si-foams. Acta Mater 170:138–154. https://doi.org/10.1016/j.actamat.2019.03.008
232. Murgas B, Flipon B, Bozzolo N, Bernacki M (2022) Level-set modeling of grain growth in 316l stainless steel under different assumptions regarding grain boundary properties. Materials 15(7):2434. https://doi.org/10.3390/ma15072434
233. Chandrappa N, Bernacki M (2023) A level-set formulation to simulate diffusive solid/solid phase transformation in polycrystalline metallic materials-application to austenite decomposition in steels. Comput Mater Sci 216:111840. https://doi.org/10.1016/j.commatsci.2022.111840
234. Bernacki M, Logé RE, Coupez T (2011) Level set framework for the finite-element modelling of recrystallization and grain growth in polycrystalline materials. Scr Mater 64(6):525–528. https://doi.org/10.1016/j.scriptamat.2010.11.032
235. Scholtes B, Boulais-Sinou R, Settefrati A, Muñoz DP, Poitrault I, Montouchet A, Bozzolo N, Bernacki M (2016) 3d level set modeling of static recrystallization considering stored energy fields. Comput Mater Sci 122:57–71. https://doi.org/10.1016/j.commatsci.2016.04.045
236. Elsey M, Esedoglu S, Smereka P (2011) Large-scale simulation of normal grain growth via diffusion-generated motion. Proc R Soc A Math Phys Eng Sci 467(2126):381–401. https://doi.org/10.1098/rspa.2010.0194
237. Elsey M, Esedog S, Smereka P et al (2009) Diffusion generated motion for grain growth in two and three dimensions. J Comput Phys 228(21):8015–8033. https://doi.org/10.1016/j.jcp.2009.07.020
238. Florez S, Shakoor M, Toulorge T, Bernacki M (2020) A new finite element strategy to simulate microstructural evolutions. Comput Mater Sci 172:109335. https://doi.org/10.1016/j.commatsci.2019.109335
239. Florez S, Alvarado K, Muñoz DP, Bernacki M (2020) A novel highly efficient lagrangian model for massively multidomain simulation applied to microstructural evolutions. Comput Methods Appl Mech Eng 367:113107. https://doi.org/10.1016/j.cma.2020.113107
240. Ghoneim A (2016) A new technique for numerical simulation of dendritic solidification using a meshfree interface finite element method. Int J Numer Methods Eng 107(10):813–852. https://doi.org/10.1002/nme.5185
241. Pei R, Korte-Kerzel S, Al-Samman T (2020) Normal and abnormal grain growth in magnesium: experimental observations and simulations. J Mater Sci Technol 50:257–270. https://doi.org/10.1016/j.jmst.2020.01.014
242. Grand V, Flipon B, Gaillac A, Bernacki M (2022) Simulation of continuous dynamic recrystallization using a level-set method. Materials 15(23):8547. https://doi.org/10.3390/ma15238547
243. Furstoss J, Petit C, Ganino C, Bernacki M, Pino-Muñoz D (2021) A new finite element approach to model microscale strain localization within olivine aggregates. Solid Earth 12(10):2369–2385. https://doi.org/10.5194/se-12-2369-2021
244. Moghadam M, Voorhees PW (2018) Level-set simulation of anisotropic phase transformations via faceted growth. Comput Mater Sci 143:454–461. https://doi.org/10.1016/j.commatsci.2017.10.055
245. Chen F, Zhu H, Zhang H, Cui Z (2020) Mesoscale modeling of dynamic recrystallization: multilevel cellular automaton simulation framework. Metall Mater Trans A 51(3):1286–1303. https://doi.org/10.1007/s11661-019-05620-3
246. Sarrazola DR, Muñoz DP, Bernacki M (2020) A new numerical framework for the full field modeling of dynamic recrystallization

in a cpfem context. Comput Mater Sci 179:109645. https://doi.org/10.1016/j.commatsci.2020.109645
247. Beaudoin A, Dawson P, Mathur K, Kocks U (1995) A hybrid finite element formulation for polycrystal plasticity with consideration of macrostructural and microstructural linking. Int J Plast 11(5):501–521. https://doi.org/10.1016/S0749-6419(99)80003-5
248. Mika D, Dawson P (1999) Polycrystal plasticity modeling of intracrystalline boundary textures. Acta Mater 47(4):1355–1369. https://doi.org/10.1016/S1359-6454(98)00386-3
249. Jivkov A, Stevens N, Marrow T (2006) A three-dimensional computational model for intergranular cracking. Comput Mater Sci 38(2):442–453. https://doi.org/10.1016/j.commatsci.2006.03.012
250. Gilbert E (1962) Random subdivisions of space into crystals. Ann Mathl Stat 33(3):958–72
251. Saylor DM, Fridy J, El-Dasher BS, Jung K-Y, Rollett AD (2004) Statistically representative three-dimensional microstructures based on orthogonal observation sections. Metall Mater Trans A 35(7):1969–1979. https://doi.org/10.1007/s11661-004-0146-0
252. Van Houtte P, Delannay L, Kalidindi S (2002) Comparison of two grain interaction models for polycrystal plasticity and deformation texture prediction. Int J Plast 18(3):359–377. https://doi.org/10.1016/S0749-6419(00)00102-9
253. Bate P, Fonseca JQ (2004) Texture development in the cold rolling of if steel. Mater Sci Eng A 380(1–2):365–377. https://doi.org/10.1016/j.msea.2004.04.007
254. Ritz H, Dawson P (2008) Sensitivity to grain discretization of the simulated crystal stress distributions in fcc polycrystals. Model Simul Mat Sci Eng 17(1):015001. https://doi.org/10.1088/0965-0393/17/1/015001
255. Kalidindi SR, Bronkhorst CA, Anand L (1992) Crystallographic texture evolution in bulk deformation processing of fcc metals. J Mech Phys Solids 40(3):537–569. https://doi.org/10.1016/0022-5096(92)80003-9
256. Johnson WA (1939) Reaction kinetics in processes of nucleation and growth. Am Inst Min Metal Petro Eng 135:416–458
257. Ragnemalm I (1992) Fast erosion and dilation by contour processing and thresholding of distance maps. Pattern Recognit Lett 13(3):161–166. https://doi.org/10.1016/0167-8655(92)90055-5
258. Meyer F, Beucher S (1990) Morphological segmentation. J Vis Commun Image Represent 1(1):21–46. https://doi.org/10.1016/1047-3203(90)90014-M
259. Jeulin D (1989) Morphological modeling of images by sequential random functions. Signal Process 16(4):403–431. https://doi.org/10.1016/0165-1684(89)90033-9
260. Diard O, Leclercq S, Rousselier G, Cailletaud G (2005) Evaluation of finite element based analysis of 3d multicrystalline aggregates plasticity: Application to crystal plasticity model identification and the study of stress and strain fields near grain boundaries. Int J Plast 21(4):691–722. https://doi.org/10.1016/j.ijplas.2004.05.017
261. Zeghadi A, N'guyen F, Forest S, Gourgues AF, Bouaziz O (2007) Ensemble averaging stress–strain fields in polycrystalline aggregates with a constrained surface microstructure–part 1: anisotropic elastic behaviour. Philos Mag 87:1401–1424. https://doi.org/10.1080/14786430601009509
262. Fritzen F, Böhlke T, Schnack E (2009) Periodic three-dimensional mesh generation for crystalline aggregates based on voronoi tessellations. Comput Mech 43(5):701–713. https://doi.org/10.1007/s00466-008-0339-2
263. Quey R, Dawson P, Barbe F (2011) Large-scale 3d random polycrystals for the finite element method: Generation, meshing and remeshing. Comput Methods Appl Mech Eng 200(17–20):1729–1745. https://doi.org/10.1016/j.cma.2011.01.002
264. Zhang P, Karimpour M, Balint D, Lin J (2012) Three-dimensional virtual grain structure generation with grain size control. Mech Mater 55:89–101. https://doi.org/10.1016/j.mechmat.2012.08.005
265. Nouri N, Ziaei-Rad V, Ziaei-Rad S (2013) An approach for simulating microstructures of polycrystalline materials. Comput Mech 52(1):181–192. https://doi.org/10.1007/s00466-012-0805-8
266. Suzudo T, Kaburaki H (2009) An evolutional approach to the numerical construction of polycrystalline structures using the voronoi tessellation. Phys Lett A 373(48):4484–4488. https://doi.org/10.1016/j.physleta.2009.09.072
267. Ganesan S, Javaheri I, Sundararaghavan V (2021) Constrained voronoi models for interpreting surface microstructural measurements. Mech Mater 159:103892. https://doi.org/10.1016/j.mechmat.2021.103892
268. Quey R, Renversade L (2018) Optimal polyhedral description of 3d polycrystals: Method and application to statistical and synchrotron x-ray diffraction data. Comput Methods Appl Mech Eng 330:308–333. https://doi.org/10.1016/j.cma.2017.10.029
269. Rycroft C (2009) Voro++: A three-dimensional voronoi cell library in c++. Technical report, Lawrence Berkeley National Lab.(LBNL), Berkeley, CA (United States). https://doi.org/10.1063/1.3215722
270. Barber CB, Dobkin DP, Huhdanpaa H (1996) The quickhull algorithm for convex hulls. ACM Trans Math Softw 22(4):469–483. https://doi.org/10.1145/235815.235821
271. Hart KA, Rimoli JJ (2020) Microstructpy: a statistical microstructure mesh generator in python. SoftwareX 12:100595. https://doi.org/10.1016/j.softx.2020.100595
272. Pratt WK (2007) Digital Image Processing: PIKS Scientific Inside, vol 4, 4th edn. Wiley Online Library, Hoboken, pp 631–648. https://doi.org/10.1002/0471221325.ch18
273. Miodownik M, Godfrey A, Holm E, Hughes D (1999) On boundary misorientation distribution functions and how to incorporate them into three-dimensional models of microstructural evolution. Acta Mater 47(9):2661–2668. https://doi.org/10.1016/S1359-6454(99)00137-8
274. Press WH, Teukolsky SA, Vetterling WT, Flannery BP (2002) Numerical recipes in c++: The art of scientific computing, pp. 444–455. Cambridge university press, Cambridge. https://www.cec.uchile.cl/cinetica/pcordero/MC_libros/NumericalRecipesinC.pdf
275. Raabe D, Roters F, Barlat F, Chen L-Q (2004) Continuum Scale Simulation of Engineering Materials: Fundamentals-microstructures-process Applications, pp. 77–114. John Wiley & Sons, Hoboken. https://doi.org/10.1002/3527603786
276. Brahme A, Alvi M, Saylor D, Fridy J, Rollett A (2006) 3d reconstruction of microstructure in a commercial purity aluminum. Scr Mater 55(1):75–80. https://doi.org/10.1016/j.scriptamat.2006.02.017
277. St-Pierre L, Héripré E, Dexet M, Crépin J, Bertolino G, Bilger N (2008) 3d simulations of microstructure and comparison with experimental microstructure coming from oim analysis. Int J Plast 24(9):1516–1532. https://doi.org/10.1016/j.ijplas.2007.10.004
278. Groeber M, Ghosh S, Uchic MD, Dimiduk DM (2008) A framework for automated analysis and simulation of 3d polycrystalline microstructures. part 2: Synthetic structure generation. Acta Mater 56(6):1274–12872. https://doi.org/10.1016/j.actamat.2007.11.040
279. Teferra K, Graham-Brady L (2015) Tessellation growth models for polycrystalline microstructures. Comput Mater Sci 102:57–67. https://doi.org/10.1016/j.commatsci.2015.02.006
280. Ilin DN, Bernacki M (2016) Advancing layer algorithm of dense ellipse packing for generating statistically equivalent polygonal

structures. Granul Matter 18(3):43. https://doi.org/10.1007/s10035-016-0646-9
281. Henrich M, Pütz F, Münstermann S (2020) A novel approach to discrete representative volume element automation and generation-dragen. Mater 13(8):1887. https://doi.org/10.3390/ma13081887
282. Chen P, Ghassemi-Armaki H, Kumar S, Bower A, Bhat S, Sadagopan S (2014) Microscale-calibrated modeling of the deformation response of dual-phase steels. Acta Mater 65:133–149. https://doi.org/10.1016/j.actamat.2013.11.036
283. Chen S, Kirubanandham A, Chawla N, Jiao Y (2016) Stochastic multi-scale reconstruction of 3d microstructure consisting of polycrystalline grains and second-phase particles from 2d micrographs. Metall Mater Trans A 47(3):1440–1450. https://doi.org/10.1007/s11661-015-3283-8
284. Ozturk T, Rollett AD (2018) Effect of microstructure on the elasto-viscoplastic deformation of dual phase titanium structures. Comput Mech 61(1):55–70. https://doi.org/10.1007/s00466-017-1467-3
285. Mandal S, Lao J, Donegan S, Rollett AD (2018) Generation of statistically representative synthetic three-dimensional microstructures. Scr Mater 146:128–132. https://doi.org/10.1016/j.scriptamat.2017.11.034
286. Tucker JC, Chan LH, Rohrer GS, Groeber MA, Rollett AD (2012) Tail departure of log-normal grain size distributions in synthetic three-dimensional microstructures. Metall Mater Trans A 43(8):2810–2822. https://doi.org/10.1007/s11661-011-0851-4
287. Bagri A, Weber G, Stinville J-C, Lenthe W, Pollock T, Woodward C, Ghosh S (2018) Microstructure and property-based statistically equivalent representative volume elements for polycrystalline ni-based superalloys containing annealing twins. Metall Mater Trans A 49(11):5727–5744. https://doi.org/10.1007/s11661-018-4858-y
288. Pinz M, Weber G, Ghosh S (2019) Generating 3d virtual microstructures and statistically equivalent rves for subgranular gamma-gamma'microstructures of nickel-based superalloys. Comput Mater Sci 167:198–214. https://doi.org/10.1016/j.commatsci.2019.05.043
289. Tu X, Shahba A, Shen J, Ghosh S (2019) Microstructure and property based statistically equivalent rves for polycrystalline-polyphase aluminum alloys. Int J Plast 115:268–292. https://doi.org/10.1016/j.ijplas.2018.12.002
290. Tang Y, Xiong Y, Park S-I, Rosen DW (2020) Universal material template for heterogeneous objects with applications to additive manufacturing. Comput Aided Des 129:102929. https://doi.org/10.1016/j.cad.2020.102929
291. Foster RC, Vander Wiel S, Anghel V, Bronkhorst C (2021) Towards random generation of microstructures of spatially varying materials from orthogonal sections. Comput Mater Sci 192:110313. https://doi.org/10.1016/j.commatsci.2021.110313
292. Kotha S, Ozturk D, Smarslok B, Ghosh S (2020) Uncertainty quantified parametrically homogenized constitutive models for microstructure-integrated structural simulations. Integr Mater Manuf Innov 9(4):322–338. https://doi.org/10.1007/s40192-020-00187-z
293. Miyazawa Y, Briffod F, Shiraiwa T, Enoki M (2019) Prediction of cyclic stress-strain property of steels by crystal plasticity simulations and machine learning. Materials 12(22):3668. https://doi.org/10.3390/ma12223668
294. Yaghoobi M, Stopka KS, Lakshmanan A, Sundararaghavan V, Allison JE, McDowell DL (2021) Prisms-fatigue computational framework for fatigue analysis in polycrystalline metals and alloys. Npj Comput Mater 7(1):1–12. https://doi.org/10.1038/s41524-021-00506-8
295. Tran A, Wildey T (2021) Solving stochastic inverse problems for property-structure linkages using data-consistent inversion and machine learning. JOM 73(1):72–89. https://doi.org/10.1007/s11837-020-04432-w
296. Pokharel R, Pandey A, Scheinker A (2021) Physics-informed data-driven surrogate modeling for full-field 3d microstructure and micromechanical field evolution of polycrystalline materials. JOM 73(11):3371–3382. https://doi.org/10.1007/s11837-021-04889-3
297. Dai M, Demirel MF, Liang Y, Hu J-M (2021) Graph neural networks for an accurate and interpretable prediction of the properties of polycrystalline materials. Npj Comput Mater 7(1):1–9. https://doi.org/10.1038/s41524-021-00574-w
298. Pandey A, Pokharel R (2021) Machine learning based surrogate modeling approach for mapping crystal deformation in three dimensions. Scr Mater 193:1–5. https://doi.org/10.1016/j.scriptamat.2020.10.028
299. Efros AA, Freeman WT (2001) Image quilting for texture synthesis and transfer. In: Proceedings of the 28th Annual Conference on Computer Graphics and Interactive Techniques, pp. 341–346. https://doi.org/10.1145/383259.383296
300. Javaheri I, Andani MT, Sundararaghavan V (2022) Large-scale synthesis of metal additively-manufactured microstructures using markov random fields. Comput Mater Sci 206:111228. https://doi.org/10.1016/j.commatsci.2022.111228
301. Javaheri I, Sundararaghavan V (2020) Polycrystalline microstructure reconstruction using markov random fields and histogram matching. Comput Aided Des 120:102806. https://doi.org/10.1016/j.cad.2019.102806
302. Acar P, Sundararaghavan V (2016) A markov random field approach for modeling spatio-temporal evolution of microstructures. Model Simul Mat Sci Eng 24(7):075005. https://doi.org/10.1088/0965-0393/24/7/075005
303. Wei L-Y, Levoy M (2000) Fast texture synthesis using tree-structured vector quantization. In: Proceedings of the 27th Annual Conference on Computer Graphics and Interactive Techniques, pp. 479–488. https://doi.org/10.1145/344779.345009
304. Bertolino G, Bilger N, Crepin J (2007) Modeling microstructures and microstructural effects on macroscopic and intragranular mechanical behavior. Comput Mater Sci 40(3):408–416. https://doi.org/10.1016/j.commatsci.2007.01.009
305. Kumar A, Nguyen L, DeGraef M, Sundararaghavan V (2016) A markov random field approach for microstructure synthesis. Model Simul Mat Sci Eng 24(3):035015. https://doi.org/10.1088/0965-0393/24/3/035015
306. Sundararaghavan V, Zabaras N (2004) A dynamic material library for the representation of single-phase polyhedral microstructures. Acta Mater 52(14):4111–4119. https://doi.org/10.1016/j.actamat.2004.05.024
307. Li Z, Wen B, Zabaras N (2010) Computing mechanical response variability of polycrystalline microstructures through dimensionality reduction techniques. Comput Mater Sci 49(3):568–581. https://doi.org/10.1016/j.commatsci.2010.05.051
308. Bostanabad R (2020) Reconstruction of 3d microstructures from 2d images via transfer learning. Comput Aided Des 128:102906. https://doi.org/10.1016/j.cad.2020.102906
309. Sundararaghavan V, Zabaras N (2005) Classification and reconstruction of three-dimensional microstructures using support vector machines. Comput Mater Sci 32(2):223–239. https://doi.org/10.1016/j.commatsci.2004.07.004
310. Wen B, Zabaras N (2012) A multiscale approach for model reduction of random microstructures. Comput Mater Sci 63:269–285. https://doi.org/10.1016/j.commatsci.2012.06.021
311. Cang R, Xu Y, Chen S, Liu Y, Jiao Y, Yi Ren M (2017) Microstructure representation and reconstruction of heterogeneous

materials via deep belief network for computational material design. J Mech Design 139(7):071404. https://doi.org/10.48550/arXiv.1612.07401
312. Cang R, Li H, Yao H, Jiao Y, Ren Y (2018) Improving direct physical properties prediction of heterogeneous materials from imaging data via convolutional neural network and a morphology-aware generative model. Comput Mater Sci 150:212–221. https://doi.org/10.1016/j.commatsci.2018.03.074
313. Patala S, Mason JK, Schuh CA (2012) Improved representations of misorientation information for grain boundary science and engineering. Prog Mater Sci 57(8):1383–1425. https://doi.org/10.1016/j.pmatsci.2012.04.002
314. Nolze G, Hielscher R (2016) Orientations-perfectly colored. J Appl Crystallogr 49(5):1786–1802. https://doi.org/10.1107/s1600576716012942
315. Tran A, Mitchell JA, Swiler LP, Wildey T (2020) An active learning high-throughput microstructure calibration framework for solving inverse structure-process problems in materials informatics. Acta Mater 194:80–92. https://doi.org/10.1016/j.actamat.2020.04.054
316. Acar P (2021) Recent progress of uncertainty quantification in small-scale materials science. Prog Mater Sci 117:100723. https://doi.org/10.1016/j.pmatsci.2020.100723